CONTENTS

Image Anal Stereol 2013;32:127-133 doi:10.5566/ias.v32.p127-133
Review Article

25 YEARS OF THE POLISH SOCIETY FOR STEREOLOGY

LESZEK WOJNAR
Institute of Applied Informatics, Faculty of Mechanical Engineering, Cracow University of Technology, Al. Jana Pawla II 37, 31-864 Cracow, Poland
e-mail: leszek.wojnar@gmail.com
(Received November 12, 2013; accepted November 13, 2013)

ABSTRACT

25 years history of the Polish Society for Stereology is summarized by a person playing active role in the Society from the very beginning till now. Formation and growth of the society is described with emphasize to some milestones in the Society history. This paper is the first attempt to summarize the activity of this scientific organization.

Keywords: history, Polish Society for Stereology, stereology.

INTRODUCTION

25 years is a significant period in professional career of a man as it lasts usually about 40 years. It is also a significant period for a scientific organization, especially in the era of unprecedented changes in science and technology we currently observe. Taking into account the above mentioned remarks I have tried to describe some items from the history of the Polish Society for Stereology. This is a highly emotional story as I have been involved in building this Society from scratch. I have written its Statute, next I have been a member of all the executive boards and in the years 1997-2001 I served to the Society as its president. It is my intention not to bother the readers with small problems that we faced during these 25 years. I want just to show some universal values and achievements that gives our Society the right to feel as a partner to the international scientific community.

BACKGROUND AND FIRST STEPS

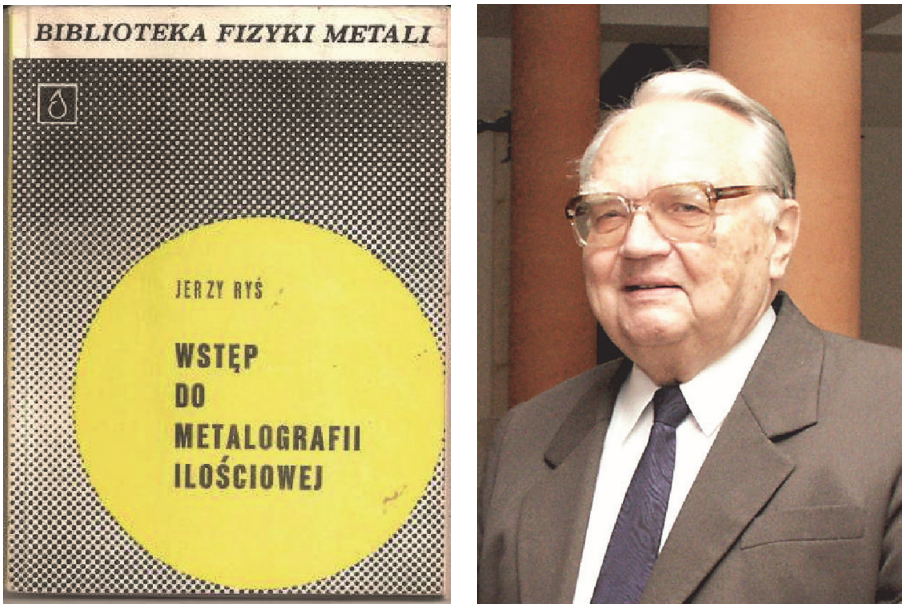

Fig. 1. *Cover page of the fundamental work of Jerzy Ryś "Introduction to quantitative metallography", 1970 (left) and prof. Jerzy Ryś at the meeting in Zakopane in 2002 (right).*

Stereological tools have been present in Poland since many years. Some achievements were published even before the Second World War (Bodziony and Hübner, 1987). In 1970 Jerzy Ryś published his "Introduction to quantitative metallography" (Fig. 1). Please, note that in the same year Ervin E. Underwood issued his famous "Quantitative stereology". First attempts to develop a formal organization of Polish stereologists were undertaken in 1981 at the Strata Mechanics Research Institute of the Polish Academy of Sciences. A reference list of Polish publications on stereology or its applications covered 95 papers (Bodziony, 1990). In 1983 the first conference on Stereology in Materials Science took place in Wisła (more on conferences you can find later in this paper) and prof. Jerzy Ryś form the Academy of Mining and Metallurgy established the Group for Stereology at the Committee for Materials Science of the Polish Academy of Sciences. Already in 1978 the Polish Society of Pathologists formed the Section of Mathematical Pathology. Prof. Edward Waniewski initiated in 1984 a series of interdisciplinary conferences on "Morphometric Methods in Biology and Medicine"

In spite of these various activities the political climate in Poland was against formation of any new organization. Finally, after breaking some bureaucratic barriers, the Polish Society for Stereology was founded in 1988 with the aim to facilitate exchange of scientific information among Polish stereologists and their foreign colleagues associated in the International Society for Stereology (Bodziony, 1990). At the first General Assembly of the Society, held in Cracow, Poland on November 28, 1988 Jakub Bodziony was elected as the first President in history of the Polish Society for Stereology.

INTERNATIONAL CONTACTS

One of the goals of the Polish Society for Stereology in the first period of its activity was development of wider contacts with the International Society for Stereology. These relations begun even before organization of the Society. Prof. Jakub Bodziony was in contact with prof. Miro Kališnik since the congress in Vienna and a wider representation of Polish Scientists participated in the European Congress in Goteborg (Sweden, 1985) and International Congress in Caen (France, 1987). At that time a very important person for our Society was Jean-Louis Chermant who helped many of our colleagues to join the congresses in Caen and next in Freiburg (Germany, 1989) and Irvine (USA, 1991).

Thanks to the existence of the Polish Society for Stereology it was much easier to invite foreign scientists to Poland. The conferences in 1990 and 1994 proved that the scientific contacts were necessary and fruitful. More about the conferences is written in the next chapter.

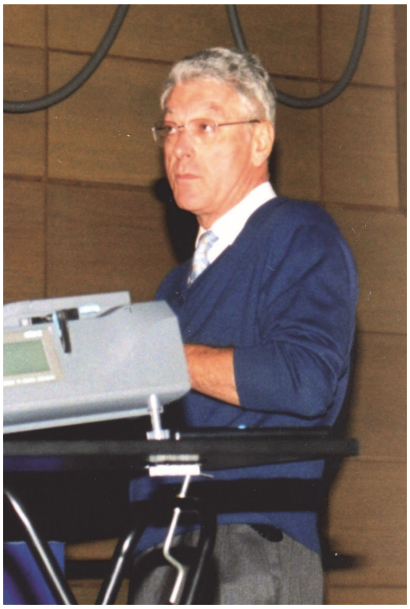

Fig. 2. *Jean-Louis Chermant during the STERMAT conference held in Cracow in 2000.*

Fig. 3. *Vaclav Horalek (Czech Republic), Rodney Coleman (United Kingdom) and Ervin E. Underwood (USA) during the STERMAT'90 conference (1990).*

The subtle networks of contacts and often friendship are very important till nowadays when we can easily communicate using the Internet, call phones or international travels without visas. Hopefully, these contacts are still vivid but we should increase them, especially for the younger generation of stereologists.

ACTIVITIES

The flagship activity of the Polish Society for Stereology is a series of STERMAT (STEreology in MATerials science) conferences. These conferences started before the Society, in 1983. The third STERMAT conference was held in 1990 and organized already under the auspices of the Polish Society for Stereology and International Society for Stereology. It was, simultaneously, the first STERMAT conference with English as an official conference language.

Fig. 4. *Most of the STERMAT conferences were held in the Polish mountains.*

The name of the conference slightly changed over the years and up to now the following nine conferences have been organized (official names are preserved):

I Konferencja
Stereologia w badaniach materiałoznawczych
Kraków-Wisła, maj 1983

II Konferencja
Stereologia w badaniach materiałoznawczych
Kraków-Rudy Raciborskie, czerwiec 1986

The Third Conference on
Stereology in Materials Science STERMAT'90
Kraków-Katowice (Szczyrk), October 1990

IV Intenational Conference on
Stereology and Image Analysis in Materials Science
STERMAT'94
Beskidy Mountains (Wisła), October 3–6, 1994

International Conference on
the Quantitative Description of Materials
Microstructure Q-MAT'97
Warsaw, April 16–19, 1997

Sixth International Conference on
Stereology and Image Analysis in Materials Science
Cracow, September 20–23, 2000

Seventh International Conference on
Stereology and Image Analysis in Materials Science
Zakopane, May 10–13, 2005
(conference jointly organized with 9th European Congress on Stereology and Image Analysis)

VIII International Conference on
Stereology and Image Analysis in Materials Science
STERMAT 2008
Zakopane, September 2–6, 2008

IX International Conference on
Stereology and Image Analysis in Materials Science
STERMAT 2012
Zakopane, September 3–6, 2012

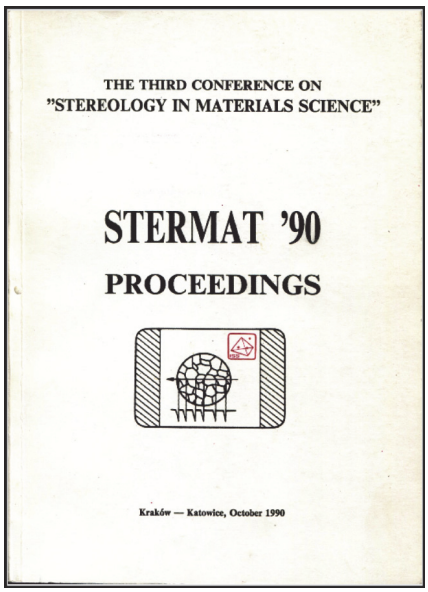

Fig. 5. *Proceeding of The third conference on Stereology in materials science STERMAT'90, the first international meeting organized by the Polish Society for Stereology.*

The organizing committees of consecutive STERMAT meetings have paid attention to keep the following properties that have been in our opinion essential for the final success:

- The conference venue should assure accommodation of all the participants and sessions in the same place – this makes easier any informal discussion,
- One should assure good food, as hungry man is an angry men and, last but not least,
- The conference proceedings should be available at the beginning of the conference, not a year after it.

Fig. 6. *There were always severe discussions about the role of posters in the conference.*

In the conferences from the STERMAT series took part numerous scientists very important for the international scientific family and International Society for Stereology. Among them were (in alphabetical order): David Aboav, Viktor Beneš, Jean-Marc Chaix, Jean-Louis Chermant, Rodney Coleman, Louis M. Cruz-Orive, Ida Eržen, Hans Jurgen Gundersen, Dominique Jeulin, Torsten Mattfeldt, Gerhard Ondraček, Brian Ralph, Ivan Saxl, Jean Serra, Jöelle Riss, Erwin E. Underwood, George VanderVoort and others, not listed here. It demonstrates the value and strength of this series of conferences.

In recent years changes in economic situation of the universities together with the growing value of virtual contacts and electronic publications make organization of conferences more and more difficult. Such a critical situation has been observed last year when the STERMAT conference has been initially waived but finally organized in autumn. We believe, however, that the quality and family-like atmosphere of our meetings will allow to gather a lot of people interested in scientific discussion in real world also during the coming meetings.

There are also other forms of activity of the Polish Society for Stereology. Among them the most valuable is a series of Schools on Image Analysis and Stereology, devoted to training in application of modern techniques in quantitative description of microstructures and organized usually in October. These schools have been also coupled with seminars for young stereologists – they can present their works and get opinions from the leading experts in the field. Schools have been also attended by guests from other countries, like, for example Hynek Lauschmann or Bruno Lay who demonstrated the newest software for image analysis. Independently, Dorota Cebula-Kozłowska has organized under the auspices of the Polish Society for Stereology a series of courses devoted to various aspects of structure-properties relationships. One of the leading lecturers during these courses has been George Vander Voort.

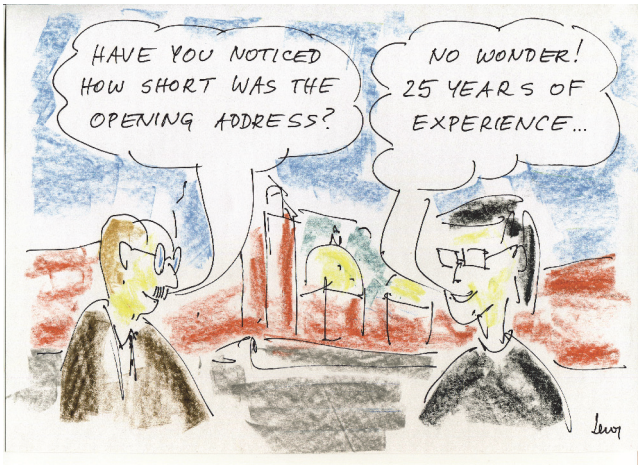

Fig. 7. *Everything that happened during the conference could be satirically commented during the closing session.*

GOVERING THE SOCIETY

Since its formation in 1988 the Polish society for Stereology has had 7 Presidents. In general, they keep their position for 4 years. The unofficial rule is that everybody is a president only once – such a rule prevents from many personal conflicts. The following people were in power in the history of the Society:

1988–1992 - Jakub Bodziony, Strata Mechanics Research Institute of the Polish Academy of Sciences,

1992–1996 - Jan Cwajna, Chair of Materials Engineering, Silesian University of Technology,

1996–1999 - Krzysztof J. Kurzydłowski, Institute of Materials Engineering, Warsaw University of Technology,

1999–2003 - Leszek Wojnar, Institute of Materials Science and Technology of Metals, Cracow University of Technology,

2003–2007 - Jacek Chrapoński, Chair of Materials Engineering, Silesian University of Technology,

2007–2012 - Janusz Szala, Chair of Materials Engineering, Silesian University of Technology,

and since 2012 - Aneta Gądek-Moszczak, Institute of Applied Informatics, Cracow University of Technology.

The Society is multidisciplinary and opened for all the disciplines. However, it is clearly visible that the Presidents of the Society have been associated with scientific institutions oriented towards materials science. This reflects the fact that in Poland stereological methods have been developed mainly in materials science. Biologists or specialists in medicine are active rather in other societies. Obviously, there exists cooperation between specialists in various disciplines, so this is a challenge for the Board of the Society to widen representation of natural sciences in the Society.

It is clear for anybody involved in any activity of larger scale that finances constitute a basis for different projects. Thus, it is essential to have a proper treasurer. This position is kept from the very beginning by the same person – Kazimierz Satora.

Fig. 8. *Presidents of the Polish Society for Stereology during a meeting on November 7, 2013. From left to right: Jakub Bodziony, Jan Cwajna, Leszek Wojnar, Jacek Chrapoński, Janusz Szala, Aneta Gądek-Moszczak. Only one of the past presidents, Krzysztof J. Kurzydłowski is missing.*

Fig. 9. *Krzysztof J. Kurzydłowski, President of the Polish Society for Stereology in the years 1994-1997.*

Fig. 10. *Kazimierz Satora, treasurer of the Polish Society for Stereology.*

PUBLICATIONS

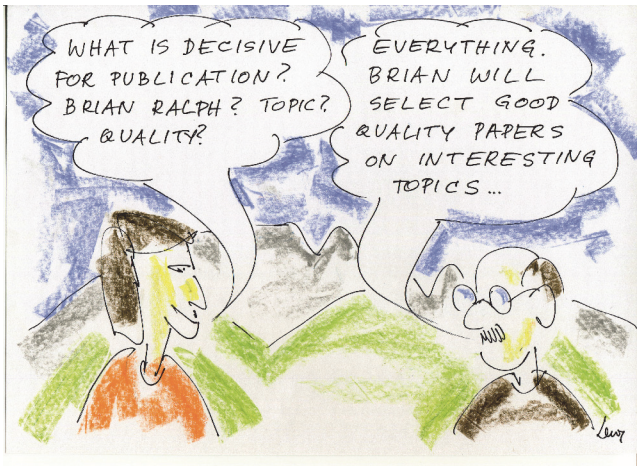

Fig. 11. *Selected papers were published after modification in Materials Characterization and Brian Ralph, being the Associate Editor, made final decision if the paper is suitable for publication.*

During these 25 years members of the Society have published numerous papers and books. Many of them have been published in Acta Stereologica and, after change of the name, in Image Analysis and Stereology. The most important for the international audience are probably some books or chapters in large monographs. Among such sources of information we can list books by Kurzydłowski and Ralph (1995) and Wojnar (1999) as well as contributions to larger projects (Wojnar and Kurzydłowski, 2000 or Wojnar *et al*., 2004). An important role has been played, especially in the early nineties, by the STERMAT conference proceedings. Due to good quality of these proceedings it was possible to send them to many libraries and obtain other valuable materials. The list of publications prepared by the members of the Polish Society for Stereology is obviously much longer, but publications in Polish are of less interest for international audience and the list of scientific papers in journals would be simply too long to publish here. There is, however, one book written in Polish that seems to be worth mentioning here. It was published in 2002 by Leszek Wojnar, Krzysztof J. Kurzydłowski and Janusz Szala. Its title is "Praktyka analizy obrazu" (Image analysis in practice). The book was printed in 1000 copies and, after distribution of them, is available since 2006 in electronic form at the digital library of the Cracow University of Technology. Up to date, more than 7000 downloads has been recorded (in addition to the book two files are available, so the book has been downloaded approx. 2500 times).

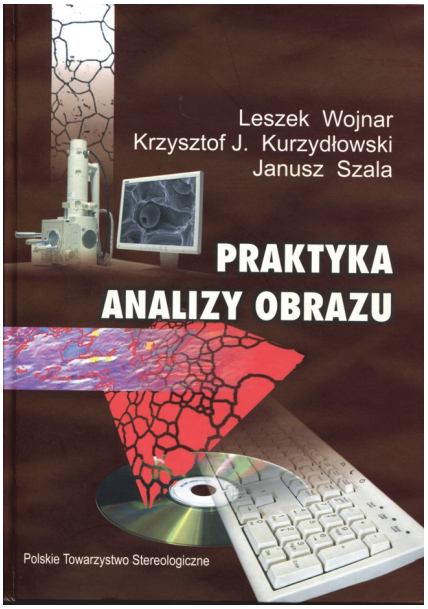

Fig. 12. *This book (Image analysis in practice) issued by the Polish Society for Stereology in 2002 and, in electronic form, in 2006 is still a leading textbook on image analysis in Poland.*

HUMOR

A good sense of humor helps to solve difficult problems. Sometimes this is the best, if not the only one, method to relax in situations full of stress. The second day of the STERMAT'90 conference was just a day of reunification of Germany. Some German colleagues at the conference wanted to serve a glass of wine on this occasion. The atmosphere became very heavy – the ghosts of Second World War were still present in the air… Fortunately, Jean-Louis Chermant found a humorous solution. He asked me to prepare quickly some images. I decided to illustrate the changes in Europe as simple morphological operations in the map of Europe. Massive migration from East Germany through Poland and Czech Republic to West Germany that we observed in 1989-1990 has been interpreted as simple geodesic path. Other changes were interpreted as segmentation, watershed detection or simple closing procedures (see Fig. 13). Jean-Louis Chermant presented it in very light, humorous version and concluded that everything would be O.K. if only we used proper structuring elements. The atmosphere on the conference was rescued.

The above described event was probably the most dramatic one in the history of our meetings. But tens of my humorous drawings accompanied almost all the conferences organized by the Polish Society for

Stereology. Some of the examples are put in this paper. I do hope that in spite of this activity I am recognized mainly as a scientist rather than an artist.

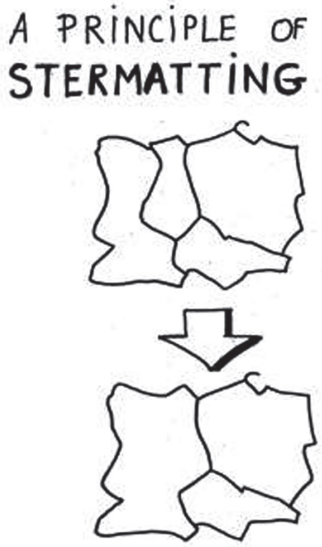

Fig. 13. *Reunification of Germany interpreted as morphological operation called "stermatting". The only problem, accordingly to Jean-Louis Chermant, was to use proper structuring element.*

PERSPECTIVES

This is clear that during the last 25 years we have observed dramatic changes in political, economic and technical environment. In 1988 we were still before the era of the Internet and websites and the iron curtain between the East and West in Europe seemed to be very strong. So, the conditions for running a scientific society are nowadays completely different. However, some words of Jakub Bodziony, prepared for STERMAT'90 seem to be still valid and important: "It is necessary to propagate among young people the problems of stereology and to help them in their scientific careers. I do not mean that we are doing nothing in this respect; what I mean is to consolidate our efforts" (Bodziony, 1990).

Before the next STERMAT conference that was held in 1994 Jean-Louis Chermant, who could not join the conference, sent me an opening address in which we could read (this material was not published yet): "And what about borders WITHIN Science? Let me only consider the main field of interest of members of our Society. Of course, Image Analysis, Mathematical Morphology, Stereology are fantastic tools. But perhaps some of you are of the opinion that one of these tools is far more fantastic than the others? If such is the case, I suggest that here again some borders should be abolished. So I am convinced that each of us has got something to teach, and something to learn from the others."

So, some problems have been recognized but remained unsolved since many years. This constitutes new challenges for scientific societies and, due to deep changes in our civilization, requires new solutions. Among these new solutions we can possibly find the need to redefine stereology.

REFERENCES

Bodziony J, Hübner K (1987). Hugo Steinhaus – an unknown stereologists? Acta Stereol 6(Suppl. II):69–78.

Bodziony J (1990). Polish Stereologists. In: Proceedings of the Third Conference on Stereology in Materials Science STERMAT'90, 1990 Oct 1-4; Kraków-Katowice, Poland, 292-304.

Kurzydlowski KJ, Ralph B (1995). The Quantitative Description of the Microstructure of Materials. Boca Raton: CRC Press.

Wojnar L (1999). Image analysis. Applications in materials engineering. Boca Raton: CRC Press.

Wojnar L, Kurzydłowski KJ (2000). Analysis and Interpretation. In: Practical Guide to Image Analysis. Materials Park, Ohio: ASM International, 145–202.

Wojnar L, Kurzydłowski KJ, Szala J (2004). Quantitative image analysis. In: ASM Handbook, Vol. 9. Metallography and Microstructures. Materials Park, Ohio: ASM International, 403–27.

Image Anal Stereol 2013;32:135-144 doi:10.5566/ias.v32.p135-144
Original Research Paper

THE CAPILLARY PATTERN IN HUMAN MASSETER MUSCLE DURING AGEING

ERIKA CVETKO[1], JIŘÍ JANÁČEK[2], LUCIE KUBÍNOVÁ[2] AND IDA ERŽEN✉,[1]

[1]Institute of Anatomy, Faculty of Medicine, University of Ljubljana, Ljubljana, Slovenia; [2]Department of Biomathematics, Institute of Physiology, Academy of Sciences of the Czech Republic
e-mails: erika.cvetko@mf-uni-lj.si; janacek@biomed.cas.cz; kubinova@biomed.cas.cz; ida.erzen@mf.uni-lj.si
(Received June 12, 2013; revised August 20, 2013; accepted October 8, 2013)

ABSTRACT

The effect of ageing on the capillary network in skeletal muscles has produced conflicting results in both, human and animals studies. Some of the inconsistencies are due to non-comparable and biased methods that were applied on thin transversal sections, especially in muscles with complicated morphological structures, such as in human masseter muscle. We present a new immunohistochemical method for staining capillaries and muscle fibres in 100 μm thick sections as well as novel approach to 3D visualization of capillaries and muscle fibres. Applying confocal microscopy and virtual 3D stereological grids, or tracing capillaries in virtual reality, length of capillaries within a muscle volume or length of capillaries adjacent to muscle fibre per fibre length, fibre surface or fibre volume were evaluated in masseter muscle of young and old subjects by an unbiased approach. Our findings show that anatomic capillarity is well maintained in masseter muscle in old subjects; however, vascular remodelling occurs with age, which could be a response to changed muscle function and age-related muscle fibre type transformations.

Keywords: 3D analysis, capillaries, confocal microscopy, human, masseter muscle.

INTRODUCTION

The effect of ageing on the capillary network in skeletal muscles has been studied in limb muscles predominantly. Both, human and animals studies have produced conflicting results. Some of the inconsistencies are due to noncomparable and biased methods that were applied on thin transversal sections, especially in muscles with complicated morphological structures, *e.g.* multipennate muscles composed of nonparallel muscle fibres of variable length. Such an anatomy suggests a complex ramification of the capillary network in 3D space which could not be satisfactorily assessed from 2D sections.

Most of the published studies on skeletal muscles counted capillary profiles and presented their results either as the number of capillary profiles per number of muscle fibre profiles (C/F), per muscle cross-sectional area (CD) or around a fibre profile (CAF), or the number of capillary contacts per fibre (CC) (Degens *et al.*, 1994; Hepple and Vogell, 2004; Croley *et al.*, 2005; Mathieu-Costello *et al.*, 2005; Ryan *et al.*, 2006; Čebašek *et al.*, 2010). Further, in human posterior crycoarythenoideus muscle (PCA) Lyon *et al.* (2007) estimated the length of capillaries per fibre and separately for each fibre type volume and surface area, using the orientator method. Methods based on Euler number (*cf.* Nyengaard, 1999; Knust *et al.*, 2009; Wulfson *et al.*, 2009) have successfully been applied in other research fields like lung, kidney etc., however they have not been introduced into the muscle research yet.

Research on animal muscles reported either maintained, unchanged capillary supply (Brown, 1987; Mitchell *et al.*, 1991; Hepple and Vogell, 2004; Mathieu-Costello *et al.*, 2005) or reduced capillary network (Degens *et al.*, 1994) with ageing. Similarly, in human muscles capillary supply has been reported to be either maintained (Denis *et al.*, 1986; Proctor *et al.*, 1995; Lyon *et al.*, 2007) or reduced (Coggan *et al.*, 1992; Frontera *et al.*, 2000; Croley *et al.*, 2005; Ryan *et al.*, 2006).

Compared to limb and trunk muscles masseter and PCA have special characteristics: masseter is active during the most part of the day to perform complex oral function such as mastication, speech, facial expression and postural control of mandible which are maintained with age. Similarly, the activity level was postulated to be the reason that there is a lack of age-related change in neuromuscular junction lengths or in the terminal axonal branching patterns at these junctions within the human PCA (Gambino *et al.*, 1990), which is active during inspiration, expiration and phonation.

Several studies proved also denser capillarization of type 1 than type 2 muscle fibres (oxidative and glycolytic fibres, respectively). Better capillary supply of type 1 than type 2 fibres was demonstrated in the triceps brachii, vastus lateralis and soleus muscles (Sjøgaard, 1982). Type 1 fibres in the triceps brachii muscle posses on average, 4.85 capillary profiles around each fibre, while in more oxidative soleus this number is 6.89; however, the difference should reflect varying oxidative capacity of the same muscle fibre type within various muscles.

Further, the ratio of capillary profiles to fibres was significantly larger in those muscles that exhibited a significantly larger proportion of oxidative fibre types (Cui *et al.*, 2008), while the number of capillary profiles per muscle cross-sectional area was larger in type 1 muscle fibres than in type 2 muscle fibres; *i.e.*, on average, in the oxidative muscle there are more capillary profiles per fibre compared to glycolytic muscle (Nelissen-Vrancken *et al.*, 1993). Long-term (4 weeks) ischemia increased significantly the capillary-to-fibre ratio in the soleus muscle, composed predominantly of type 1 fibres, whereas capillarity in the more glycolytic portion of the gastrocnemius muscle did not change.

Type 2 fibres of orofacial muscles display a relatively higher activity of oxidative enzymes than those of the limb muscles (Stål *et al.*, 1990), although it has been proved elsewhere that fibre size is decisive for the capillarity and the level of oxidative metabolism is just a secondary effect (Cotter *et al.*, 1973; Brown *et al.*, 1976; Škorjanc *et al.*, 1998; Egginton and Hudlická, 2000; Hepple and Vogel, 2004).

In limb muscles exercise training may prevent the age-related loss of muscle capillaries supplying type 1 fibres, while it is not efficient in maintaining capillary network to type 2a and 2b fibres. This suggests that ageing is accompanied by lower angiogenic potential of type 2 muscle fibres (Proctor *et al.*, 1995). Caution should be adopted when comparing the limb and jaw muscles because of intrinsic anatomic and behavioural differences in the masticatory apparatus and limb function. It could be speculated that postural function is predominant in limb muscle with ageing but not in jaw-closing muscles.

In our previous publication (Čebašek *et al.*, 2010) we proved that counting capillary profiles in 2D can underestimate capillary length by up to 75 percent in muscles with nonparallel muscle fibres and complicated anatomic composition. To avoid this estimation error we applied the method for estimating characteristics of the capillary network in 3D, introduced in our previous publications (Kubínová *et al.*, 2001; Eržen *et al.*, 2011; Janáček *et al.*, 2011). The method requires thick tissue sections from which a complete series of optical sections is captured by a confocal microscope. The capillary network is visualized in 3D and analysed within the whole sample volume. Although the method is more time consuming than the 2D method, muscle sample preparation requires a skilful technician and results need to be corrected for shrinkage in the z direction (Janáček *et al.*, 2012). This method provides a more complete information on the capillary anatomy in the studied muscles. Parameters that can be estimated within a unit of muscle tissue are the capillary length, number of capillary branchings, average capillary length and orientation of capillaries, *i.e.* the degree of anisotropy. Further, we measure the length of capillaries supplying muscle fibre type 1 and type 2 per muscle fibre length (Lcap/ Lfib), per muscle fibre surface area (Lcap/Sfib) and per muscle fibre volume (Lcap/Vfib).

The aim of the present study was to find out if in human masseter muscle vascular remodelling occurs with age, which could be a response to changed muscle function and age-related muscle fibre type transformations.

MATERIAL AND METHODS

Samples of masseter muscles were taken at autopsy from eight young subjects (average age 28.4 yrs, SEM = 2.7, range 19–39 yrs) and eight elderly subjects (average age 78.3 yrs, SEM = 1.5, range 70–84 yrs) who passed away either after brain stroke or in car accidents. Most autopsy samples of the super-ficial part of the muscle were excised up to 26 hrs post-mortem, one sample 48 hrs and we do not have precise information for one sample. The National Medical Ethics Committee of the Republic of Slovenia approved the research.

After excision muscle samples were immersed in liquid nitrogen and kept frozen in deep freezer at -70ºC. Transversal sections 100 µm thick were cut with the cryotome Cryo-Star HM 560 (Microm International GmbH, Waldorf, Germany) into cold phosphate buffered saline. They were immediately transferred into cold fixative for 48 hrs. Both solutions were kept at a constant temperature of +4ºC on a mixture of water and ice.

The fixative contained 10% formaldehyde and 0.1% glutaraldehyde in 5 mM Tris buffer with 0.5 mM EDTA and proteinase-K 0.2%. Throughout the fixation, rinsing and staining procedures sections were kept in small homemade baskets, which were gently transferred from one solution to the other. The penetration of all media and antibodies was enabled from all directions and at

the same time the sections were protected from mechanical injury.

IMMUNOHISTOCHEMISTRY

All antibodies were diluted in 2% bovine serum in phosphate buffered saline at pH 7.2 to 7.4. After thorough rinsing in phosphate buffered saline with Triton X-100 (PBST) 20 mM, sections were immersed in 20% normal goat serum for two hours followed by an overnight incubation in F8 (1:1000 to 1:2000) (Dako, Glostrup, Denmark), rinsing in PBST (1–2 hrs), incubation in anti mouse Alexa-Fluor 488 (1:500) (Invitrogen) for two hours, rinsing in PBST for 1–2 hrs, overnight incubation in monoclonal collagen (1:150) (Dako, Glostrup, Denmark), rinsing in PBST for 1–2 hrs, anti mouse Alexa-Fluor 546 1:500, rinsing in PBST (1–2 hours), overnight incubation in fluorescein conjugated Ulex europaeus agglutinin I (UEA) (Sigma Aldrich, St Louis, USA) 1:500 and final thorough rinsing in PBST for one hour.

Finally, sections were carefully transferred to the slides and embedded in Prolong ®Gold antifade (Invitrogen). To prevent tissue deformation the distance between the slide and the cover slip was maintained by two layers made by the ImgEdge pen (Dako, Glostrup, Denmark) (see Janáček *et al*., 2011).

CONFOCAL MICROSCOPY

Completely registered stacks of images of the whole thickness of specimen including its upper and lower neighbourhood were captured from thick sections by LSM 510 confocal microscope (Karl Zeiss, Jena, Germany) using a Plan Apochromat 20× (NA = 0.75) dry objective. Green and red fluorescence was excited with argon (488 nm) and He/Ne (543 nm) lasers, respectively. Emission signal was filtered using a narrow band (505–530 nm) and an LP 560-nm filter. Images (512×512 pixels) were captured at a pixel size from 0.62 to 1 μm with intervals 1μm in axial direction.

IMAGE PROCESSING

Correction of the tissue shrinkage

The apparent thickness of the confocal stack may be strongly influenced by physical deformation of the sample (Dorph-Petersen *et al.*, 2001) and optical phenomena (Hell *et al.*, 1993). The deformation occurs even in well fixed skeletal muscle samples; it is spatially homogeneous and can be corrected by adapting the intersection axial distance properly (Janáček *et al.*, 2012).

The apparent thickness of the transversal sections was estimated as the distance between optical sections where the average intensity at the section drops at half of the maximal value of section average intensity (the parameter is usually called FWHM - full width at half maximum).

The axial calibration of individual stacks was multiplied by a correction factor to match the apparent distance of the lower and upper surface of the thick section to the original thickness known from the microtome setting. The precision of the microtome calibration was carefully checked by authorized service.

The apparent thickness of the transversal sections was estimated as the distance between extreme optical sections where the average intensity at the section drops at half of the maximal value of section average intensity (the parameter is usually called FWHM - full width at half maximum).

Automatic detection of capillaries

The green channel of the 3D image coded by 256 levels of gray was pre-processed to enable automatic segmentation by thresholding. The image was smoothed by 3D Gaussian filter with parameter sigma set to 2 μm in order to decrease level of the noise. Then the slowly varying background due to nonspecific staining was removed by subtracting the lower Lipschitz envelope with slope 1 μm^{-1} (Štencel and Janáček, 2006). Binary image of capillaries obtained by thresholding was thinned by procedure called skeletonization using the 6-pass algorithm (Palágyi and Kuba, 1998) yielding line binary skeleton. The binary image then converted to spatial geometric graph of capillaries, composed of straight line segments (the graph edges) connected at endpoints (the graph vertices) by generating chains of line segments during automatic tracing of the thin lines in the binary image between the endpoints or branching points and connecting them to the centres of mass of remained thick parts. The graph was then resampled to obtain the uniform length of the line segments equal to 5 μm, because the chains obtained by tracing procedure composed of many short segments with irregular course do not represent well the smooth course of capillaries and would yield overestimates of length. The image processing and further measurements were accomplished by dedicated plug-ins of Ellipse programme (ViDiTo, Slovakia).

Manual tracing of capillaries

The graphs of capillaries were corrected manually using 3D editing program. We used a custom made programme with desktop virtual reality interface for PC with MS Windows (Microsoft, USA). The interface

consists of stereoscopic volume rendering of images with 3D cursor controlled by a haptic device (Sensable-Omni, SenseGraphics AB, Sweden) with force proportional to the gradient of the image intensity. The haptic feedback serves as a cue for depth perception and enables better placement of cursor in the capillaries. The stereoscopic rendering is accomplished either by a special graphic card with dedicated monitor and LCD shutter glasses or by anaglyph visualization with a common display and colour (RB) glasses. The program enables 3D drawing of capillaries as chains of line segments, moving individual points, connecting the chains together and deleting the vertices or chains. Eventually other 3D editor as Filament editor in Amira (VSG) or Tracer plug-in Ellipse may be used for editing.

Assigning capillaries to muscle fibres

Muscle fibre outlines were manually drawn at two to four levels within the stack from the topmost to the bottom image inside the sample. The outlines were used for muscle fibre diameter estimation and for assignment of the capillaries to individual fibres (see Janáček *et al.*, 2009). Fibre diameter was defined as the length of projection ('single' Feret's diameter) in the direction that is perpendicular to the direction of the maximal length of projection, implying that the diameter defined in this way is less influenced by the angle of cutting.

The neighbourhood of the fibre was represented by triangulated surface spanning contours obtained by dilation of contours of the fibre cross-section within the sample by 15 μm. The triangulated surface was selected by a dynamic programming algorithm from triangulated surfaces spanning the contours as the surface encompassing maximal volume. The total length of the capillaries around each individual muscle fibre was calculated by summing up the lengths of the line segments inside the fibre neighbourhood. Capillaries were assigned to a fibre when they were present within the 15-μm neighbourhood from the fibre. Several capillaries could be assigned to two or more fibres. The calculation was implemented in CapFibres plug-in of Ellipse program.

3D visualisation of capillaries and muscle fibres

The surfaces of muscle fibres were modelled by triangulated surfaces spanning the outlines of the fibres extremal cross-sections. The capillaries were modelled by chains of cylinders with constant diameter joined by spheres with the same diameter. The capillaries and fibre surfaces were rendered in Contours plug-in of program Ellipse using OpenGL graphic library (SGI, USA).

Parameters describing the capillary pattern in muscle samples

The length of capillaries is calculated by summing the line segments lengths. The course of capillaries and their distribution in regard to muscle fibre orientation were described by tortuosity, connectivity (*i.e.* number of branchings) and the degree of anisotropy (orientation).

We define *tortuosity* as average curvature – the sum of angles (in radians) between successive line segments divided by the total capillary length.

We estimated *connectivity* by the number of capillary branchings counted manually from 3D visualisation of capillaries. The number is equal to estimate of -2χ (χ is Euler-Poincaré characteristic – Gundersen *et al.*, 1993) for samples of capillary network, *i.e.* connected network without endpoints and with branching points where exactly three chains connect.

Orientation of capillaries was judged by the degree of anisotropy computed from eigenvalues of mean structural tensor in the following way: Each line segment of the traced capillaries $\langle a,b\rangle$ with end-points a and b of length L and direction $v = (b - a)/L$ yielded the matrix

$$U = \begin{pmatrix} v_1 \cdot v_1 & v_1 \cdot v_2 & v_1 \cdot v_3 \\ v_2 \cdot v_1 & v_2 \cdot v_2 & v_2 \cdot v_3 \\ v_3 \cdot v_1 & v_3 \cdot v_2 & v_3 \cdot v_3 \end{pmatrix}.$$

The average of all matrices (weighted by length) was calculated $T = \sum_i L_i U_i \Big/ \sum_i L_i$.

The anisotropy characteristics were calculated from the eigenvalues $\lambda_1 \geq \lambda_2 \geq \lambda_3 \geq 0$ of the matrix T

$$\frac{2\lambda_3}{\lambda_1 + \lambda_2}.$$

The obtained numbers can be in range from 1 (*i.e.* isotropy – capillaries express no preferential direction) to infinity (*i.e.* total anisotropy- all capillaries run in the same direction presumably parallel to the muscle fibre axes).

The mean capillary length was estimated as ⅔ of the total length divided by the number of branchings. The estimator is based on assumption that each capillary is connected to 2 other capillaries at each of both ends.

Parameters describing capillary supply of muscle fibre types

We estimated capillary characteristics: length of capillaries per muscle fibre length (Lcap/Lfib), per muscle fibre surface area (Lcap/Sfib) and per muscle fibre volume (Lcap/Vfib) of type 1 and type 2 muscle fibres separately. Muscle fibre types were selected by their diameter based on our previous research on masseter muscle (see Cvetko *et al.*, 2012). In most samples fibres smaller than 30 µm were classified as type 2 fibres and fibres larger than 40 µm as type 1 fibres. Since in three out of 16 samples muscle fibres were much smaller, those smaller than 20 µm were taken as type 2 fibres and those larger than 30 µm as type 1 fibres. All the remaining fibres were hybrid fibres (between type 1 and type 2 fibres) - they were excluded from the study.

STATISTICS

The statistical package Systat Version 5 was applied to calculate mean values and standard error of the mean (SEM) for the length of capillaries per muscle volume (Lcap/Vmuscle), Lcap/Lfib, Lcap/Sfib, Lcap/Vfib, tortuosity, anisotropy, Lbr, Nbr/Vmuscle and fibre diameter. Differences in mean values of the above parameters between masseter muscles of young and old subjects and between muscle fibres of type 1 and 2 were tested with independent samples test t. Differences among means were considered statistically significant, if $p < 0.05$.

RESULTS

The triple immunohistochemical staining detected capillaries in yellow - green and muscle fibres in red in most young and old subjects (Fig. 1). In several muscle samples, however, UEA lectin failed to detect capillaries. Those samples were excluded from the study.

Fig. 2 shows 3D rendering of capillaries and muscle fibres in masseter muscle of young and old subjects.

The characteristics of the capillary network were quite variable within every age group (Table 1). We could not detect any significant differences among both age groups; however, there was a trend toward reduction in curvature and branch density in the old group with a consequent elongation of the average capillary branch length. We need to point out that values for Lcap/Vmuscle and Nbr/Vmuscle could be biased as due to ethic reasons, we could not measure total volume of masseter muscles. The latter could therefore lead to a possible reference trap.

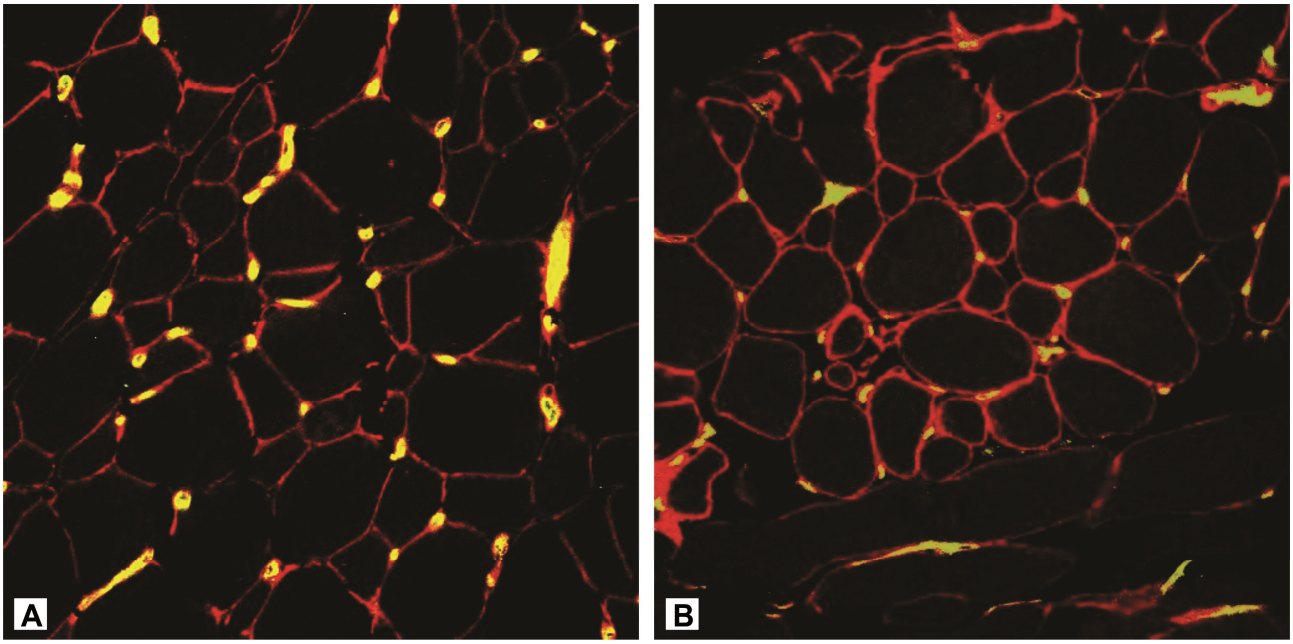

Fig. 1. *Capillaries and muscle fibres in human masseter muscle of young (a) and old (b) subject. Merged image of green and red channel. A triple immunofluorescence staining for capillaries (in yellow - green) and muscle fibre outlines (in red). Scale=100 µm.*

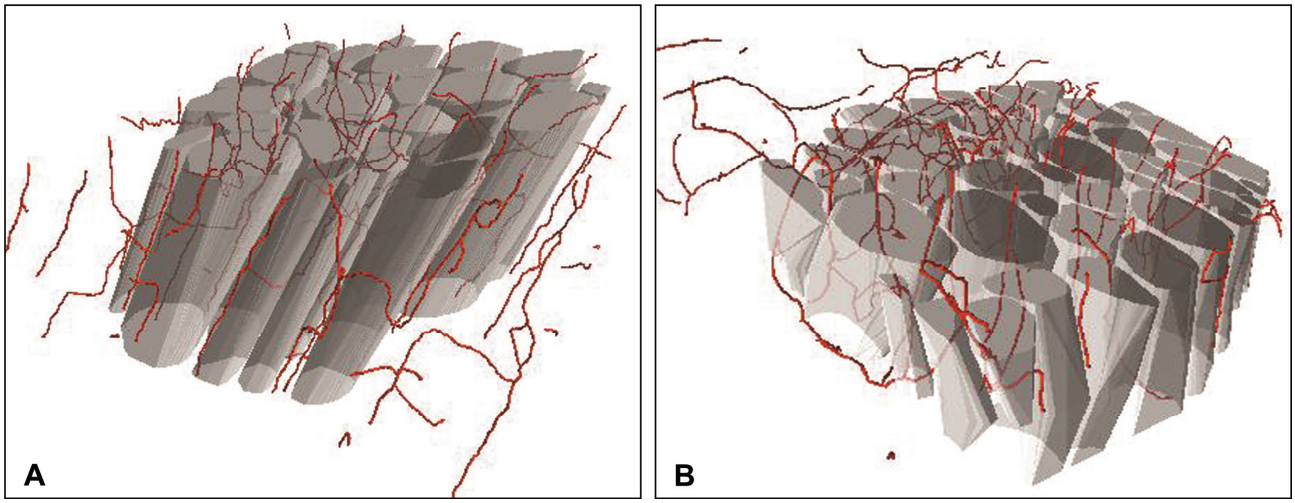

Fig. 2. *3D rendering of capillaries and muscle fibres in masseter muscle of young (a) and old (b) subjects.*

Table 1. *Capillary pattern in muscle samples of young and old subjects. Network characteristics were estimated by the length of capillaries per muscle volume (Lcap/Vmuscle [μm^{-2}])×10^{-6}, tortuosity [rad μm^{-1}]×10^{-3}, anisotropy, number of branchings per muscle volume (Nbr/Vmuscle [μm^{-3}]) ×10^{-6}, mean capillary length (Lbr [µm]). Post-mortem interval (PMI) [hours] is indicated for all but one sample.)*

	Sample	Age	PMI	Lcap/Vmuscle	Tortuosity	Anisotrpy	Lbr	Nbr/Vmuscle
Young	1	19.0	11	448.10	78.16	1.92	158.70	1.95
	2	29.0	26	746.34	41.91	2.49	178.38	2.85
	3	29.0	21	620.99	59.04	1.76	143.48	2.92
	4	35.0	14	629.61	80.55	2.47	189.64	2.24
	5	39.0	15	710.06	174.99	2.93	197.60	2.46
	6	19.0	25	583.39	99.94	1.75	90.27	4.47
	7	31.0	24	655.95	97.90	1.51	76.70	5.78
	8	26.0	18	520.14	70.95	1.80	109.74	3.36
	Avg	28.4		614.32	87.93	2.08	143.06	3.25
	SD	6.2		97.15	40.02	0.49	46.20	1.28
	SEM	2.2		34.35	14.15	0.17	16.33	0.45
	CV	21.8		15.81	45.51	23.56	32.29	39.38
Old	9	73.0	21	328.14	45.34	2.40	199.34	1.13
	10	84.0	48	723.05	87.97	2.41	264.06	1.85
	11	83.0	15	837.92	61.77	1.71	201.96	2.77
	12	79.0	21	429.84	54.30	1.92	161.99	2.52
	13	76.0	17	701.41	61.36	1.83	109.96	4.50
	14	84.0	-	813.27	49.70	2.70	169.24	3.42
	12	77.0	24	893.68	44.00	2.68	321.26	2.13
	16	70.0	22	747.08	61.11	2.56	133.85	3.96
	Avg	78.3		684.30	59.19	2.28	195.21	2.79
	SD	5.2		187.55	13.10	0.37	64.71	1.05
	SEM	1.7		66.31	4.63	0.13	22.88	0.37
	CV	6.7		27.41	22.51	16.23	33.15	37.63

Since most masseter muscles are composed of smaller type 2 and larger type 1 muscle fibres (Cvetko *et al.*, 2012) we estimated capillary characteristics around those two fibre types separately (Figs. 3a,b,c).

Length of capillaries per fibre length (Lcap/Lfib) was larger in type 1 fibre than in type 2 fibres in young subject, but not significantly different in old subjects. With ageing in type 1 fibres Lcap/Lfib dropped significantly ($p = 0.041$) while in type 2 fibres Lcap/Lfib showed tendency to decrease in samples of old subjects, Lcap/Sfib did not change with age, while Lcap/Vfib was significantly smaller in type 1 compared to type 2 fibres ($p = 0.032$).

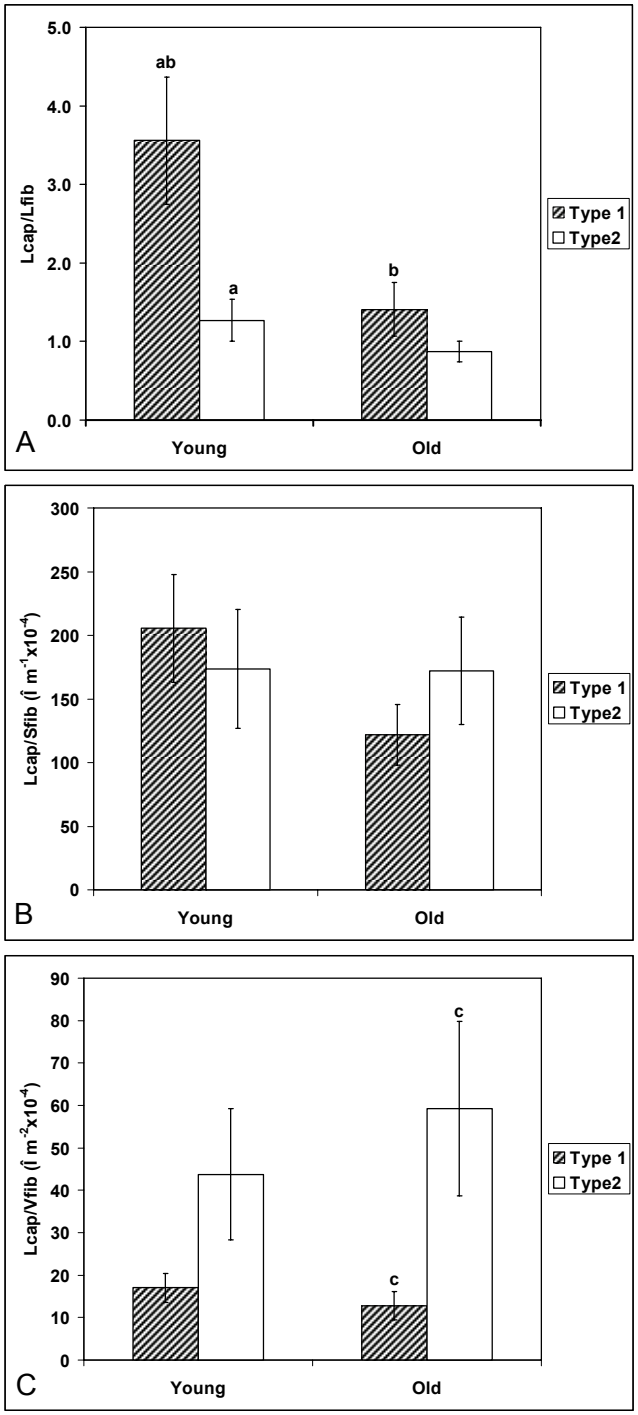

Fig. 3. *Capillary supply of muscle fibre types 1 and 2 in young and old human masseter muscles. Network characteristics were estimated by the length of capillaries A) per muscle fibre length (Lcap/Lfib), B) per muscle fibre surface area (Lcap/Sfib [μm^{-1}]$\times 10^{-4}$) and C) per muscle fibre volume (Lcap/Vfib [μm^{-2}] $\times 10^{-4}$), $^{a}P = 0.041$, $^{b}P = 0.026$, $^{c}P = 0.032$*

DISCUSSION

This study has proved that the length of capillaries per fibre length (Lcap/Lfib) was larger in type 1 fibres than in type 2 fibres in young subjects, but not significantly different in old subjects. With ageing in type 1 fibres Lcap/Lfib dropped significantly, while in type 2 fibres Lcap/Lfib showed just a tendency to decrease, Lcap/Sfib did not change with age, while Lcap/Vfib was significantly smaller in type 1 compared to type 2 fibres. There was a trend toward reduction in curvature and branch density with a consequent elongation of the average capillary branch length in the old group.

The characteristics of the capillary network were quite variable within every age group. Large interindividual variability in capillarity could reflect differences in muscle daily activity and loading pattern due to different craniofacial morphology, intermaxillary relationship and dental status, but also due to methodological problems that could not be totally overcome. All the data were obtained from autopsy material where it is much more difficult to ensure good tissue preservation. Moreover, to our knowledge it is practically impossible to control the extent of autolysis. In Janáček *et al.* (2011) we describe in detail the methodological problems that needed to be solved before we could get a good staining of capillaries through 100 μm muscle section. Further, although UAE lectin is an excellent marker for capillaries in human skeletal muscles, it did not function in several human autopsy muscle samples. Kadota *et al.* (1986) report that in case of stroke, the time of brain sample excision after stroke is decisive. Maybe, capillaries in skeletal muscles react similarly. We attempted to overcome this problem with additional staining of capillaries with collagen IV and F8. When one or the other marker did not function completely, it was still possible to identify capillaries. In case of complete absence of UAE binding the samples were discarded.

Most muscle samples were excised up to 26 hrs after death and one 48 hrs after death, therefore we assume that post-mortem changes affected all samples in a similar way, though we are well aware that the changes could not be absolutely comparable. We could not find any correlation between values of estimated parameters and the time post mortem. We observed lack of anastomoses especially in the old group. As

we were not able to find any marker of post-mortem changes - lack of anastomoses could also be ascribed to postmortal degradation and not only to changes due to ageing. Since we could not identify properly the postmortal changes, this is also a potential reason for great variability in our results.

CAPILLARY PATTERN IN MASSETER MUSCLE AT YOUNG AND OLD SUBJECTS

Data from the present study indicate that there are no significant age-related changes in capillarity of the masseter muscle as a whole; however, larger length of capillaries per unit muscle volume, reduction in curvature and branch density with a consequent elongation of the average capillary branch length point to remodelling of the capillary bed in old subjects. A tendency of larger length of capillaries per unit muscle fibre volume in old masseter muscle reflects smaller diameter of muscle fibres in old subjects. In our previous study in masseter muscle we presented a larger number of branches and greater tortuosity compared to vastus lateralis muscle and to multifidus muscle (Janáček *et al.*, 2011). Curvature and branch density seem to be muscle specific and may represent a compensatory mechanism in masseter muscle to improve diffusive capacity. The trend toward a higher degree of anisotropy, lower tortuosity and branch density found with ageing suggest the age related alteration in geometry in the capillarity in masseter muscle. A tendency toward decreased number of branches - anastomoses among longitudinally oriented capillaries - and decreased tortuosity in aged masseter suggest lower metabolic requirements of ageing muscle fibres.

Lower muscle capillarization is accompanied with lower VEGF expression (Croley *et al.*, 2005; Ryan *et al.*, 2006). Angiogenic potential seems not to be disturbed in masseter muscle with age. Although VEGF-164 is a predominant form in various tissues, the role of VEGF188 was reported in angiogenesis and capillary maintenance in the masticatory muscles (Ishii *et al.*, 2001). Since anatomical capillarization is well maintained in old masseter muscle, it could be speculated that VEGF188 is not downregulated with age.

Quantitative analysis of capillary supply to skeletal muscle is a prerequisite for understanding the limits to peripheral oxygen transport. This facilitates an increase in the exchange of O_2 and nutrients, the resistance to fatigue might thus be improved, especially in the small fast fibres. Consequently the smaller muscle fibres can be advantageous for masseter muscle. This is supported by findings in endurance test studies reporting that the jaw closing muscles resist fatigue better than arm and hand muscles (van Steenberghe *et al.*, 1978). Further, changes in capillary membrane permeability and differences in enzyme activity of the capillaries might reflect different ability of the muscles to resist fatigue and pain (Sjøgaard *et al.*, 1988).

We confirmed a better capillarization of type 1 than type 2 fibres in young subjects, but not in elder. This is congruent with a 2:1 ratio of capillary profiles supplying type 1 compared to type 2 fibres for the anterior portion and 6:1 for the posterior portion in the masseter muscle (Stål *et al.*, 1996) and denser capillary supply of type 1 compared to type 2 fibres regardless age and sex reported in PCA muscle (Lyon *et al.*, 2007).

Lcap/Lfib adjacent to type 1 fibres decreased significantly in masseter muscle in old subjects, which suggests that type 1 muscle fibres are less frequently activated with ageing (altered pattern of muscle use or innervation of type 1 fibres).

Type 1 fibres, which are representative of a slow twitch motor unit, are recruited at relatively low stimulations and are resistant to fatigue (Nordstrom and Miles, 1990). They are probably correlated with the maintenance of the tonic function in the masseter muscle at rest, which characterizes its function. This means that only type 1 fibres would be activated at small force level.

As a result of different daily activity pattern and different loading pattern the need and demand of blood supply to type 1 fibres change with ageing. Changed craniofacial morphology, such as reduced vertical dimension of the face and reduced weight of the mandible (teeth loss followed by bone resorption) impose reduced stretch on muscle fibres followed by reduced activity of type 1 fibres. Reduced metabolic needs of type 1 fibres provoke adjustment of capillary network adjacent to type 1 fibres. An age-associated decrease of type 1 fibres and increase in proportion of type 2 fibres were demonstrated in masseter muscle (Cvetko *et al.*, 2012). This data support a shift toward the less oxidative muscle phenotype. The age-related changes in terms of craniofacial morphology are paralleled by alterations in muscle fibre type composition (transitions to fast phenotype) and adjustment of capillarization adjacent to type 1 fibres.

Changes in the ratio of fibre types in jaw muscles based on MyHC expression could be due to age-related changes in neural or hormonal influences (Korfage *et al.*, 2005) and changed muscle use (Basu *et al.*, 2002). Muscular changes due to inactivity often occurring in

limb muscles do not happen in jaw muscles since habitual oral motor movements (chewing, talking, and swallowing) are maintained in elderly subjects. An important functional consequence of the observed apparent shift towards faster, therefore more powerful fibre types is that this shift may compensate for the loss of muscle power due to reduced mass in the old age.

Similarly to decreased proportion of type 1 fibres with age in masseter muscle data from human laryngeal thyroarythenoid muscle show that there is an age-related loss of type 1 fibres. This suggests that there is a combination of fibre transformations with a subsequent reorganization of the vasculature.

In young subjects the length of capillaries per fibre length (Lcap/Lfib) was significantly larger in capillaries adjacent to type 1 fibres than to type 2 fibres. Greater Lcap/Lfib in type 1 fibres compared to type 2 fibres is in concordance to findings that fast to slow fibre remodelling of the masticatory muscles also encompasses an increase in capillary density (Gedrange *et al.*, 2003), the capillary length supplying the fibre unit volume (Lcap/Vfib) is larger for type 2 fibres, *i.e.* the unit fibre volume, supplied by the unit capillary length is smaller in type 2 muscle fibres. This probably reflects the metabolic needs of type 2 fibres with predominantly glycolytic metabolism.

Our findings show that anatomic capillarity is well maintained in masseter muscle in old subjects. We conclude that alterations in the anatomic size of the capillary/fibre interface do not play a major role in the fall in skeletal muscle aerobic performance with ageing.

ACKNOWLEDGEMENTS

The present study was supported by the Slovenian Research Agency (P3-043) and by the public funds provided by the Academy of Sciences of the Czech Republic (AV0Z50110509 and RVO:67985823). We are grateful to Mrs. Nataša Pollak, Mrs. Majda Črnak-Maasarani, Mrs. Andreja Vidmar, Mr. Ivan Blažinovič, Mr. Marko Slak and Mr. Milan Števanec for their skilful technical assistance.

REFERENCES

Basu R, Basu A, Nair KS (2002). Muscle changes in aging. J Nutr Health Aging 6:336–41.

Brown M (1987). Change in fiber size, not number, in ageing skeletal muscle. Age Ageing 16:244–8.

Brown M, Cotter Ma, Hudlická O, Vrbová G (1976). The effects of different patterns of muscle activity on capillary density, mechanical properties and structure of slow and fast rabbit muscles. Pflugers Arch 361:241–50.

Coggan AR, Spina RJ, King DS, Rogers MA, Brown M, Nemeth PM, Holloszy JO (1992). Histochemical and enzymatic comparison of the gastrocnemius muscle of young and elderly men and women. J Gerontol 47: B71–6.

Cotter M, Hudlická O, Pette D, Staudte H, Vrbová G (1973). Changes of capillary density and enzyme pattern in fast rabbit muscles during long-term stimulation. J Physiol-London 230:34P–35P.

Croley AN, Zwetsloot KA, Westerkamp LM, Ryan NA, Pendergast AM, Hickner RC, *et al.* (2005). Lower capillarization, VEGF protein, and VEGF mRNA response to acute exercise in the vastus ateralis muscle of aged vs. young women. J Appl Physiol 99:1872–9.

Cvetko E, Karen P, Janáček J, Kubínová L, Plasencia AL, Eržen I (2012). Human masseter muscle fibres from the elderly express less neonatal myosin than those of young adults. Anat Rec (Hoboken) 295:1364–72.

Cui L, Ju Y, Ding L, Trejo-Morales M, Olfert IM (2008). Arteriolar and venular capillary distribution in skeletal muscles of old rats. Gerontol A Biol Sci Med Sci 63: 928–35.

Čebašek V, Eržen I, Vyhnal A, Janáček J, Ribarič S, Kubínová L (2010). The estimation error of skeletal muscle capillary supply is significantly reduced by 3D method. Microvasc Res 79:40–6.

Degens H, Turek Z, Hoofd LJC, Binkhorst RA (1994). Capillary proliferation related to fibre types in hypertrophied ageing rat m. plantaris. Adv Exp Med Biol 345:669–76.

Denis C, Chatard JC, Dormois D, Linossier MT, Geyssant A, Lacour JR (1986). Effects of endurance training on capillary supply of human skeletal muscle on two age groups (20 and 60 years). J Physiol (Paris) 81:379–83.

Dorph-Petersen KA, Nyengaard JR, Gundersen HJG (2001). Tissue shrinkage and unbiased stereological estimation of particle number and size. J Microsc 204:232–46.

Egginton S, Hudlická O (2000). Selective long-term electrical stimulation of fast glycolytic fibres increases capillary supply but not oxidative enzyme activity in rat skeletal muscles. Exp Physiol 85:567–73.

Eržen I, Janáček J, Kubínová L (2011). Characterization of the capillary network in skeletal muscles from 3D data. Physiol Res 60:1–13.

Frontera WR, Hughes VA, Fielding RA, Fiatarone MA, Evans WJ, Roubenhoff R (2000). Aging of skeletal muscle: a 12-year longitudinal study. J Appl Physiol 88:1321–6.

Gambino DR, Malmgren LT, Gacek RR (1990). Age-related changes in the neuromuscular junctions in the human posterior cricoarytenoid muscles: a quantitative study. Laryngoscope 100: 262–8.

Gedrange T, Walter B, Tetzlaff I, Kasper M, Schubert H, Harzer W, *et al.* (2003). Regional alterations in fiber type distribution, capillary density, and blood flow after

lower jaw sagittal advancement in pig masticatory muscles. J Dent Res 82:570–4.

Gundersen HJG, Boyce RW, Nyengaard JR, Odgaard A (1993) The Conneulor: unbiased estimation of connectivity using physical disectors under projection. Bone 14:217–22.

Hell S, Reiner G, Cremer C, Stelzer EHK (1993) Aberrations in confocal fluorescence microscopy induced by mismatches in refractive index. Microsc 169:391–405.

Hepple RT, Vogell JE (2004). Anatomic capillarization is maintained in relative excess of fibre oxidative capacity in some skeletal muscles of late middle-aged rats. J Appl Physiol 96:2257–64.

Ishii H, Oota I, Takuma T, Inomata K (2001). Developmental expression of vascular endothelial growth factor in the masseter muscle of rats. Arch Oral Biol 46:77–82.

Janáček J, Cvetko E, Kubínová L, Travnik L, Eržen I (2011). A novel method for evaluation of capillarity in human skeletal muscles from confocal 3D images. Microvasc Res 81:231–8.

Janáček J, Kreft M, Čebašek V, Eržen I (2012). Correcting the axial shrinkage of skeletal muscle thick sections visualized by confocal microscopy. J Microsc 246: 107–2.

Kadota E, Tanji K, Nishida S, Takahashi M, Maeda M, Hiruma S, *et al.* (1986). Lectin (UEA -1) reaction of capillary endothelium with reference to permeability in autopsied cases of cerebral infarction. Histol Histopathol 1:219–26.

Knust J, Ochs M, Gundersen HJG, Nyengaard JR (2009). Stereological estimates of alveolar number and size and capillary length and surface area in mice lungs. Anat Rec 292:113–22.

Korfage JA, Koolstra JH, Langenbach GE, van Eijden TM (2005). Fiber-type composition of the human jaw muscles (part 1) origin and functional significance of fiber-type diversity. J Dent Res 84:774–83.

Kubínová L, Janáček J, Ribarič S, Čebašek V, Eržen I (2001). Three-dimensional study of the capillary supply of skeletal muscle fibres using confocal microscopy. J Muscle Res Cell Motil 22:217–27.

Lyon MJ, Steer LM, Malmgren LT (2007). Stereological estimates indicate that aging does not alter the capillary length density in the human posterior cricoarytenoid muscle. J Appl Physiol 103:1815–23.

Mathieu-Costello O, Ju Y, Trejo-Morales M, Cui L (2005). Greater capillary-fibre interface per fibre mitochondrial volume in skeletal muscles of old rats. J Appl Physiol 99:281–9.

Mitchell ML, Byrnes WC, Mazzeo RS (1991). A comparison of skeletal muscle morphology with training between young and old Fischer 344 rats. Mech Ageing Dev 58: 21–35.

Nelissen-Vrancken HJ, Boudier HA, Daemen MJ, Smits JF (1993). Antihypertensive therapy and adaptive mechanisms in peripheral ischemia. Hypertension 22:780–8.

Nordstrom MA, Miles TS (1990). Fatigue of single motor units in human masseter. J Appl Physiol 68:26–34.

Nyengaard JR (1999). Stereologic methods and their application in kidney research (Review). J Am Soc Nephrol 10:1100–23.

Palágyi K, Kuba A (1998). A 3D 6-subiteration thinning algorithm for extracting medial lines. Pattern Rec Lett 19:613–27.

Proctor DN, Sinning WE, Walro JM, Sieck GC, Lemon PW (1995). Oxidative capacity of human muscle fiber types: effects of age and training status. J Appl Physiol 78:2033–8.

Ryan NA, Zwetsloot KA, Westerkamp LM, Hickner RC, Pofahl WE, Gavin TP (2006). Lower skeletal muscle capillarization and VEGF expression in aged vs. young men. J Appl Physiol 100:178–85.

Sjøgaard G (1982). Capillary supply and cross-sectional area of slow and fast twitch muscle fibres in man. Histochemistry 76:547–55.

Sjøgaard G, Savard G, Juel C (1988). Muscle blood flow during isometric activity and its relation to muscle fatigue. Eur J Appl Physiol Occup Physiol 57:327–35.

Stål P, Eriksson PO, Eriksson A, Thornell LE (1990). Enzyme-histochemical and morphological characteristics of muscle fibre types in the human buccinator and orbicularis oris. Arch Oral Biol 35:449–58.

Stål P, Eriksson PO, Thornell LE (1996). Differences in capillary supply between human oro-facial, masticatory and limb muscles. J Muscle Res Cell Motil 17:183–97.

Škorjanc D, Jaschinski F, Heine G, Pette D (1998). Sequential increases in capillarization and mitochondrial enzymes in low-frequency-stimulated rabbit muscle. Am J Physiol Cell Physiol 274:C810–8.

Štencel M, Janáček J (2006). On calculation of chamfer distance and Lipschitz covers in digital images. Proceedings S4G. Lechnerová R, Saxl I, Beneš V, eds. Prague, Union of Czech Mathematicians and Physicists, 517–22.

van Steenberghe D, De Vries JH, Hollander AP (1978). Resistance of jaw-closing muscles to fatigue during repetitive maximal voluntary clenching efforts in man. Arch Oral Biol 23:697–701.

Wulfson D, Knust J, Ochs M, Nyengaard JR, Gundersen HJG (2009) Stereological estimation of the total number of ventilator units in mice lungs. J Microsc 238: 75–89.

Image Anal Stereol 2013;32:145-153 doi:10.5566/ias.v32.p145-153
Original Research Paper

STEREOLOGICAL EVALUATION OF BRAIN MAGNETIC RESONANCE IMAGES OF SCHIZOPHRENIC PATIENTS

AMANI ELFAKI[✉,1], ABDELRAZAG ELFAKI[2], TAHIR OSMAN[3], BUNYAMIN SAHIN[1], ABDELGANI ELSHEIKH[3], AMIRA MOHAMED[4], ANAS HAMDOUN[5] AND ABDELRAHMAN MOHAMMED[3]

[1]Department of Anatomy, Medical School, Ondokuz Mayıs University, Samsun 55139, Turkey; [2]Department of Psychiatry, Ahfad University for Women, Omdurman, Sudan; [3]Departments of Anatomy, Psychiatry and Radiology, Faculty of Medicine, Ribat University, Burri 55 Khartoum, Sudan; [4]Tigani Almahi Psychiatric hospital, Khartoum, Sudan; [5] Gazira University, Faculty of Medicine, Department of Radiology, Wad Medani, Sudan
e-mail: amani.elfaki@omu.edu.tr, amanielfaki@gmail.com, bsahinomu@gmail.com, Abdelrazagelfaki@gmail.com, ali.taher56@yahoo.com, abdelghani55@hotmail.com, abdalrahmannoor@hotmail.com, Hamdoun11@hotmail.com, amiraharoun@hotmail.com
(Received March 7, 2013; revised July 11, 2013; accepted August 8, 2013)

ABSTRACT

Advances in neuroimaging have enabled studies of specific neuroanatomical abnormalities with relevance to schizophrenia. This study quantified structural alterations on brain magnetic resonance (MR) images of patients with schizophrenia. MR brain imaging was done on 88 control and 57 schizophrenic subjects and Dicom images were analyzed with ImageJ software. The brain volume was estimated with the planimetric stereological technique. The volume fraction of brain structures was also estimated. The results showed that, the mean volume of right, left, and total hemispheres in controls were 551, 550, and 1101 cm^3, respectively. The mean volumes of right, left, and total hemispheres in schizophrenics were 513, 512, and 1026 cm^3, respectively. The schizophrenics' brains were smaller than the controls ($p < 0.05$). The mean volume of total white matter of controls (516 cm^3) was bigger than the schizophrenics' volume (451 cm^3), ($p < 0.05$). The volume fraction of total white matter was also lower in schizophrenics ($p < 0.05$). Volume fraction of the lateral ventricles was higher in schizophrenics ($p < 0.05$). According to the findings, the volumes of schizophrenics' brain were smaller than the controls and the volume fractional changes in schizophrenics showed sex dependent differences. We conclude that stereological analysis of MR brain images is useful for quantifying schizophrenia related structural changes.

Keywords: brain, Cavalieri principle, magnetic resonance images, schizophrenia, stereology, volume, volume fraction

INTRODUCTION

Advances in neuroimaging have cleared the way for studies on specific neuroanatomical abnormalities with relevance to schizophrenia. Schizophrenia is a psychotic disorder with delusions, hallucinations, disorganized behavior and speech, and negative symptoms (Spitz and Sadock, 1973). Despite its unknown etiology, Bleuler, who first described the disease, in a lecture in Berlin on 24 April 1908, believed that a relationship between the structural brain abnormalities and the etiology of schizophrenia exists (Peralta and Cuesta, 2011).

With the first magnetic resonance imaging (MRI) study in schizophrenia by Smith *et al.* (1984), the researchers were offered a unique opportunity to examine special brain areas in live patients. Unlike computed tomography (CT) scan, MRI can discriminate the grey and white matter of brain with much better resolution, so that MRI has become the imaging modality of choice in evaluation of the brain changes during schizophrenia (Shenton *et al.*, 2001).

When evaluating the volumes of different structures in the brain, it is necessary to determine the total cerebral volume to find out if the change in the volume of those structures is secondary to overall changes in the cerebral volume or has occurred independently. MRI studies have reported changes in the brain volume (Sanfilipo *et al.*, 2000), and the volume of lateral ventricles (Rajarethinam *et al.*, 2000). Moreover, some studies suggested that brain morphology could predict the course of the disease and the outcome for neuroleptic drugs used (Ebdrup *et al.*, 2011).

The majority of structural brain imaging studies in schizophrenia, thus far, have been confined to adult

subjects, only a few studies have explored whole-brain changes in early-onset schizophrenia on a morphometric basis (Sowell *et al.*, 2000; Thompson *et al.*, 2001; Vidal *et al.*, 2006). Despite a prolific literature, the structural cerebral changes revealed in adult-onset schizophrenia have previously shown great inconsistencies, partly due to the heterogeneity of the methods applied and to methodological problems in working with this patient population, such as the appropriate interpretation of the enlargement of ventricles (Kubicki *et al.*, 2005; Walterfang *et al.*, 2006; Kubicki *et al.*, 2007). In performing the work described here, advantage of recent advances in grey matter stereology and white matter integrity analyses was taken, as well as the lateral ventricular volume in appropriate statistical inferences.

Many biomedical studies have applied unbiased stereological methods in combination with non-invasive MRI (Gong *et al.*, 1998). For example, the reliability of the Cavalieri estimator and point counting in combination with MRI to estimate the volume of biological structures based on systematic sampling has been investigated in several studies (Gundersen *et al.*, 1999). However, the accuracy of these estimators has been evaluated by only a few researchers (Doherty *et al.*, 2000; Garcia-Finana *et al.*, 2003).

The aim of the present study was the stereological quantification of schizophrenia related brain changes on MRI in combination with stereology, to detect structural alterations of the cerebrum in schizophrenics. It also aims to present what Hippocrates already knew in the fourth century B.C. “almost everything that we think, do and feel derive from the brain. Mental illness arises from the brain when it is not healthy”. The repeatability and reproducibility of procedure in this study was investigated to ensure consistency of the measurements.

MATERIAL AND METHODS

88 control subjects (51 male, 37 female) and 57 schizophrenic patients (30 male, 27 female) participated in the present study. The total number of volunteers was 145. The details of the mean of ages and body mass index of the participants are describe in the table 1. The study was approved by the Ethical Committee of the Gezira University/ Sudan. Patients or patient’s relatives and controls consented to all procedures.

CRITERIA OF SELECTION

Adults Sudanese who are clinically diagnosed as schizophrenic patients. All schizophrenic patients met ICD/10 criteria and were receiving regular antipsychotic medication. The patients were selected from: Professor Abdelaal Alidresi Psychiatric hospital, Tigani Almahi Psychiatric hospital, and private psychiatric clinics in Sudan.

Controls were Sudanese volunteers with no history of psychiatric disorders and drug medication. Control subjects were matched with patients on the basis of gender and age.

Exclusion criteria for both patients and controls include a head trauma, drug abuse and central neurological disorders.

MRI ACQUISITION

Structural MRI was done to both patients and controls in the Department of Radiology in the National Ribat University. The MR scanner used was a SIEMENS 1.5 Tesla Magnetom Avanto Vision System. T1-weighted images were obtained using three-dimensional acquisition by Magnetization Prepared Rapid Acquisition (MP-RA); it produces good grey/white matter contrast in a very short acquisition time. Slice distance was 1.0 mm, the field of view was 250 read, 192 mm phase, TR = 1657 ms, TE = 2.95 ms, bandwidth 180 Hz/pixel, flip angle 15°, ECHO spacing = 7.5 ms, phase resolution = 100%, slice resolution = 50%, and acquisition time = 5 min and 18 sec. The images were made in the coronal section.

This T1-weighted sequence is part of the standard clinical protocol for qualitative and quantitative analysis of the whole brain in patients with epilepsy.

METHODS OF MEASUREMENTS

Morphometric measurements were conducted blind to the clinical data using ImageJ software. The ImageJ is produced and distributed by the National Institute of Health (NIH). The software is in the public domain and was downloaded from the Internet (available at the site: http://rsb.info.nih.gov/ij/). It runs on any computer system. Measurements from images can be stored separately. The Dicom brain images were transferred to the ImageJ software and converted into a stack. Systematic random sampling was done since the number of slices in coronal plane was about 192 sections. The sampling fraction was 1/10 and 1/5 for the brain and ventricles, respectively. This means, for example taking the 5^{th} section as first, then going on to the sections 15, 25, 35 for the brain. Therefore, the section interval for the brain was 1 cm and for the ventricle 0.5 cm. Finally 15 to 17 sections containing brain images and 14 to 20 sections containing ventricles were obtained.

The midline of the brains and possible borders of the hemispheres were drawn on the images to delineate them from the surrounding tissues (Fig. 1A). The outer boundaries of the hemisphere were manually delineated (Fig. 1B). A threshold tool was used to delineate the boundaries of the white matter, and then the wand tool was used to delineate the boundaries of the hemispheres (Fig. 1C). This procedure was also done for the ventricles (Fig. 1D). The sectional cut surface of the structure of interest was measured by the software automatically. The volume of cerebral hemispheres, ventricles and white matter was estimated by the multiplication of the total sectional surface area with the section interval (*i.e.*, 1 cm and 0.5 cm for the hemisphere and ventricle, respectively) as it shown in the formula

$$V = \sum a \times t,$$

where, V is the volume, $\sum a$ is the total sectional area of the structure and t is the space between the examined sections.

The total brain volume was estimated by summating the volumes of both hemispheres, and grey matter volume was obtained by subtracting the volume of white matter and ventricles from the total hemispheric volume.

For the measurements of the volume fraction the following formula was used:

$$\text{Volume fraction} = \frac{\text{Volume of } X \text{ phase in } Y \text{ reference space}}{\text{Volume of } Y \text{ reference space}},$$

where the $V_V(X, Y)$ indicates volume fraction of X phase within the Y reference volume. Using this approach, V_V (hippocampus, brain), V_V (cortex, total brain volume) and V_V (tumor, hemisphere) can be estimated. Volume fraction ranges from 0 to 1 and is often expressed as a percentage.

In the planimetry method, the coefficient of error (CE) of estimates was obtained using the following formula:

$$CE = \left(\sum_{i=1}^{n} A_i\right)^{-1} \times \left[\frac{1}{240}\left(3\sum_{i=1}^{n} A_i^2 - 4\sum_{i=1}^{n-1} A_i A_{i+1} + \sum_{i=1}^{n-2} A_i A_{i+2}\right)\right]^{1/2}.$$

Where, i = 1, 2, …, m is the number of sections. A is the measured area of the sections using planimetry and the others are constants. This formula allows the researcher to evaluate the area changes and the measured cut surface areas in the consecutive section series (Mazonakis *et al.*, 2002).

The calculations and the CE values were done with Microsoft Excel. A spreadsheet was prepared and the surface area data were transferred from ImageJ to Excel where the calculations were done automatically.

Two weeks later the same procedure was applied and the same observer obtained the volume data. The details of the intra-rater variation are reported in the paper published by Elfaki *et al.* (2011).

Wilcoxon's signed-rank test was applied to compare the results of first and second sessions. Pearson correlation test was done to see the relation between the two session's values. A p value of 0.05 or less was accepted as statistically significant.

ANALYSIS

Data analysis was performed on a personal computer using the Statistical Package for Social Science (SPSS, Version 15). The data was collected on a master sheet designed for that purpose.

Independent sample T-test was used to compare the measurements of cerebral structures between controls and schizophrenics. The estimation result of the same observer between two sessions, the Wilcoxon Signed Rank Test was applied.

Table 1. *Comparison of the mean age and body mass index (BMI) between controls and schizophrenics*.

		The mean of age (Years) (±SD)	The mean of BMI (kg/m^2) (±SD)
Male	Control	28 (±SD 5.97)	24 (±SD 4.02)*
	Schizophrenic	30 (±SD 5.97)	22 (±SD 3.49)*
Female	Control	29 (±SD 6.14)	25 (±SD 4.83)
	Schizophrenic	31 (±SD 6.77)	24 (±SD 6.31)
Total	Control	29 (±SD 6.01)	25 (±SD 3.38)*
	Schizophrenic	31 (±SD 6.31)	23 (±SD 5.08)*

*$p < 0.05$

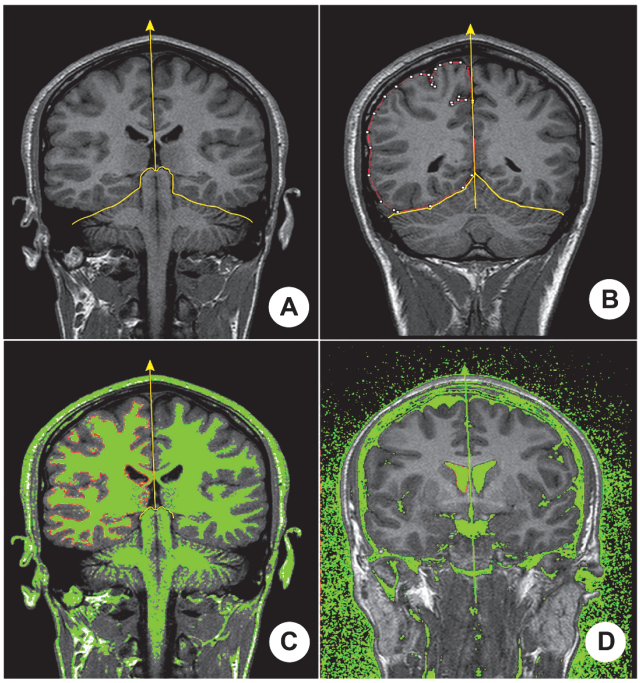

Fig. 1. *Estimation of the hemispheres, white matter and ventricular size of the brains using the imageJ. A. Splitting the brain into two hemispheres in the midline and separating the cerebellum and brainstem from the hemispheres, B. Delineation the boundaries of the hemispheres, C. Threshold image for the measurement of white matter area, D. Threshold image for the measurement of lateral ventricle area.*

RESULTS

Evaluation of the volume and volume fraction of the hemispheres

The volumes of right, left hemispheres and total volume of hemispheres showed differences between males and females within the groups and across the groups. The volumes of males were higher than the volumes of females. The volumes of schizophrenic patients were less than that of the controls. (Table 2)

The volume and the volume fraction of the right hemisphere were slightly larger than the left hemisphere. However, it did not reach to a statistically significant level. This means that the hemispheres were symmetrical both for the schizophrenic patients and controls (Table 2).

Evaluation of the volume and volume fraction of the white matter

The volumes of right, left hemispheric white matters and total volume of white matter were larger in controls than the schizophrenic patients both for males and females. In controls, there were no differences for the volumes of white matters between males and females. However, the volumes of white matter in males were less than females in schizophrenic patients (Table 3).

The volume fraction of white matter in schizophrenic patients was less for the right, left and total hemispheres indicating that the disease resulted in decrease of white matter. While the volume fractions of white matter of males were slightly lower in controls, but it did not reach to a statistically significant level. The volume fraction of white matter of males was extremely lower than the females in schizophrenic patients indicating that the volume fractional changes were severe in males compared to females in schizophrenics (Table 3).

Evaluation of the volume and volume fraction of the grey matter

The volumes of right, left hemispheric grey matter and total volume of grey matter did not differ between controls and schizophrenic patients. The volumes of right, left and total grey matters of males were higher in controls and schizophrenic patients. The volumes of grey matter of schizophrenic patients in males were higher than the controls. However, it did not reach to a statistical significant level (Table 4).

Table 2. *Comparison of the mean volume and volume fraction of the cerebral hemisphere between controls and schizophrenics.*

		Volume (cm^3) - CV (%) of hemisphere			Volume fraction (%) - CV (%) of hemisphere	
		Right	Left	Total	Right	Left
Male	Control	569* (7.90)	568* (7.78)	1140* (7.78)	50.1 (0.92)	49.9 (0.92)
	Schizophrenic	543* (7.94)	541* (8.65)	1085* (8.19)	50.1 (1.32)	49.9 (1.32)
Female	Control	524* (7.69)	525* (7.45)	1050* (7.54)	50.0 (0.72)	50.0 (0.72)
	Schizophrenic	480* (8.01)	480* (8.10)	961* (8.03)	50.0 (0.56)	50.0 (0.56)
Total	Control	551* (8.8)	550* (8.6)	1101* (8.6)	50.0 (0.8)	50.0 (0.8)
	Schizophrenic	513* (10.0)	512* (10.3)	1026* (10.1)	50.1 (1.0)	49.9 (1.0)

*$p < 0.05$

Table 3. *Comparison of the mean of the volume and volume fraction of the white matter between controls and schizophrenics.*

		Volume (cm^3) - CV (%) of white matter			Volume fraction (%) - CV (%) of white matter		
		Right	Left	Total	Right	Left	Total
Male	Control	271* (18.2)	253* (18.2)	525* (18.1)	47.7* (17.0)	44.7* (17.6)	46.2* (17.2)
	Schizophrenic	230* (16.4)	215* (16.1)	445* (16.1)	42.4* (15.6)	39.8* (14.7)	41.1* (15.0)
Female	Control	257* (16.5)	243* (16.3)	500* (16.3)	49.1 (15.3)	46.3 (15.3)	47.7 (15.2)
	Schizophrenic	236* (15.8)	223* (15.8)	459* (15.4)	49.1 (13.2)	46.5 (13.8)	47.8 (13.3)
Total	Control	265* (17.6)	249* (17.5)	515* (17.4)	48.3* (16.3)	45.4* (16.6)	46.8* (16.3)
	Schizophrenic	233* (16.0)	219* (15.7)	451* (15.7)	45.6* (16.1)	43.0* (16.2)	44.3* (15.9)

*$p < 0.05$

Table 4. *Comparison of the mean of the volume and volume fraction of the grey matter between controls and schizophrenics.*

		Volume (cm^3) - CV (%) of grey matter			Volume fraction (%) - CV (%) of grey matter		
		Right	Left	Total	Right	Left	Total
Male	Control	299 (18.3)	315 (17.5)	613 (17.7)	52.3* (15.5)	55.3* (14.2)	53.9* (14.8)
	Schizophrenic	313 (14.9)	326 (13.7)	640 (14.1)	57.6* (11.5)	60.2* (9.7)	58.9* (10.4)
Female	Control	267* (17.1)	282* (15.7)	549* (16.3)	50.9 (14.7)	53.7 (13.2)	52.3 (13.8)
	Schizophrenic	245* (15.1)	257* (15.2)	502* (14.9)	50.9 (12.7)	53.5 (12.0)	52.2 (12.1)
Total	Control	285 (18.6)	301 (17.6)	586 (18.0)	51.7* (15.2)	54.6* (13.8)	53.2* (14.4)
	Schizophrenic	281 (19.4)	294 (18.6)	574 (18.8)	54.4* (13.4)	57.0* (12.2)	55.7* (12.6)

*$p < 0.05$

The volume fraction of grey matter in schizophrenic patients was higher for the right, left and total hemispheres indicating that the disease resulted in increase of grey matter. While the volume fractions of grey matters of females were slightly lower in controls, it did not reach to a statistically significant level. The volume fraction of grey matter of females did not show difference between the controls and schizophrenic patients (Table 4).

Evaluation of the volume and volume fraction of the lateral ventricles

The volumes of right, left lateral ventricles and total volume of lateral ventricles were higher in schizophrenic patients than controls. However, it did not reach to a statistically significant level. The volumes of right, left and total volume of lateral ventricles did not differ between males and females in controls. The volumes of the left and total lateral ventricles were higher in males than females in schizophrenic patients (Table 5).

The volume fraction of lateral ventricles in schizophrenic patients was higher for the right, left and total hemispheres indicating that the disease resulted in increase of lateral ventricles. The volume fraction of left, right and total lateral ventricles did not show difference between males and females in both controls and schizophrenic patients (Table 5).

Coefficient of error (CE) estimation results for the volume data

The CE of volume was estimated. The details of the CE values are given in (Table 6).

Evaluation of the intra-rater variation for the estimation of volume of cerebral structures

The mean total brain volumes of 30 subjects were 1090 cm^3 and 1087 cm^3 for the first and second sessions, respectively. The mean total white matter volumes were 537 cm^3 for the first and second sessions, respectively. They were 554 cm^3 and 549 cm^3 for the total gray matter volumes in two sessions, respectively. The values for the total ventricular volumes were the same for both sessions, 14.3 cm^3. Statistical analysis of the data obtained in the first and second sessions did not differ from each other ($p > 0.05$).

The correlation analysis of the estimates showed that there were high correlations between the first and second sessions. The correlation coefficient (r) for the total brain, total white matter, total grey matter and total ventricles were 0.99.

Table 5. *Comparison of the mean of the volume and volume fraction of the lateral ventricles between controls and schizophrenics.*

		Volume (cm^3) - CV (%) of lateral ventricles			Volume fraction (%) - CV (%) of lateral ventricles		
		Right	Left	Total	Right	Left	Total
Male	Control	6.96 (48.6)	7.6* (50.8)	14.6 (47.7)	1.22 (47.5)	1.33* (47.4)	1.28* (45.3)
	Schizophrenic	7.70 (35.5)	9.22* (34.2)	16.9 (32.0)	1.42 (35.9)	1.70* (31.8)	1.56* (31.4)
Female	Control	6.13 (33.9)	7.06 (44.2)	13.2 (36.8)	1.17 (32.5)	1.33* (38.3)	1.25* (32.8)
	Schizophrenic	6.68 (30.1)	7.51 (28.9)	14.2 (28.5)	1.39 (27.3)	1.56* (25.6)	1.47* (25.9)
Total	Control	6.61 (44.2)	7.39 (48.3)	14.0 (44.1)	1.20* (42.5)	1.33* (43.6)	1.26* (40.5)
	Schizophrenic	7.22 (33.9)	8.41 (33.5)	15.6 (31.8)	1.41* (31.9)	1.63* (29.4)	1.52* (28.9)

*$p < 0.05$

Table 6. *The mean coefficient of error (%) values of the volume estimations.*

		Right hemisphere	Left hemisphere	Left white matter	Right white matter	Right ventricle	Left ventricle
Male	Control	0.07	0.17	0.33	0.33	0.58	0.51
	Schizophrenic	0.18	0.18	0.31	0.33	0.50	0.41
Female	Control	0.17	0.17	0.32	0.33	0.65	0.50
	Schizophrenic	0.17	0.17	0.32	0.33	0.54	0.47
Total	Control	0.17	0.17	0.32	0.33	0.61	0.50
	Schizophrenic	0.18	0.18	0.31	0.33	0.52	0.44

Bland and Altman analysis (Chap 2003) was also applied to see the agreement between to session. There was a good agreement between the sessions.

DISCUSSION

The main findings of this study are that the schizophrenic patients had a reduced total cerebral (7.33%), white matter (14%), and grey matter (2.12%) volumes and enlarged lateral ventricular volumes (11.7%). Alterations of the left hemisphere in schizophrenia are found more consistently than that of the right.

The current study supports the finding of Shenton *et al.* (2001), The current study supports the finding of Shenton (2001), who reported the left hemisphere to be less dense than the right in twins with schizophrenia, who reported the left hemisphere to be less dense than the right in a twin with schizophrenia, while the reverse was true for their healthy co-twin and control subjects. These results imply that left hemisphere abnormality is environmentally acquired, rather than a genetic trait. The right hemisphere, especially the temporal area, develops earlier than the left for a short period of time (Geschwind and Galaburda, 1985). Therefore, if there were an insult to the fetal brain in the process of neurodevelopment, the left hemisphere would be more prone to disruption, which could be related to the pathogenesis of schizophrenia.

Although some researchers did not detect any significant difference between the cerebral hemispheric volumes of the schizophrenic patients and the healthy individuals, some others believe that in schizophrenia the cerebrum is smaller than normal. The present findings of reductions converge mostly with Olabi *et al.* (2011), they found that patients with schizophrenia showed significantly greater decreases over time than controls in whole-brain volume, whole-brain gray matter, frontal gray and white matter, parietal white matter, and temporal white matter volume, as well as larger increases in lateral ventricular volume.

However, there has been considerable variability in results of schizophrenia MRI studies. A number of factors may contribute to this variability, including differences in analysis methods, variability in the disorder itself, and also due to variations in sampling selection and recruitment biases concerning both patient and control samples.

On the other hand, findings of an informative quantitative postmortem schizophrenia studies support a tendency towards a slightly reduced cortical volume, without any major global deficits in cortical cell number. The field is moving toward more targeted studies of specific cell types in specific cortical areas, including laminar analyses. Although such studies have detected schizophrenia-related cortical changes, more studies are needed before a consensus can be reached (Dorph-Petersen and Lewis, 2011).

White matter reductions were bilateral and widespread in this study. Some studies concentrate on grey matter findings, 7 studies included in the meta-analysis by Honea *et al.* (2005), had looked into only grey matter, whereas 7 studies had explored both tissues, and only one was restricted to white matter. Hence, the literature supporting white matter loss is not yet as strong that documenting grey matter deficit (Wright *et al.*, 2000). However, the findings of present study imply that there are significant deficits in regional white matter tissue in schizophrenia, which can be interpreted as a loss of organization of the fibers and alteration of the myelin, and thus, white matter should not be overlooked in future morphometric studies.

The regional grey matter reductions observed in females are broadly consistent with those reported in previous structural MRI studies. In keeping with the existing literature it has been shown in this study that patients with schizophrenia have significantly lower total and regional grey matter volume when compared to age and sex matched healthy volunteers (Kasai *et al.*, 2002). Some studies, however, have failed to reproduce these relationships (Paillere-Martinot *et al.*, 2001). The findings of male schizophrenics in this study were quite different than those reported in the literature.

When considering differences between the study's findings, it is important to note that there are different measures calculated in different ways, and need not necessarily yield identical results. Thus, a straightforward interpretation of such differences is that they reflect regional heterogeneity in underlying pathological mechanisms. This view is consistent with ongoing debate over the cause of MRI-based grey matter reductions (Weinberger and McClure, 2002; Mathalon *et al.* 2003), and evidence that such reductions may not necessarily result from a unitary process (Fornito *et al.*, 2009). For example, reductions in neuron density have commonly been found in post-mortem studies of medial temporal, medial prefrontal and thalamic regions in schizophrenic patients (Todtenkopf *et al.*, 2005), whereas increased neuronal density, accompanied by reduced synaptic density, has been a replicated finding in lateral prefrontal areas (Glantz and Lewis, 2001).

Other authors (Sowell *et al.*, 2003; Paus, 2005) have drawn attention to the substantial contributions made by non-neuronal tissue to grey matter estimates in T1- weighted imaging, implying that up to 1/3 of the signal may originate from intracortical white matter (Braitenberg, 2001). These findings imply that grey matter reductions observed with MRI, can arise from changes to several different tissue compartments, including neurons, glia, and their processes. Better understanding of how different histopathological changes affect MRI based grey matter changes is necessary to constrain future interpretation of neuroimaging findings. Therefore, in this study, the grey matter decreases found on MRI could be explained by either cell death and/or atrophy in females.

In schizophrenia patients, lateral ventricle enlargement is associated with smaller cortical and subcortical grey matter volumes (Weinberger and McClure, 2002). White matter reduction in proximity of the lateral ventricles can also be considered as an index of lateral ventricle enlargement (Price *et al.,* 2006). In vivo imaging studies and post-mortem investigations have led to the conclusion that the most important morphological abnormality in schizophrenia brains is ventricular enlargement relative to ventricular size in healthy controls. Although larger lateral ventricles are the most common finding in the schizophrenia, it is not specific and can be found in a number of other disorders such as Alzheimer's disease, hydrocephalus, and Huntington's chorea. In general, enlarged lateral ventricles are interesting findings which can indicate paraventricular neuronal tissue loss or embryonic dysgenesis (Shenton *et al.*, 2001).

The present results imply that there could be a neuroanatomical basis in the lateral ventricle volume differences between patients with schizophrenia and normal subjects; the lateralized ventricular differences that concern the left hemisphere, as numerous studies have implied that large ventricles in schizophrenia simply reflect diffuse brain atrophy. Rather, focal shrinkage in distinct gray matter regions involved in the pathophysiology of the disorder and adjacent to the ventricles might be a main contributor to this effect. This could also explain the variability in localization and extent of ventricular changes in schizophrenia. (Gaser *et al.*, 2004)

In the present study, the patients using typical and atypical antipsychotic medication there was a relative decrease in the volumes of the two hemispheres and grey matter in addition to decrease in the volume fraction of the white matter over the interval compared with controls. At the same time we do not find evidence for ventricular volume changes.

Our findings imply that antipsychotic treatment may contribute to brain tissue volume loss. More recent literature reviews have highlighted the potential role of antipsychotics in influencing brain volume deficits in schizophrenia and its implications (Navari and Dazzan, 2009).

The present findings of reductions meet mostly with the findings of Ho *et al.* (2011), which noticed

although antipsychotics relieve psychosis and its attendant suffering, these drugs may not arrest the pathophysiologic processes underlying schizophrenia and may even aggravate progressive brain tissue volume reductions.

CONCLUSION

Male schizophrenic patients had a higher grey matter volume than the controls. The volume fraction of grey matter in male schizophrenic patients was highest among the four groups in the study. While the grey matter volume fraction is symmetrical for controls and schizophrenic females, it was asymmetrical for the male schizophrenics. The left grey matter volume fraction was higher than the right one. Finally, in male patients, the lateral ventricles were asymmetrical and the volume fraction of left one was higher than the right lateral ventricles.

ACKNOWLEDGEMENTS

The authors are highly indebted to the technicians of the department of radiology in the National Ribat University/ Sudan, for their great contribution to this study and to the subjects who participated in collection of data.

This study was supported by the Organization for Women in Science for the Developing World (OWSDW)/ Italy and the Ministry of Higher Education/ Sudan. The topic of this paper was presented at the S4G Conference, June 25-28, 2012 in Prague, Czech Republic.

REFERENCES

Braitenberg V (2001). Brain size and number of neurons: an exercise in synthetic neuroanatomy. J Comput Neurosci 10:71–7.

Chap TE (2003). Comparison of population means. Introductory biostatistics (1). John Wiley and Sons. Canada, 246–81.

Doherty CP, Fitzsimons M, Holohan T, Mohamed HB, Farrell M, Meredith GE (2000). Accuracy and validity of stereology as a quantitative method for assessment of human temporal lobe volumes acquired by magnetic resonance imaging. Magn Reson Imaging 18:1017–25.

Dorph-Petersen KA, Lewis DA (2011). Stereological approaches to identifying neuropathology in psychosis. Biol Psychiatry 69:113–26.

Ebdrup BH, Skimminge A, Rasmussen H, Aggernaes B, Oranje B, Lublin H (2011). Progressive striatal and hippocampal volume loss in initially antipsychotic-naive, first-episode schizophrenia patients treated with quetiapine: relationship to dose and symptoms. Int J Neuropsychopharmacol 14:69–82.

Elfaki A; Osman T; Elsheikh A, Hamdoun A; Sahin B (2011). Evaluation of the intra-rater variation for the estimation of volume of cerebral structures using the cavalieri principle on magnetic resonance images. J Exp Clin Med 28:22–5.

Fornito A, Yucel M, Dean B, Wood SJ, Pantelis C (2009). Anatomical abnormalities of the anterior cingulate cortex in schizophrenia: bridging the gap between neuroimaging and neuropathology. Schizophr Bull 35:973–93.

Garcia-Finana M, Cruz-Orive LM, Mackay CE, Pakkenberg B, Roberts N (2003). Comparison of MR imaging against physical sectioning to estimate the volume of human cerebral compartments. Neuroimage 18:505–6.

Gaser C, Nenadic I, Buchsbaum BR, Hazlett EA, Buchsbaum MS (2004). Ventricular enlargement in schizophrenia related to volume reduction of the thalamus, striatum, and superior temporal cortex. Am J Psychiatry 61:154–6.

Geschwind N, Galaburda AM (1985). Cerebral lateralization. Biological mechanisms, associations, and pathology: I. A hypothesis and a program for research. Arch Neurol 42:428–59.

Glantz LA, Lewis DA (2001). Dendritic spine density in schizophrenia and depression. Arch Gen Psychiatry 58: 203.

Gong QY, Roberts N, Garden AS, Whitehouse GH (1998). Fetal and fetal brain volume estimation in the third trimester of human pregnancy using gradient echo MR imaging. Magn Reson Imaging 16:235–40.

Gundersen HJ, Jensen EB, Kiêu K, Nielsen J (1999). The efficiency of systematic sampling in stereology - reconsidered. J Microsc 193:199–211.

Ho BC, Andreasen NC, Ziebell S, Pierson R, Magnotta V (2011). Long-term antipsychotic treatment and brain volumes: A longitudinal study of first-episode schizophrenia. Arch Gen Psychiatry 68:128–37.

Honea R, Crow TJ, Passingham D, Mackay CE (2005). Regional deficits in brain volume in schizophrenia: a meta-analysis of voxel-based morphometry studies. Am J Psychiatry 162:2233–45.

Kasai K, Iwanami A, Yamasue H, Kuroki N, Nakagome K, Fukuda M (2002). Neuroanatomy and neurophysiology in schizophrenia. Neurosci Res 43:93–110.

Kubicki M, McCarley RW, Shenton ME (2005). Evidence for white matter abnormalities in schizophrenia. Curr Opin Psychiatry 18:121–34.

Kubicki M, McCarley R, Westin CF, Park HJ, Maier S, Kikinis R (2007). A review of diffusion tensor imaging studies in schizophrenia. J Psychiatr Res 41:15–30.

Mathalon DH, Rapoport JL, Davis KL, Krystal JH (2003). Neurotoxicity, neuroplasticity, and magnetic resonance imaging morphometry. Arch Gen Psychiatry 60:848–9.

Mazonakis M, Damilakis J, Maris T, Prassopoulos P, Gourtsoyiannis N (2002). Comparison of two volumetric techniques for estimating liver volume using magnetic resonance imaging. J Magn Reson Imaging 15: 557–63.

Navari S, Dazzan P (2009). Do antipsychotic drugs affect brain structure? a systematic and critical review of MRI findings. Psychol Med 39:1763–77.

Olabi B, Ellison-Wright I, McIntosh AM, Wood SJ, Bullmore E, Lawrie SM (2011). Are there progressive brain changes in schizophrenia? A meta-analysis of structural magnetic resonance imaging studies. Biol Psychiatry 70: 88–96.

Paillere-Martinot M, Caclin A, Artiges E, Poline JB, Joliot M, Mallet L (2001). Cerebral gray and white matter reductions and clinical correlates in patients with early onset schizophrenia. Schizophr Res 50:19–26.

Paus T (2005). Mapping brain maturation and cognitive development during adolescence. Trends Cogn Sci 9:60–8.

Peralta V, Cuesta MJ (2011). Eugen Bleuler and the schizophrenias: 100 years after Schizophr Bull 37:1118–20.

Price G, Cercignani M, Bagary MS, Barnes TR, Barker GJ, Joyce EM (2006). A volumetric MRI and magnetization transfer imaging follow-up study of patients with firstepisode schizophrenia. Schizophr Res 87:100–8.

Rajarethinam RP, DeQuardo JR, Nalepa R, Tandon R (2000). Superior temporal gyrus in schizophrenia: a volumetric magnetic resonance imaging study. Schizophr Res 41:303–12.

Sanfilipo M, Lafargue T, Arena L, Rusinek H, Kushner K, Lautin A (2000). Fine volumetric analysis of the cerebral ventricular system in schizophrenia: further evidence for multifocal mild to moderate enlargement. Schizophr Bull 26:201–16.

Shenton ME, Dickey CC, Frumin M, McCarley RW (2001). A review of MRI findings in schizophrenia. Schizophr Res 49:1–52.

Smith RC, Calderon M, Ravichandran GK, Largen J, Vroulis G, Shvartsburd A (1984). Nuclear magnetic reso-nance in schizophrenia: a preliminary study. Psychiatry Res 12: 137–47.

Sowell ER, Levitt J, Thompson PM, Holmes CJ, Blanton RE, Kornsand DS (2000). Brain abnormalities in early-onset schizophrenia spectrum disorder observed with statistical parametric mapping of structural magnetic resonance images. Am J Psychiatry 157:1475–84.

Sowell ER, Peterson BS, Thompson PM, Welcome SE, Henkenius AL (2003). Mapping cortical change across the human life span. Nat Neurosci 6:309–15.

Spitz H, Sadock BJ (1973). Small interactional groups in the psychiatric training of graduate nursing students. J Nurs Educ 12:6–13.

Thompson PM, Vidal C, Giedd JN, Gochman P, Blumenthal J, Nicolson R (2001). Mapping adolescent brain change reveals dynamic wave of accelerated gray matter loss in very early-onset schizophrenia. Proc Natl Acad Sci USA 98:11650–5.

Todtenkopf MS, Vincent SL, Benes FM (2005). A cross-study meta-analysis and three-dimensional comparison of cell counting in the anterior cingulate cortex of schizophrenic and bipolar brain. Schizophr Res 73:79–89.

Vidal CN, Rapoport JL, Hayashi KM, Geaga JA, Sui Y, McLemore LE (2006). Dynamically spreading frontal and cingulate deficits mapped in adolescents with schizophrenia. Arch Gen Psychiatry 63:25–34.

Walterfang M, Wood SJ, Velakoulis D, Pantelis C (2006). Neuropathological, neurogenetic and neuroimaging evidence for white matter pathology in schizophrenia. Neurosci Biobehav Rev 30:918–48.

Weinberger DR, McClure RK (2002). Neurotoxicity, neuroplasticity, and magnetic resonance imaging morphometry: what is happening in the schizophrenic brain? Arch Gen Psychiatry 59:553–8.

Wright IC, Rabe-Hesketh S, Woodruff PW, David AS, Murray RM, Bullmore ET (2000). Meta-analysis of regional brain volumes in schizophrenia. Am J Psychiatry 157:16–25.

Image Anal Stereol 2013;32:155-165 doi:10.5566/ias.v32.p155-165
Original Research Paper

MULTICLASS PATTERN RECOGNITION OF THE GLEASON SCORE OF PROSTATIC CARCINOMAS USING METHODS OF SPATIAL STATISTICS

TORSTEN MATTFELDT✉,[1], PAUL GRAHOVAC[1] AND SEBASTIAN LÜCK[2]

[1]Institute of Pathology, University of Ulm, 89081 Ulm, Germany; [2]Institute of Stochastics, University of Ulm, 89081 Ulm, Germany
e-mail: torsten.mattfeldt@uni-ulm.de, grahovac.pur@googlemail.com, seblueck@gmx.net
(Received October 10, 2013; revised November 25, 2013; accepted November 26, 2013)

ABSTRACT

The Gleason score of a prostatic carcinoma is generally considered as one of the most important prognostic parameters of this tumour type. In the present study, it was attempted to study the relation between the Gleason score and objective data of spatial statistics, and to predict this score from such data. For this purpose, 25 T1 incidental prostatic carcinomas, 50 pT2N0, and 28 pT3N0 prostatic adenocarcinomas were characterized by a histological texture analysis based on principles of spatial statistics. On sectional images, progression from low grade to high grade prostatic cancer in terms of the Gleason score is correlated with complex changes of the epithelial cells and their lumina with respect to their area, boundary length and Euler number per unit area. The central finding was a highly significant negative correlation between the Gleason score and the Euler number of the epithelial cell phase per unit area. The Gleason score of all individual cases was predicted from the spatial statistical variables by multivariate linear regression. This approach means to perform a multiclass pattern recognition, as opposed to the usual problem of binary pattern recognition. A prediction was considered as acceptable when its deviation from the human classification was no more than 1 point. This was achieved in 79 of these 103 cases when only the Euler number density was used as predictor variable. The accuracy could be risen slightly to 84 of the 103 cases, when 7 input variables were used for prediction of the Gleason score, which means an accuracy of 81.5%.

Keywords: classification, pattern recognition, prostate cancer, regression, spatial statistics.

INTRODUCTION

Staging and grading are of central importance for treatment decisions and prognostication of prostate cancer. For staging, the TNM classification of the UICC is the established standard (Sobin *et al.*, 2009). As grading procedure, the Gleason grading system is usually recommended (see, *e.g.*, Murphy *et al.*, 1994; Amin *et al.*, 2004; Eble et al., 2004). According to this system, the histological textures within the tumour are evaluated at low magnification and graded in values from 1–5. The Gleason score is obtained by summing up the grades of the two most dominant textures (Gleason, 1966; 1992; Amin *et al.*, 2004; Eble *et al.*, 2004). Hence a Gleason score is an integer number in the interval $[2,10]$. While staging of prostatic carcinomas according to the TNM-scheme is usually considered as highly reproducible, there remains admittedly a subjective element in Gleason grading. This may lead to intra-observer and inter-observer variability, when the same cases are examined twice by the same observer or by two different observers, respectively.

In previous investigations, it has been shown that the texture of prostatic tissue, as seen at low magnification, may be characterized quantitatively in terms of spatial statistics and stereology (Mattfeldt *et al.*, 1999; 2000; 2003; Mattfeldt, 2003). Basically, prostatic carcinoma tissue may be subdivided into three phases, namely the epithelial cells (the tumour cells), the lumina, and the stroma, which together account for 100% of the tumour tissue. Applying established methods of spatial statistics to digitized binary images, it is possible to characterize these phases quantitatively in terms of area, boundary length and Euler number per unit tissue area (see, *e.g.*, Ohser and Mücklich, 2000). In particular, the Euler number appears highly attractive for a quantitative characterization of prostatic carcinomas. The Euler number χ of a set of geometrical objects is the number of separate objects minus the number of holes in them (Fig. 1). Hence the Euler number should be directly linked to fundamental pathological tumor properties such as solid architecture where ideally $\chi > 0$ (epithelial blocks without holes), tubular architecture where $\chi \approx 0$ (approximately one hole per block), and cribriform architecture where ideally $\chi < 0$ (many holes inside a block; Mattfeldt *et al.*, 2007b).

A look at the well-known schematic images of the Gleason grades shows that grades 1–2 have a tubular differentiation, grade 3 consists of a mixture of tubular and cribriform (sieve-like) structures, grade

4 is predominantly cribriform, and grade 5 contains cribriform and solid patterns (Gleason, 1966; 1992; Amin *et al.*, 2004; Eble *et al.*, 2004). Hence, it seems plausible to characterize the texture of prostatic carcinomas in terms of the Euler number of the phase of the epithelial cells per unit area, in addition to other model parameters, in relation to the Gleason score. In this investigation, we wanted to find answers to the following questions: (i) Which objective quantitative textural changes occur in prostatic tissue with progression from low to high Gleason scores? (ii) To which extent is it possible to predict the Gleason score from such data in individual cases? In an earlier paper with less cases, we had tried to predict the stage of such tumours in a *binary* manner (pT2 vs. pT3) from similar data (Mattfeldt *et al.*, 2003). In the present paper, we deal with the prediction of the Gleason score, which means *multiclass* pattern recognition from spatial data, which is new as far as we can determine. Moreover, the number of cases has been increased, and tumours of stage T1 have been newly included.

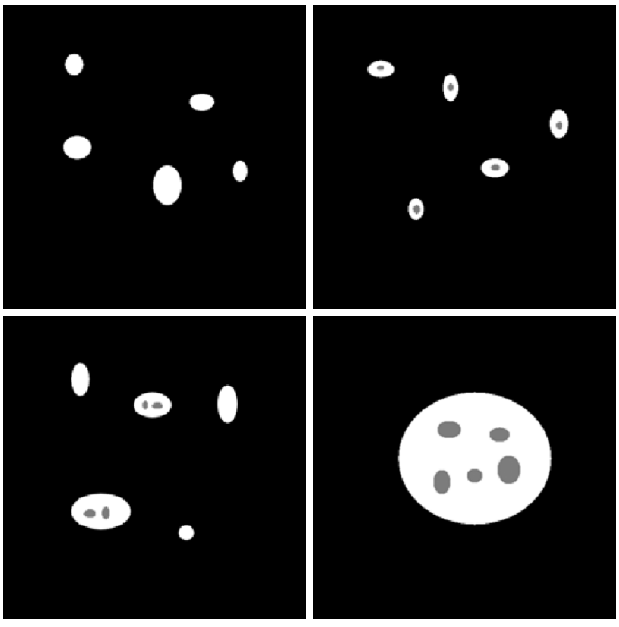

Fig. 1. *Schematic illustration of the Euler number for a triphasic structure with the phases: epithelial cells (white), lumen (grey) and stroma (black). The Euler number χ ist the number of individual structures minus the number of holes in them. For the white phase, we have in the upper left panel $\chi = 5$, in the upper right panel $\chi = 5-5 = 0$, in the lower left panel $\chi = 5-4 = 1$, and in the lower right panel $\chi = 1-5 = -4$.*

MATERIAL AND METHODS

PATIENTS

The investigations were performed on prostatic carcinoma specimens of 103 patients from 3 groups. A first group (the T1-group) consisted of 25 cases of incidental prostatic carcinoma, diagnosed from transurethral resection material or from surgical resection specimens (adenomectomies) that had been removed because of a diagnosis of benign prostatic hyperplasia; these had been classified as T1a or T1b, respectively. A second group (the pT2-group) consisted of 50 primary prostatic adenocarcinomas with TNM classification pT2N0. A third group (the pT3-group) consisted of 28 prostatic adenocarcinomas classified as pT3N0. The primary tumor specimens in the pT2- and pT3-groups were radical prostatectomy specimens. In fact, the cases of the pT2- and pT3-groups had also been used in our previous study on the prediction of prostatic carcinoma stage on the basis of stereological data and CGH findings (Mattfeldt *et al.*, 2003). The tumor-bearing slides of all prostatectomy specimens had been evaluated by the first author with respect to the Gleason score prior to the investigation. The mean Gleason score in the T1 group was 4.16 (SD: 1.30), in the pT2 group it was 6.18 (SD: 0.92), and in the pT3 group it was 7.11 (SD: 0.99).

SPATIAL STATISTICS

In diagnostic histopathology, tissue sections are studied under light microscopical view. If it comes to quantitation, rectangular or quadratic windows are usually superimposed onto the sections. In the first instance, one is hence faced with planar textures. These may be interpreted as realizations of planar random closed sets (RACS) restricted to rectangular observation windows. As numerical descriptors for this type of data we will estimate

- A_A, the mean area of the interesting phase per unit reference area (area fraction),
- B_A, the mean boundary length of the interesting phase per unit reference area, and
- χ_A, the mean Euler number of the interesting phase per unit reference area.

These three model parameters are also denoted as the *specific intrinsic volumes* of the RACS in the plane. In order for the specific intrinsic volumes to be well-defined, the RACS needs to satisfy certain conditions. Hence, referring to Schneider and Weil (2000), Theorem 5.1.3, for our investigations we assume that our data sets may be viewed as realizations of RACSs with the following properties:

- The RACSs are stationary, *i.e.*, their distribution is invariant w.r.t. translations of the origin.
- With probability 1, the RACSs have realizations in the extended convex ring, *i.e.*, the restrictions of the RACSs to any compact and convex observation window K can be decomposed into finitely many compact and convex subsets.
- If $N([0,1]^2)$ denotes the (random) minimum number of sets in such a decomposition w.r.t. the unit cube, $2^{N([0,1]^2)}$ has finite expectation.

Since we are working with bounded pixel images, the degree to which these assumptions reflect the true nature of the tissue must remain unclear. However, the quite central stationarity assumption seems to be realistic for the inner parts of the tissues captured by the observation windows.

For the purpose of this investigation, paraffin sections of a nominal thickness of 5 µm stained with Haematoxylin-Eosin were used. From these sections, visual fields containing tumour tissue were selected according to technical quality criteria at an objective magnification of 10 ×. In practice, all sections were looked through, and the a fixed number of the first visual fields with clearly discernible tumour tissue and without artifacts were used for the study. In the T1 group 5 fields were studied, because the amount of tumour tissue was often rather sparse in these cases where only parts of the prostate glands had been removed, whereas 10 fields were examined in the pT2 and pT3 groups, where complete specimens of the complete prostate gland were available. The images had the size 510×510 pixels (*i.e.*, 512×512 pixels including a non-informative black border of 1 pixel width on each edge). They were acquired with a CCD camera connected to a Zeiss light microscope and transferred to the image analysis system Kontron IBAS 2000, where they were interactively segmented into the three phases: epithelial cells (tumour cells), lumina, and stroma (Figs. 2,3). Interactive segmentation consisted in tracing the profiles of the lumina and epithelial blocks with the electronic cursor on the digitizing tablet of the aforementioned Kontron system under visual control on a monitor; the remainder was considered as the stromal component. As the contrast between these components is very high (see Figs. 2,3), the risk of subjectivity is very low according to our experience from previous studies (Mattfeldt *et al.*, 1999, 2001, 2003).

The segmentation was performed by a technician, who was not provided with information on the Gleason score. The segmented images were transferred to a PC and converted to binary images containing i. only the luminal phase and its complement, ii. only the epithelial cell phase and its complement, and iii. only the stromal phase and its complement. Finally, the resulting binary images were evaluated using routines of the software package Geostoch, a Java based open library system (Mayer *et al.*, 2004). In this package, the routine 'Measure2D' was used, which is based on established algorithms for the estimation of specific intrinsic volumes from digitized binary images in 2D (see Ohser and Mücklich, 2000, section 4.2, pp. 124–133). Thus, one obtains estimates of A_A, B_A and χ_A for the aforementioned phases i.–iii. of every image, *i.e.*, 9 specific intrinsic volumes are estimated per image in the first instance. To characterize the individual tumours, arithmetic mean values were computed between these estimates for the 5–10 images per case. The final magnification corresponded to a width of 0.4 mm of the quadratic visual field at the scale of the tissue.

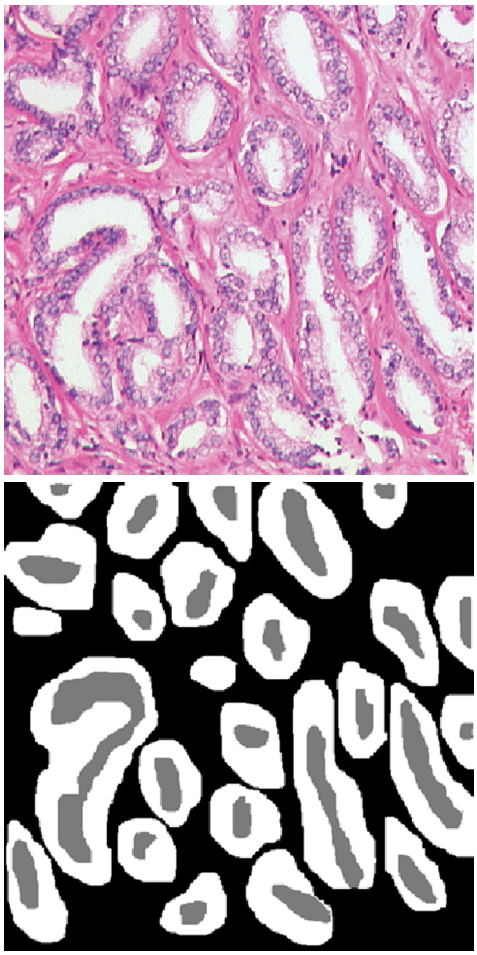

Fig. 2. *Upper panel: visual field from a prostatic adenocarcinoma with tubular differentiation (primary and secondary Gleason grade 3). Haematoxylin-Eosin stain. Its segmentation leads to the lower panel, which contains the three phases: white – epithelial cells, gray – lumen, black – stroma. Gleason score 3+3=6.*

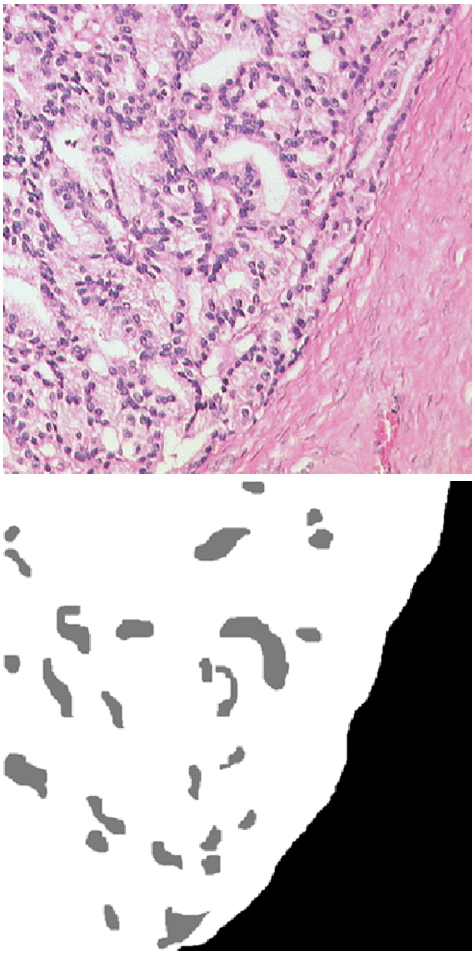

Fig. 3. *Upper panel: visual field from a prostatic adenocarcinoma with cribriform differentiation (primary and secondary Gleason grade 4). Lower panel: the same image after segmentation. Haematoxylin-Eosin stain. Gleason score 4+4=8.*

STATISTICAL METHODS

VARIABLE SELECTION

An attempt was made to find the best combination of input variables for the classification (pattern recognition) of the cases with respect to the Gleason score (see below). To this aim, we applied *multivariate linear regression* of 9 influence variables (the 3 estimates $\hat{A}_A, \hat{B}_A$ and $\hat{\chi}_A$ of the 3 main phases, *i.e.*, epithelial cells, lumen, and stroma) on the Gleason score as the dependent variable. In this case, we suppose that the output variable is a linear combination of the influence variables plus a random error term. Using this approach, the Gleason score is considered as a real variable, although in fact it takes only integer values, for the sake of simplification. To implement this approach, the 'reg' procedure of the program package SAS was used with the 'maxr' option. In this mode the program performs multivariate linear regressions of all the 9 influence variables on the Gleason score and tries to find the best combination for each prescribed number of variables (1–9).

PREDICTION (MULTICLASS PATTERN RECOGNITION)

It was attempted to predict the Gleason score from quantitative image characteristics of individual cases by computer. This approach may be considered as an example of *statistical learning* with a supervised learning rule. The computer learns by training from preclassified cases, from which the set of input variables and the output variable (the Gleason score) are known. As input data, those combinations of the variables were selected that provided the best linear regression models for fixed numbers of input variables from 1 to 9. The output variable is the Gleason score, *i.e.*, an integer number in the interval [2,10]. Hence, we deal with a problem of *multiclass pattern recognition.* The values of the independent variables were inserted into the fitted regression equation. The value obtained by rounding this result to the next integer was then taken as the estimate of the Gleason score of the test case.

CROSS-VALIDATION

In our retrospective data set, the accuracy of prediction of the output data from the input data in the test phase was examined by *cross-validation.* This concept means that the total set of n cases is partitioned into a subgroup of $n-k$ cases (the training cases) and another subgroup which consists of the k remaining cases (the test cases). In the training phase, the algorithm 'learns' to estimate the output variable from the input variables within the training group. In the test phase thereafter, the output variable of the test cases is estimated from the input variables of the test cases making use of the information learnt previously from the training group. This strategy simulates a confrontation of the algorithm with a new case, and by this manner one tests its ability to generalize. When the number of cases is large, it is possible to use, *e.g.*, 25–33% of the cases as test cases. If the number of cases is relatively small (*e.g.*, $n \approx 100$), it is often recommended to choose $k = 1$, *i.e.*, to apply the *leave-one-out principle* (synonyms: jackknife, round-robin) (Tourassi and Floyd, 1997; Vapnik, 1998). The latter approach was also used in the present study. The prediction is repeated cyclically for every patient as test case with the complementary set of cases serving as its training group.

Table 1. *Group comparisons.*

Group		1 (GS 2–4)		2 (GS 5–7)		3 (GS 8–10)	
Number of cases		13		79		11	
Variable		Mean	SD	Mean	SD	Mean	SD
A_A(epi)		0.3452	0.0921	0.4282	0.0756	0.5405	0.1161
A_A(lumen)		0.0876	0.0485	0.1132	0.0443	0.0917	0.0638
A_A(stroma)		0.5670	0.1130	0.4584	0.0902	0.3676	0.1413
B_A(epi)	[mm/mm^2]	36.9211	7.9281	48.8251	7.4582	39.9074	10.0248
B_A(lumen)	[mm/mm^2]	11.4390	2.5549	17.4614	4.3937	18.1943	8.4128
B_A(stroma)	[mm/mm^2]	25.4924	6.4175	31.3801	5.3632	21.7252	11.0343
χ_A(epi)	[mm^{-2}]	−13.7379	27.5399	−77.8718	61.9519	−186.0369	140.6322
χ_A(lumen)	[mm^{-2}]	109.0144	41.1674	167.5646	52.3744	221.7329	117.2564
χ_A(stroma)	[mm^{-2}]	−109.4831	42.0575	−128.9811	44.2810	−69.7869	94.8673

RESULTS

GROUP COMPARISONS

The cases were sorted into three groups with respect to the Gleason score: group I with low scores (2–4), group II with intermediate scores (5–7), and group III with high scores (8–10). The results are shown in Table I. The group mean values were tested for significant differences by pairwise t-tests between group I and II, and between group II and III.

RESULTS FOR THE EPITHELIAL CELL PHASE

The area fraction of epithelial cells rose highly significantly with increasing Gleason score ($p < 0.0001$) (Fig. 4, upper panel). The boundary length density of the epithelial cells rose significantly from group I to group II ($p < 0.0001$), but fell significantly from group II to group III ($p < 0.001$) (Fig. 4, middle panel). The Euler number density of the epithelial phase attained a slightly negative value already in group I, and declined to more and more negative values in groups II and III ($p < 0.0001$) (Fig. 4, lower panel).

RESULTS FOR THE LUMINAL PHASE

There was an increase of the luminal boundary length density in cases of Group II in comparison to group I ($p < 0.001$) (Fig. 5, upper panel). The Euler number density of the lumina remained positive throughout all groups. It rose significantly from group I to group II ($p < 0.001$) and from group II to group III ($p < 0.001$) (Fig. 5, lower panel).

RESULTS FOR THE STROMAL PHASE

The area fraction of the stroma declined highly significantly through all groups with increasing Gleason scores ($p < 0.01$). The boundary length density of the stromal phase increased highly significantly from group 1 to group 2 ($p < 0.001$) and thereafter decreased significantly from group 2 to group 3 ($p < 0.001$). The Euler number density of the stromal phase assumed strongly negative values in all 3 groups. It moved towards less negative values from group II to group III ($p < 0.001$), which reflects a decrease of the number of epithelial units (union of epithelial cells and lumen, *i.e.*, 'holes' from the viewpoint of the stroma) inside the stroma (Fig. 6).

CORRELATION ANALYSIS

Linear correlation analysis of the data revealed a highly significant positive correlation of the Gleason score with the area fraction of the epithelial phase ($r = 0.4380, p < 0.0001$). The Gleason score was also correlated positively with the boundary length density of the luminal phase ($r = 0.3798, p < 0.0001$). There were no significant correlations between the Gleason score and the area fraction of the luminal phase and with the boundary length densities of the epithelial cell phase, respectively.

A highly significant negative correlation was found between the Gleason score and the Euler number density of the epithelial cell phase per unit area ($r = -0.5284, p < 0.0001$). There was also a significant positive correlation of the Gleason score with the Euler number density of the lumina ($r = 0.4390, p < 0.0001$).

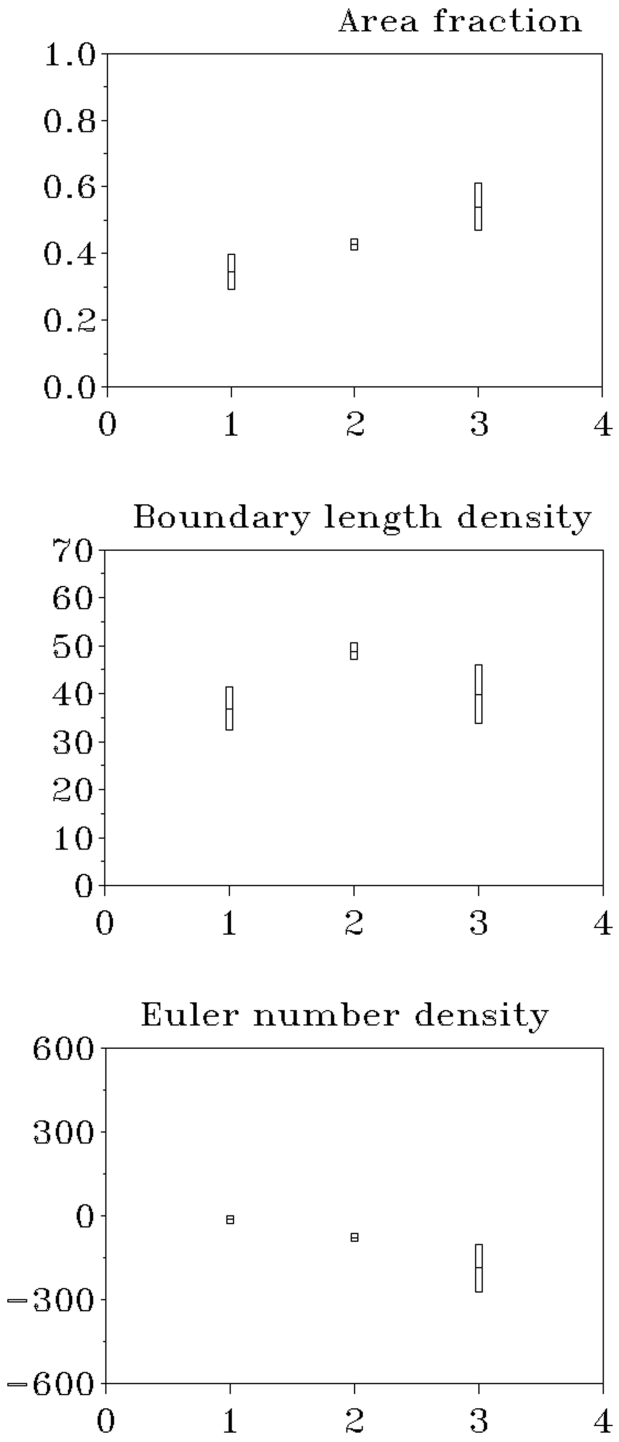

Fig. 4. *Results for the epithelial cell phase. Abscissa value 1: Gleason score 2–4, 2: Gleason score 5–7, 3: Gleason score 8–10. Indicated are group mean values and bounds of 95% confidence intervals. Upper panel: Area fraction of epithelial cells in the three groups. Middle panel: Boundary length of epithelial cells per unit area in the same groups. Lower panel: Euler number of epithelial cells per unit area in the same groups. This parameter shows a highly significant decrease with increasing Gleason score.*

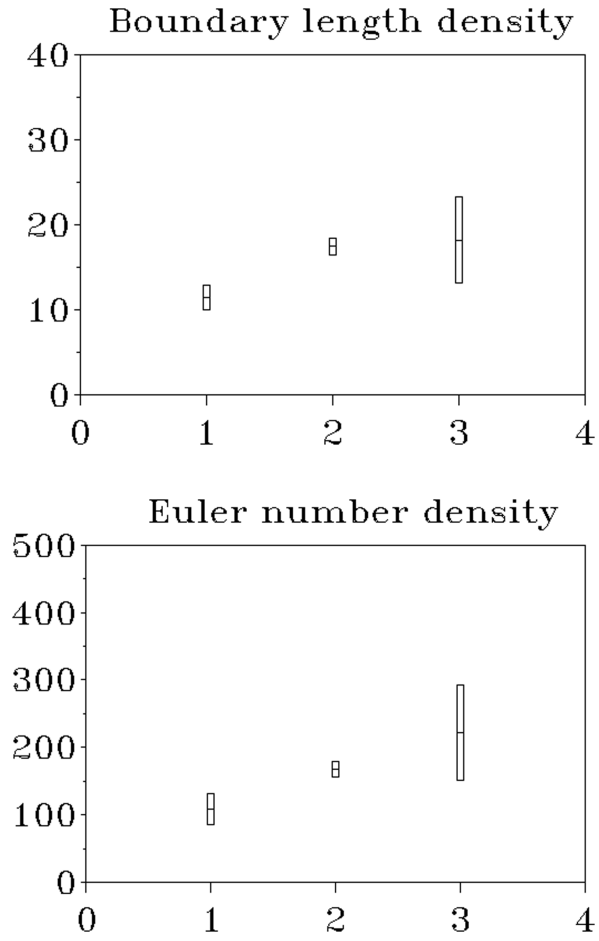

Fig. 5. *Results for the luminal phase. Upper panel: Boundary length of lumina per unit area in the same groups. The increase from group 1 to group 2 is significant. Lower panel: Euler number of lumina per unit area in the same three groups. This parameter shows a significant increase with increasing Gleason scores.*

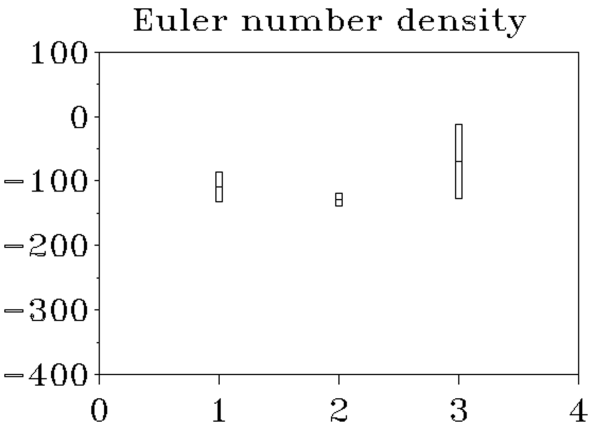

Fig. 6. *Results for the stromal phase. Euler number of stroma per unit area in the same three groups.*

PREDICTION

In our cross-validation study with the leave-one-out scheme, the Gleason score of each individual case was predicted by linear regression and rounding to the next integer, as outlined above, with cyclically training on 102 cases and testing on 1 case. Usually, in studies on observer variability of the Gleason score, a classification is considered as acceptable, when two judgments of a case differ by no more than 1 point (see, *e.g.*, Bostwick, 1994). Using this criterium, we found that the Gleason score of 79 of the 103 cases (*i.e.*, 76.6%) could already be predicted sufficiently on the basis of only one parameter: the Euler number density χ_A of the epithelial cell phase. The highest accuracy of prediction was found when the following 7 variables were included into the regression model: Euler number density, area fraction and boundary length density of the epithelial cell phase; Euler number density and boundary length density of the luminal phase; Euler number density and boundary length density of the stroma. When the aforementioned criterium of sufficient accuracy at a discrepancy ≤ 1 was adopted, 84/103 predictions (81.5%) were considered as acceptable. The correlation coefficient between the predicted Gleason score and the preclassified Gleason score was $r = 0.6059$ ($p < 0.0001$) in the best model.

DISCUSSION

TISSUE CHANGES WITH INCREASING GLEASON SCORE

Let us first consider the changes of the elementary parameters: area fraction and boundary length density. The area fraction of the epithelial cells rose with increasing Gleason score. This is very plausible when one considers the large epithelial areas devoid of stroma in high grade prostatic carcinomas. The area fraction of the luminal phase remained nearly constant with increasing Gleason scores. This finding was, however, accompanied by a rise of the boundary length of the luminal phase per unit tissue area. If the boundary length of the lumina rises despite an unchanged area fraction, this means that a geometrical change must have occurred by which boundary length has been gained. It means that the boundary-to-area ratio of the luminal phase must have increased. This may occur if either the luminal units, maintaining their shape, become smaller and increase in number, or if the luminal units change to more elongated or wrinkled shapes without increasing their number. Clearly, also a combination of mechanisms can account for the phenomenon. All three mechanisms augment boundary length but keep the area fraction constant. That the first effect is stronger is suggested by the finding that the Euler number of the luminal phase per unit area increased with the Gleason score.

The geometrical meaning of A_A and B_A is intuitively obvious. The Euler number density χ_A is more complex. It is the number of units minus the number of holes in them per unit area. The main finding of this study was a rather strong negative correlation $(r = -0.5284, p < 0.0001)$ between the Euler number density of the epithelial cell phase and the Gleason score. The epithelial cells form a complex phase, which essentially has two disjoint boundaries: an outer boundary, directed towards the stroma, and an inner boundary, directed towards the lumina. The Euler number density of the epithelial cell phase is influenced by both components. First, the data show that an increase to large Gleason scores led to a decrease of the Euler number density of the epithelial blocks (including cells and lumina). This change is also reflected in the transition of the Euler number density of the stroma to less negative values in the step from intermediate to very high Gleason scores. Hence, we have a reduction of the Euler number density 'from outwards'. Second, there was a strong positive correlation of the Gleason score with the Euler number density of the lumina. Each newly formed lumen reduces the Euler number of the epithelial cell phase by 1. Hence, the increase of the Euler number density of the lumina led to a further decrease of the Euler number density of the epithelial phase 'from inwards'. To sum up, the strong negative correlation of χ_A of the epithelial phase to the Gleason score is due to a decrease of the number of the epithelial tumour tissue units per unit area as a whole, and to the formation of an increasing number of epithelial lumina inside them.

The reader will have noted that a highly significant negative correlation between the Gleason score and the Euler number of the epithelial phase per area could be shown, but nevertheless the absolute value of the correlation coefficient was not very high ($r = -0.5284$). Various causes can be discussed to account for this finding. On one hand, a sampling error must be considered: for statistical learning, 5–10 visual fields were selected, whereas the human decision on a Gleason score is based on the evaluation of the whole section. Furthermore, one has to account for the inherently subjective nature of Gleason grading. There is another aspect which becomes apparent when one considers the well-known schematic diagrams of the Gleason grades 1–5. In grade 1–4 tumours, a gradual transition occurs from purely tubular to more and more cribriform structures, which leads to an expected transition from positive to negative Euler

numbers of the epithelial phase per area, as outlined above. Gleason grade 5 patterns are characterized by the development of solid parts, *i.e.*, unstructured epithelial blocks without lumina at all, in addition to the cribriform component which further persists. Such solid structures will tend to increase the Euler number per area a little. This means that, even under ideal conditions, if no sampling error occurs and subjective errors are kept to a minimum, there will be no absolutely linear relation between the Euler number of the epithelial phase per area and the Gleason score any more, when grade 5 patterns are present. Fortunately, this effect is probably not very relevant in reality due to the following considerations. A grade 5 pattern usually occurs in a case with Gleason score 9 or 10. If the Gleason score is 9, this means that grades 4 and 5 dominate, hence a strong cribriform component is still present due to the contribution of grade 4. Even in cases with Gleason score 10, the cribriform variety is rarely totally lost, as the original drawing of Gleason shows (Gleason, 1966; 1992). Moreover, cases with Gleason scores ≥ 9 are generally rare; in our unselected case series, there were only 4 cases with Gleason score 9 (3.9%), and there was no case with Gleason score 10. These data are in accordance with larger series of prostatectomy specimens, where only 2.8% and 0.05% of cases were found with Gleason scores 9 and 10, respectively (Amin *et al.*, 2004). These facts imply that in general, the negative correlation of the Gleason score to the Euler number of the epithelial cell phase per area should hold in good approximation for the whole spectrum of cases.

PREDICTION

A major result of the present study was the finding that in 84/103 cases (81.5%), the Gleason score of a prostatic carcinoma could be successfully predicted from a set of 7 variables of spatial statistics. The criterium for success was that machine prediction and human classification differed by no more than 1 point. Using the aforementioned 7 variables for prediction, only 19/103 cases were insufficiently predicted. It was looked up whether they were systematically undergraded or overgraded. Overgrading was found in 9, and undergrading was found in 10 of these 19 cases. We conclude that the statistical learning method leads neither to a systematic overgrading nor to a systematic undergrading.

Overfitting is a well-known trap in pattern recognition studies. It is likely to occur if too many input variables are used, which makes the model too complex. In this case, one may obtain good results in the training phase, but the system is characteristically unable to generalize to new cases. Here a cross-validation step was performed to avoid this pitfall. Slight overfitting was seen to emerge when the number of input variables was increased from 1 to 2, where the accuracy of prediction sank slightly despite using additional input information: with 2 input variables, the number of sufficiently classified variables decreased from 79 to 76; a similar decrase eas found when the number of input variables was increased from 7 to 8, *i.e.*, a decrease from 84 to 81 acceptably classified cases.

We would like to stress that the type of cross-validation that we used in this investigation – the leave-one-out approach – seems particularly suitable for applications in histopathology. It simulates the situation that an observer has gained experience in a certain number of cases, and on the basis of this learning process he is confronted with a single new case he has to classify. This way of learning is quite analogous to histopathological diagnostics, where the pathologist learns to generalize from multiple similar cases to a new case. In fact, it has been advocated to train Gleason grading by studying preclassified cases, published, *e.g.*, in textbooks (Amin et al., 2004) and on the internet (see http://217.8.156.155/norcyt/prostata/PROST.htm).

With regards to a potential application in practice, our method using spatial statistics applied to interactively segmented images is clearly too laborious for everyday use. However, it becomes increasingly common to work with *virtual microscopic slides*. These are large image files generated by a computer linked to a conventional light microscope which scans the physical microscopic slide completely and fully automatically. If the epithelial phase could be reproducibly segmented, *e.g.*, by an immunohistochemical stain with an antibody that detects specifically the tumour cells, the whole texture analysis as described here could be performed fully automatically.

METHODOLOGICAL ASPECTS

PREDICTION METHODS

Linear regression methods are clearly not the only way to perform a multiclass pattern recognition of the Gleason score from spatial data. Alternatively, one could try to work with robust nonparametric methods of prediction, which do not presuppose a linear model assumption in the relation between the influence variables and the dependent variable. In fact, such a nonlinear behaviour could be observed, *e.g.*, for the

variable B_A of lumen per tissue, which rose from group I to group II and declined in group III as compared to group II. In this context, *artificial neural networks* appear as an attractive alternative, *e.g.*, multilayer feedforward networks with backpropagation, learning vector quantization (LVQ) or support vector machines (SVM; Kohonen *et al.*, 1996; Burges, 1998; Saunders *et al.*, 1998). Such neural paradigms have been used by our group to predict various properties of prostatic carcinomas from input data sets (Mattfeldt *et al.*, 1999; 2001; 2003). For example, it was tried to predict from a set of input variables whether a prostatic carcinoma was still confined to the prostate (stage pT2), or had already extended beyond the organ (stage $\geq$ pT3; Mattfeldt *et al.*, 2001; 2003). In this case, we are faced with *binary* pattern recognition. The same is true when it is tried to predict a relapse from primary tumour data, see Mattfeldt *et al.*(1999). In another study, it was attempted to predict the Gleason score from spatial data in a binary manner, *e.g.*, Gleason score < 7 versus Gleason score ≥ 7 (Wittke *et al.*, 2007). As far as we could determine, however, *multiclass* prediction of the Gleason score on the basis of spatial statistical data has not been performed before.

It is easily possible to adapt the aforementioned algorithms LVQ and SVM in such a manner that they learn to classify items with an ordinal dependent variable (Kohonen *et al.*, 1996; Burges, 1998; Saunders et al., 1998). For example, this option is provided for support vector machines as the 'multiclass pattern recognition mode'. In further research work, it will be examined whether these paradigms may lead to an increase of the predictive accuracy.

SPATIAL STATISTICS

In the present study, the Gleason scores were characterized in terms of planar spatial statistics by estimating specific intrinsic volumes of tissue phases, which were basically considered as *random closed sets with positive area.* While this is a well established field of spatial statistics, much more work has been done in the field of the statistical analysis and modelling of *spatial point patterns* (see, *e.g.*, Illian *et al.*, 2008). Such an approach is also feasible in the case of prostatic cancer, *e.g.*, by studying the point patterns of the tumour cell nucleus profiles. Such patterns may be characterized nonparametrically in terms of first and second order properties. It is also possible to fit parametric point process models to such patterns, *e.g.*, Gibbs processes (Mattfeldt *et al.*, 2007a; Illian *et al.*, 2008). It must however be kept in mind that the present approach based on volume processes is more natural when it is intended to predict the Gleason score from image data, as this method of grading means to focus entirely on the texture and to disregard all nuclear changes deliberately. Pure point process statistics would imply that an important property — the topology of the epithelial cell phase — is neglected. Nevertheless, point process statistics could bring potentially valuable additional information, which is not reflected by the Gleason score. In this context we mention grading systems for prostate cancer which have been suggested as alternatives to the Gleason grading system, see, *e.g.*, (Mostofi, 1975; Böcking et al., 1982; Bostwick, 1994). In contrast to Gleason grading, findings on changes of the tumour cell nuclei are considered in these systems. Here we have concentrated only on Gleason grading, because it is the standard procedure favoured by most urologists and recommended by a WHO consensus conference since 1993 (Murphy *et al.*, 1994).

STEREOLOGY

Based on the following established estimators from stereology, the measured morphological changes in 2D sections of prostatic tissue may be related to alterations of 3D tumour morphology. One has

$$\hat{V}_V = A_A \tag{1a}$$

$$\hat{S}_V = \frac{4}{\pi} B_A \tag{1b}$$

$$\hat{M}_V = 2\pi\chi_A \tag{1c}$$

where V_V is the volume fraction, S_V is the mean surface area per unit reference volume, and M_V is the curvature density (integral of mean curvature per unit volume of the corresponding 3D RACS, see Weibel, 1980, pp. 84–101, Fig. 3.16); by $\hat{V}_V$, $\hat{S}_V$ and $\hat{M}_V$ we denote the estimators of these quantities. In addition to the assumptions made above, which ensure the intrinsic volumes of RACS to be well-defined, these stereological estimators are only unbiased if the RACS is isotropic (see, *e.g.*, Kiderlen, 2010, p. 37). This appears to be a reasonable assumption for our data. Especially the stereological link (1c) between the mean Euler number χ_A and the curvature density M_V is quite instructive: It allows to interpret decreasing values of χ_A (and thus M_V) as a transformation of the 3D tissue surface, where locally convex parts are reduced in favor of a locally concave geometry, which is, *e.g.*, represented by infoldings and holes.

In terms of automated Gleason grading, the use of stereological formulas as above can obviously not be expected to improve the quality of prediction, since the 3D stereological estimates are related to the measured 2D characteristics by multiplication of constant factors.

Stereology also provides methods for the estimation of 2D intrinsic volumes from micrographs, thus presenting alternatives to the quantitation techniques used in this study (Weibel, 1980, pp. 97–101; Stoyan *et al.*, 1995, eqs. 7.3.8, 7.3.9 and 11.2.5, Fig. 7.2). The stereological methods have been implemented in various software packages for the analysis of digitized images. The non-stereological estimation technique applied in our study is however quite appropriate for a fully automatic machine learning approach to Gleason grading that does not require any user interaction. Thus, once image segmentation of the different tissue phases can be done in an automatic way, the proposed method of algorithmic Gleason grading can be conducted in a highly efficient way.

ACKNOWLEDGMENTS

Thanks are due to Michael Held and Rolf Kunft for technical assistance.

REFERENCES

Amin MB, Grignon DJ, Humphrey PA, Srigley JR (2004). Gleason grading of prostatic cancer. A contemporary approach. Philadelphia: Willincott.

Böcking A, Kiehn J, Heinzel-Wach M (1982). Combined histologic grading of prostatic carcinoma. Cancer 50:288–94.

Bostwick DG (1994). Grading prostate cancer. Am J Clin Pathol 102(Suppl 1):38–56.

Burges JC (1998). A tutorial on support vector machines for pattern recognition. Data Mining Knowl Discov 2:121–67.

Eble JN, Sauter G, Epstein JI, Sesterhenn IA (2004). Pathology and genetics of tumours of the urinary system and male genital organs. Lyon: IARC Press.

Gleason DF (1966). Classification of prostatic carcinoma. Cancer Chemother Rep 50:125–8. .

Gleason DF (1992). Histologic grading of prostate cancer: a perspective. Hum Pathol 23:273–9.

Berner A, Busch C, Halvorsen OJ, Haugen OA, Scott H, Sund S, Svindland A: Web-training set for Gleason grading. The Norwegian study group for Prostate Cancer (NUCG).

Illian J, Penttinen A, Stoyan H, Stoyan D (2008). Statistical analysis and modelling of spatial point patterns. Chichester: Wiley.

Kiderlen M (2010). Introduction into integral geometry and stereology. In: Spodarev E, Ed. Stochastic geometry, spatial statistics and random fields. Lect Notes Math 2068:21–48.

Kohonen T, Hynninen J, Kangas J, Laaksonen J, Torkkola K (1996). LVQ_PAK: The learning vector quantization program package. Technical Report A30, Helsinki University of Technology, Laboratory of Computer and Information Science, Otaniemi, Finland.

Mattfeldt T (2003). Classification of binary spatial textures using stochastic geometry, nonlinear deterministic analysis and artificial neural networks. Int J Pattern Recogn 17:275–300.

Mattfeldt T, Kestler HA, Hautmann R, Gottfried HW (1999). Prediction of prostatic cancer progression after radical prostatectomy using artificial neural networks: a feasibility study. BJU Int 84:316–23.

Mattfeldt T, Gottfried H-W, Schmidt V, Kestler HA (2000). Classification of spatial textures in benign and cancerous glandular tissues by stereology and stochastic geometry using artificial neural networks. J Microsc 198:143–58.

Mattfeldt T, Kestler HA, Hautmann R, Gottfried H-W (2001). Systematic biopsy-based staging of prostatic carcinoma using artificial neural networks. Eur Urol 39:530–7.

Mattfeldt T, Gottfried H-W, Wolter H, Schmidt V, Kestler HA, Mayer J (2003). Classification of prostatic carcinoma with artificial neural networks using comparative genomic hybridization and quantitative stereological data. Pathol Res Pract 199:773–84.

Mattfeldt T, Eckel S, Fleischer F, Schmidt V (2007a). Statistical modelling of the geometry of planar sections of prostatic capillaries on the basis of stationary Strauss hard-core processes. J Microsc 228:272–81.

Mattfeldt T, Meschenmoser D, Pantle U, Schmidt V (2007b). Characterization of mammary gland tissue using joint estimators of Minkowski functionals. Image Anal Stereol 26:13–22.

Mayer J, Schmidt V, Schweiggert F (2004). A unified simulation framework for spatial stochastic models. Simul Model Pract Th 12:307–26.

Mostofi FK (1975). Grading of prostatic carcinoma. Cancer Chemoth Rep 59(I):111–7. .

Murphy GP, Busch C, Abrahamsson PA, Epstein JI, McNeal JE, Miller GJ, Mostofi FK, Nagle RB, Nordling S, Parkinson C (1994) . Histopathology of localized prostate cancer. Consensus conference on diagnosis and prognostic parameters in localized prostate cancer. Stockholm, Sweden, May 12-13, 1993. Scand J Urol Nephrol Suppl 162:7–42. .

Ohser J, Mücklich F (2000). Statistical Analysis of Microstructures in Materials Science. Chichester: Wiley.

Saunders R, Stitson MO, Weston J, Bottou L, Schölkopf B, Smola A (1998). Support vector machine reference

manual. Technical Report. Royal Holloway, University of London.

Schneider R, Weil W (2000). Stochastische Geometrie. Stuttgart: Teubner.

Sobin LH, Gospodarowicz MK, Wittekind C, Eds. (2009). TNM classification of malignant tumours. Wiley: New York.

Stoyan D, Kendall WS, Mecke J (1995). Stochastic Geometry and Its Applications, 2nd Ed. Wiley: Chichester.

Tourassi GD, Floyd CE (1997). The effect of data sampling on the performance evaluation of artificial neural networks in medical diagnosis. Med Decis Making 17:186–92. .

Vapnik VN (1998). Statistical Learning Theory. Wiley: New York.

Weibel ER (1980). Stereological Methods. II. Theoretical Foundations. London: Academic Press.

Wittke C, Mayer J, Schweiggert F (2007) On the classification of prostate carcinoma with methods from spatial statistics. IEEE Trans Inf Technol Biomed 11:406–14. .

Image Anal Stereol 2013;32:167-174 doi:10.5566/ias.v32.p167-174
Original Research Paper

COLOR SEGMENTATION OF MGG COLORED CYTOLOGICAL IMAGES USING NON LINEAR OPPONENT COLOR SPACES

HÉLÈNE GOUINAUD✉,[1] AND LARA LECLERC[2]

[1]CIS-LGF/CNRS 158 cours Fauriel 42023 Saint-Etienne Cedex 2 France; [2]Université Jean Monnet F-42023 Saint-Etienne France LINA EA 4624
e-mail: gouinaud@emse.fr, lara.leclerc@univ-st-etienne.fr
(Received March 18, 2013; revised August 8, 2013; accepted October 8, 2013)

ABSTRACT

This paper presents a color image segmentation method for the quantification of viable cells from samples obtained after cytocentrifugation process and May Grunwald Giemsa (MGG) coloration and then observed by optical microscopy. The method is based on color multi-thresholding and mathematical morphology processing using color information on human visual system based models such as CIELAB model, LUX (Logarithmic hUe eXtension) model and CoLIP (Color Logarithmic Image Processing) model, a new human color vision based model also presented in this article. The results show that the CoLIP model, developed following each step of the human visual color perception, is particularly well adapted for this type of images.

Keywords: color, cytology, human vision, image analysis, logarithmic image processing, segmentation.

INTRODUCTION

Classic histotechnology methods (*e.g.* cytocentrifugation) are widely used in clinical medicine and biological research (De Brauwer *et al.*, 2000) and lead to cell observations with morphological considerations. An important aspect is based on the cellular viability and morphological features usually highlighted by colorations such as May Grunwald Giemsa (MGG). The quantification of cells and more particularly viable cells is a determinant parameter in cytology preparations. Generally, in histology laboratories, after cell preparation and coloration, a manual determination of the viability percentage is performed by numbering each dead cell which is time-consuming and leads to potential errors. We describe in this work an image processing algorithm dedicated to the cells numeration and classification for applications after cytocentrifugation and MGG staining.

The MGG coloration produces samples with purple colored cell nuclei and blue colored cytoplasm (see Fig. 1 typical MGG images). This coloration allows the human eye to differentiate living cells (circularly shaped and composed of a nucleus and a cytoplasm) and dead cells (composed of a scattered nuclei, usually brighter than living cell nuclei) better than on gray level sample. The color information is then useful to the human eye to cell detection. Usually, cell image extraction algorithms are based on the image segmentation of an achromatic channel, obtained by combination of the color channels. This type of image segmentation gives relatively good results but ignores the chromatic part of information used by the human visual system. In order to improve the segmentation, particularly the particles disconnection, it is necessary to add chromatic information to the achromatic information. Lezoray et al. have been working on such cytological images color segmentation and cells classification methods. Their segmentation methods are based on watershed, clustering, and mathematical morphology (Lezoray *et al.*, 1999; Lezoray, 2003; Lezoray and Lecluse, 2007), and are most of the time based on classical RGB model. In this article we aim at demonstrating that human vision based color opponent models are also of interest with the cells classification and segmentation issue. In the case of MGG image coloration, which is widely used, we show that color opponent models are much more adapted than classical RGB model. Then we describe the segmentation method based on color multi-thresholding, mathematical morphology processing and adapted for color opponent models. We compare results on CIELAB model, which is the most known and used human vision based model, LUX (Logarithmic hUe eXtension) (Lievin and Luthon, 2004) model, and CoLIP (Color Logarihtmic Image Processing) (Gouinaud *et al.*, 2011) model, two human vision based models derived from the LIP (Logarihtmic Image Processing) theory (Jourlin and Pinoli, 1988; 2001) and the visual human color perception.

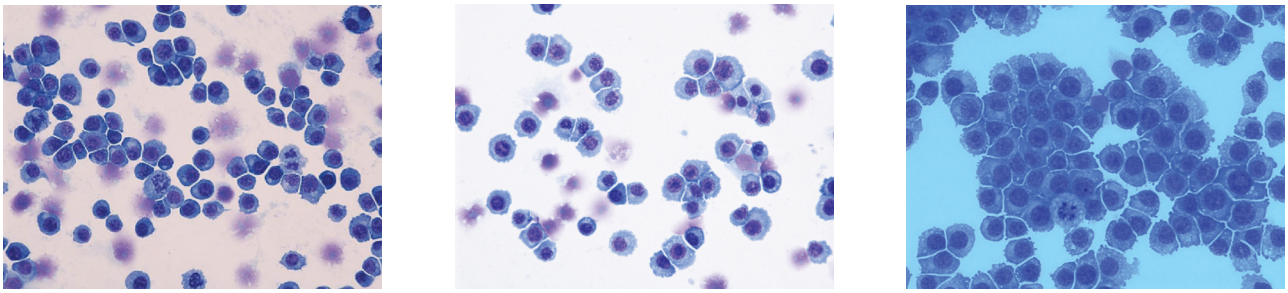

(a) (b) (c)

Fig. 1. *(a), (b), and (c): typical macrophage images obtained with cytocentrifugation process and MGG coloration and then observed on an optical microscope with the 40× objective (Size: 1560 × 1920 pixels).*

MATERIALS AND METHODS

IN VITRO MODEL

Macrophage cell culture

The RAW 264.7 cell line was provided by ATCC Cell Biology Collection (Promochem LGC) and derives from mice peritoneal macrophages transformed by the AMLV virus (Abelson Murine Leukemia Virus). Cells were cultured in DMEM medium (Dulbecco's Modified Eagle's Medium, Gibco) complemented with 10% of fetal calf serum (FCS, Gibco), 1% penicillin-streptomycin (penicillin 10 000 units/ml, streptomycin 10 mg/ml, Sigma) and incubated at 37°C under a 5% carbon dioxide humidified atmosphere.

Cytocentrifugation

The cytocentrifuge is widely used in clinical medicine and biological research to transfer biological cells onto a microscope slide. Cells were grown in 25 cm^2 culture flasks (1 million cells in 4 ml of DMEMc). After proliferation, cells were gently removed with a scraper and centrifuged. The desired concentration of 100 000 cells per slide were then cytocentrifuged for 10 minutes at 600 rpm (Cytospin Shandon) and air dried over night at room temperature.

May Grunwald Giemsa coloration

This staining is dedicated to air dried cytology preparations such as cytocentrifugation and was performed with an inclusion automat (Leica Autostainer XL). The procedure was performed as follows: Fixation in methanol for 15 minutes, staining in May-Grunwald for 5 minutes, staining in Giemsa for 10 minutes. Rinsing in a pH 6.8 buffer, rinsing in a 50/50 buffer/acetone, dehydration in acetone X2 and clearing in xylene X3. This coloration allows the distinction between cell nuclei which appeared violet and cytoplasm which appeared in blue. Such details would not be as precise without any preparation.

Images acquisition

Samples were then observed on an optical microscope (Nikon Eclipse 80i) coupled with a digital sight Nikon camera. Acquisitions were performed using different microscope objectives (10×, 40×, 60× and 100× under oil immersion). For the rest of the study, in order to have reproductive data, only the images acquired with the 40× objective are treated.

Fig. 1 presents typical MGG images acquired following the procedure described in this paragraph. Results of the color segmentation algortithm presented below will be displayed on these example images. Due to the acquisition profile of the microscope, image coloration can be bright or dark, and a blue halo can appear (see Fig. 1c). A white balance algorithm will be added before the color segmentation in order to extract the sample background color and standardize images balance.

COLOR VISION BASED MODELS

Color human perception can be described by two complementary visual theories that model representation and processing of color information along the visual pathway. The trichromacy theory (Young-Helmoltz) states that the retina contains three types of cones, responsible for color vision and sensitive to red, green, and blue wavelength. The opponent process theory (Hering) states that the human visual system interprets information about color in an antagonistic way (Fairchild, 2005). Human vision based color spaces usually follow the two theories, and are divided in three steps which produce three antagonists channels. The first step models the trichromacy, *i.e.*, the light absorption by cones photoreceptors denoted L, M and S according to the wavelengths of their spectral sensitivities peaks (Long, Medium, and Short wavelength, respectively). When converted to an electric signal, the light intensity signal is compressed and psychological studies have

shown that the neural response from a stimulus is close to a logarithmic curve (Fairchild, 2005). This cone compression corresponds to the second steps of human vision based models. The third and last step is the opponent processing of color information that occurs on upper layers of the retina and on the brain, and produces three opposing pairs of processes, one achromatic and two chromatic red-green and yellow-blue channels, which are linear combinations of the cones' neural responses (Fairchild, 2005).

The three color opponent models presented here, the CIELAB model (Fairchild, 2005), the LUX model proposed by Luthon et al. (Lievin and Luthon, 2004; Luthon *et al.*, 2010) and the CoLIP model proposed by Gouinaud et al. (Gouinaud *et al.*, 2011), follow these three fundamental steps.

CIELAB model

The CIELAB color space is a color-opponent space, where the dimension L^* represents the lightness and the dimensions a^* and b^* represent the red-green and yellow-blue color-opponent dimensions, based on nonlinearly compressed CIE XYZ color space coordinates which take into account the illuminant or white point (X_W, Y_W, Z_W) (Fairchild, 2005).

$$\begin{cases} L^* = 116 * f\left(\dfrac{Y}{Y_W}\right) - 16\,, \\ a^* = 500 * \left(f\left(\dfrac{X}{X_W}\right) - f\left(\dfrac{Y}{Y_W}\right)\right), \\ b^* = 200 * \left(f\left(\dfrac{Y}{Y_W}\right) - f\left(\dfrac{Z}{Z_W}\right)\right), \end{cases} \tag{1}$$

where the cone compression f is the following function:

$$f(x) = \begin{cases} \sqrt[3]{x}\,, & \text{if } x > \left(\dfrac{6}{29}\right)^3, \\ \dfrac{1}{3}\left(\dfrac{29}{6}\right)^2 x + \dfrac{4}{29}\,, & \text{if } x \le \left(\dfrac{6}{29}\right)^3. \end{cases} \tag{2}$$

The LUX model

The LUX approach is based on the LIP framework too, and has also been built by the following steps of human color visual perception (Lievin and Luthon, 2004; Luthon *et al.*, 2010). Cone intensities are represented by (R,G,B) channels and then the non-linear response of the retinal stage is modeled by the isomorphism ϕ applied on each chromatic tone channel,

$$\phi(F) = -M_0 \ln\left(\frac{F+1}{M_0}\right). \tag{3}$$

The opponent process is modeled by the (Y,C_r,C_b) color space transformation applied on resulting logarithmic chromatic tones. The (Y,C_r,C_b) color space transformation matrix called P_{LUX} is:

$$P_{LUX} = \begin{pmatrix} 0.3 & 0.6 & 0.1 \\ 0.5 & -0.4 & -0.1 \\ -0.2 & -0.3 & 0.5 \end{pmatrix}. \tag{4}$$

Finally, in applying the inverse isomorphism ϕ^{-1} on logarithmic antagonist channels resulting from the (Y,C_r,C_b) color space transformation, the (L,U,X) channels that represent color in the LUX model can be derived from (R,G,B) intensities as follows:

$$\begin{aligned} L &= (R+1)^{0.3}(G+1)^{0.6}(B+1)^{0.1} - 1\,, \\ U &= \begin{cases} \dfrac{M_0}{2}\left(\dfrac{R+1}{L+1}\right), & \text{if } R \le L\,, \\ M_0 - \dfrac{M_0}{2}\left(\dfrac{L+1}{R+1}\right), & \text{if } R \ge L\,, \end{cases} \\ X &= \begin{cases} \dfrac{M_0}{2}\left(\dfrac{B+1}{L+1}\right), & \text{if } B \le L\,, \\ M_0 - \dfrac{M_0}{2}\left(\dfrac{L+1}{B+1}\right), & \text{if } B \ge L\,. \end{cases} \end{aligned} \tag{5}$$

The CoLIP Model

The CoLIP model is the color extension of the LIP model (Jourlin and Pinoli, 1988; 2001), constructed following each step of the human vision (Gouinaud *et al.*, 2011). In the CoLIP framework, the image has first to be transformed from its original representation space to the cone pigment absorption space (L,M,S). In the case of the (X,Y,Z) space, the linear transformation matrix U from (X,Y,Z) to (L,M,S) is the M_{HPE} matrix (Fairchild, 2005):

$$M_{HPE} = \begin{pmatrix} 0.38971 & 0.68898 & -0.07868 \\ -0.22981 & 1.18340 & 0.04641 \\ 0 & 0 & 1 \end{pmatrix}. \tag{6}$$

As in the LIP framework, color images are represented by color tone vector $\vec{f}(x,y) = (l(x,y), m(x,y), s(x,y))$ defined on a spatial domain $\mathbf{D}$ in $\mathbb{R}^2$ and related to intensity vector $\vec{F} = (L(x,y), M(x,y), S(x,y))$ through the following relation:

$$\vec{f} = \begin{pmatrix} l \\ m \\ s \end{pmatrix} = \begin{pmatrix} M_0\left(1 - \frac{L_t}{L_i}\right) \\ M_0\left(1 - \frac{M_t}{M_i}\right) \\ M_0\left(1 - \frac{S_t}{S_i}\right) \end{pmatrix}, \tag{7}$$

where M_0 is a scaling factor, L_i, M_i and S_i represent incident light, and L_t, M_t and S_t represent transmitted light. The color tone vector is nothing else than

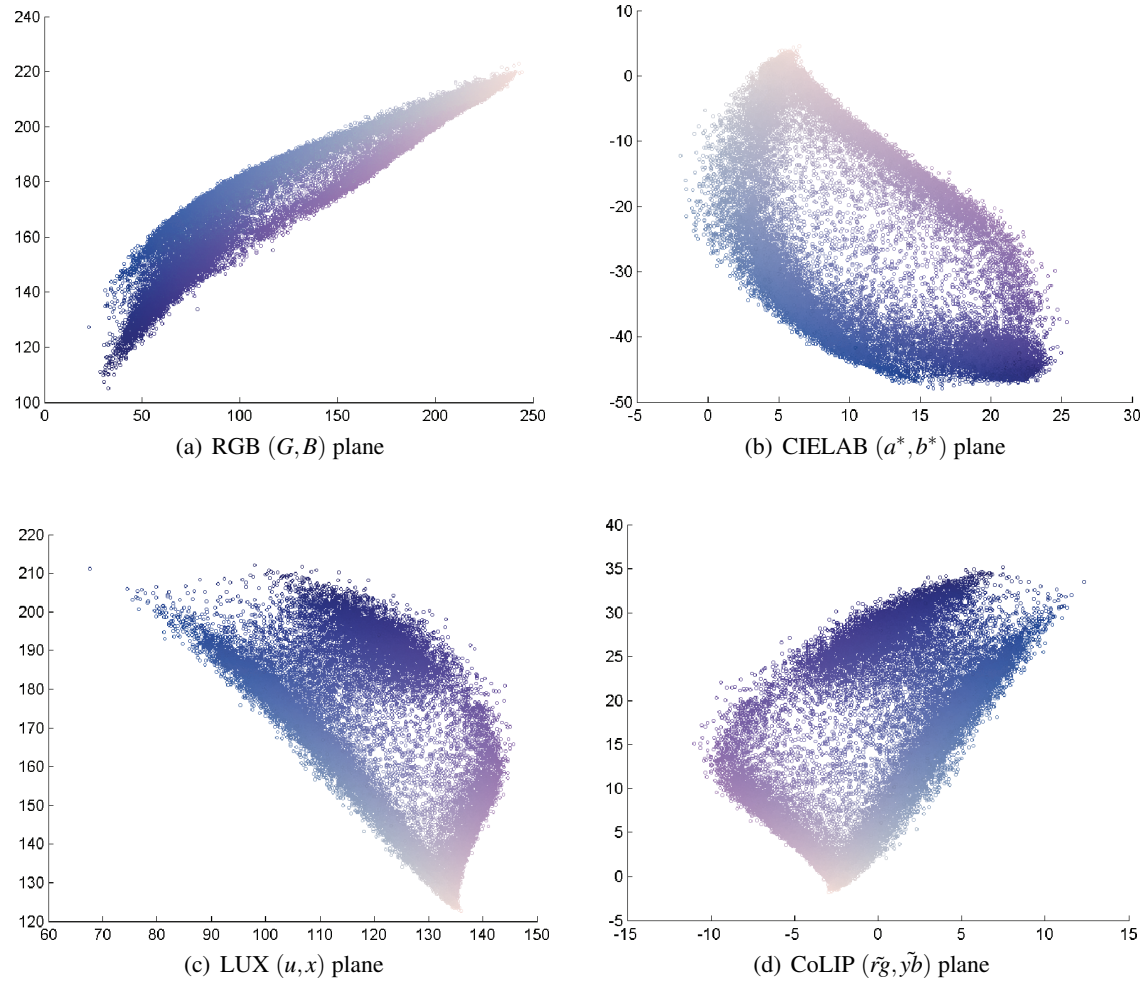

(a) RGB (G,B) plane (b) CIELAB (a^*,b^*) plane

(c) LUX (u,x) plane (d) CoLIP $(\tilde{rg},\tilde{yb})$ plane

Fig. 2. *Cell image 1 cloud of points displayed in RGB (a), CIELAB (b), LUX (c) and CoLIP(d) chromatic planes.*

a normalized inverted color intensity vector. This inverted scale has a physical meaning as images are transmitted images. The tone vector represents matter opacity. With this definition, the $(0,0,0)$ vector represents a transparent point and (M_0,M_0,M_0) corresponds to a dark point. The vector tone is valued in $[0,M_0)^3$. In the digital case, image intensities are expressed on 256 gray levels with a floor quantization. The scaling factor M_0 is set to 256 and the tone vector $\vec{f}$ is defined as follows:

$$\vec{f} = \begin{pmatrix} l \\ m \\ s \end{pmatrix} = \begin{pmatrix} M_0 - L - 1 \\ M_0 - M - 1 \\ M_0 - S - 1 \end{pmatrix}. \tag{8}$$

The cone compression is modeled in the CoLIP model by the isomorphism φ

$$\vec{\tilde{f}} = \varphi(\vec{f}) = -M_0 \ln\left(\frac{M_0 - \vec{f}}{M_0}\right). \tag{9}$$

Here the φ function is applied to each tone vector coordinates. The resulting vector is the logarithmic tone vector $\vec{\tilde{f}} = \left(\tilde{l},\tilde{m},\tilde{s}\right)$. The opponent processing is modeled in the CoLIP framework by a linear combination of the logarithmic tone vector coordinates $\tilde{l}$, $\tilde{m}$, and $\tilde{s}$ computed with the matrix P.

$$P = \begin{pmatrix} \alpha & \beta & \gamma \\ \alpha' & \beta' & \gamma' \\ \alpha'' & \beta'' & \gamma'' \end{pmatrix}. \tag{10}$$

The resulting vector is the antagonist logarithmic tone vector $\vec{\tilde{f}} = (\tilde{a},\tilde{rg},\tilde{yb})$ (where a stands for achromatic, rg for red-green and yb for yellow-blue).

$$\begin{pmatrix} \tilde{a} \\ \tilde{rg} \\ \tilde{yb} \end{pmatrix} = P * \begin{pmatrix} \tilde{l} \\ \tilde{m} \\ \tilde{s} \end{pmatrix} = \begin{pmatrix} \alpha\tilde{l} + \beta\tilde{m} + \gamma\tilde{s} \\ \alpha'\tilde{l} + \beta'\tilde{m} + \gamma'\tilde{s} \\ \alpha''\tilde{l} + \beta''\tilde{m} + \gamma''\tilde{s} \end{pmatrix}, \tag{11}$$

where parameters $\alpha,\beta,\gamma \geq 0$ define the achromatic channel, parameters $\alpha',\gamma' \geq 0$, $\beta' \leq 0$ define the red-green channel, and parameters $\alpha'',\beta'' \leq 0$, $\gamma'' \leq 0$ define the yellow-blue channel.

If $L = M = S$, the image is achromatic (gray level image). Therefore $\widetilde{rg} = 0$, $\widetilde{yb} = 0$ and $\tilde{a} = \tilde{l} = \tilde{m} = \tilde{s}$. The P matrix parameters satisfy the following relations:

$$\begin{cases} \alpha + \beta + \gamma = 1 \,, \\ \alpha' + \beta' + \gamma' = 0 \,, \\ \alpha'' + \beta'' + \gamma'' = 0 \,. \end{cases} \tag{12}$$

In this application, the antagonist transformation matrix P_{CoLIP} is (Gouinaud *et al.*, 2011):

$$P_{CoLIP} = \begin{pmatrix} 40/61 & 20/61 & 1/61 \\ 1 & -12/11 & 1/11 \\ 1/9 & 1/9 & -2/9 \end{pmatrix}. \tag{13}$$

Comparison and interests

As explained in introduction, MGG coloration produces images with blue and red dominant hues. The three interest areas, living cells' nuclei, living cells' cytoplasms, and scattered dead cells' nuclei are respectively dark purple, blue and bright purple. The aim of the segmentation is to detect disconnected living cells nuclei, in order to numerate living cells. Achromatic information on color opponent spaces do not give more information that can be found on R, G or B classical channels, since the cytoplasms and dead cells luminosity are not really different. But chromatic information, especially in color opponent spaces, could allow detecting a chromatic difference between the three interest areas. In Fig. 2 are plotted the image 1 clouds of points in the chromatic planes (R,B) in primary space RGB, (a^*,b^*) in CIELAB space, (U,X) in LUX space and $(\widetilde{rg},\widetilde{yb})$ in CoLIP space. The three interest areas appear clearly as distinct clouds of points on each diagram. On the (R,B) chromatic plane, these areas are very close but on human vision based models, these three areas are clearly distinct and even more on both LUX and CoLIP chromatic planes. As they better model the human visual perception, human vision based models allow to compute color contrast among the interest areas and to include chromatic information in the segmentation process.

Thus, chromatic information given by human vision based models can enhance the luminosity segmentation. MGG images have a dominant blue hue, so luminosity and yellow blue channel will be redundant. But, the red-green channel should give information, particularly to detect living cells cytoplasm and nuclei frontier which could be of interest to detect and numerate living cell nuclei. In Fig. 3, the red-green channel of image (a) Fig. 1 is displayed within CIELAB, LUX and CoLIP models. We can see that it allows to differentiate cytoplasm and nuclei but also dead cells. This is particularly visible on the CoLIP yellow-blue channel.

Giving all these results, the color image segmentation method described in the following section aim at detecting living cells' nuclei in detecting image pixels with achromatic and yellow-blue channel and then sharpens the cell detection disconnection in removing cytoplasm and dead cells nuclei with yellow-blue channel. Dead cells are detected on the red-green channel.

SEGMENTATION ALGORITHM

Color segmentation methods for cytological images are based on four fundamental steps. A step of pre-treatment allows checking the presence of relevant particles, smoothing the image to reduce noise, and eliminating non relevant elements. The color image is then converted in an appropriate color space. Then the algorithm main step is the relevant particles regions extraction. Here, various method can be found in the state of the art including multi-thresholding and color gradient (Lezoray *et al.*, 1999; 2003), histogram clustering (Lezoray, 2003; Lezoray and Lecluse, 2007), and pixel classification (Meurie *et al.*, 2003). This step is achieved with segmentation refinement using mathematical morphology. Eventually a step of region growing is performed, in order to disconnect and quantify the segmented particles. This is most of the time performed by a watershed algorithm.

The color segmentation method presented in this article is composed of the same fundamental four steps. The step of pre-treatment consists in extracting an automatic red scale bar that appears on some images and induces trouble in the algorithm and in smoothing the image. It is then shown that color opponent spaces (CIELAB, LUX or CoLIP) are more convenient than classical primary space to discriminate relevant areas in this type of cytological images, due to their color antagonism and logarithmic image dynamic range. The color conversion also includes a white balance algorithm in order to extract the sample background color and standardize images balance. The third step is the phase of regions extraction and it is performed using Otsu multi-thresholding. The segmentation is then enhanced by morphological filters. Eventually, the fourth and last step quantifies living and dead cells using watershed transform and evaluate sample viability. All experimental results of this study have been computed with matlab.

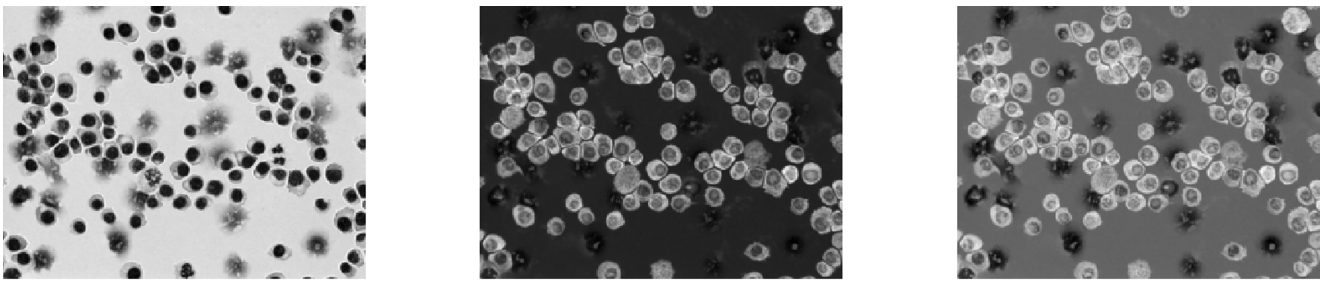

Fig. 3. *Red-green chanel in CIELAB (a), LUX (b) and CoLIP (c) color opponent models*

VIABILITY QUANTIFICATION

PRE-TREATMENT

On some images, an automatic red scale bar can appear, and induce trouble in the algorithm. A mask image of the red scale bar is created, and then pixels on the edge of the scale bar a progressively replaced by a close pixel, like an erosion, until the scale bar disappears completely. Then, the image white point, corresponding to the sample color back ground is computed. The difficulty is to define the value to give to the white point. In order to eliminate local saturation phenomenons, the white point is calculated in taking pixels that have greatest values of images on all channels until a certain percentage p of image pixels is reached, and then taking the mean of these pixels on each channel. Here $p = 1\%$ (Gouinaud *et al.*, 2011). The smoothing algorithm is performed using a median filter.

CONVERTING IMAGE FROM RGB TO THE COLOR OPPONENT SPACE

First of all, a white balance algorithm is performed on the image. Withim CIELAB model, the white balance is integrated since the white point (X_W, Y_W, Z_W) is taken into account (see Eq. 1). In LUX and CoLIP model, the white balance algorithm is the ratio of R, G, B or L, M, S chanels, respectively, to the white point R_W, G_W, B_W or L_W, M_W, S_W, respectively.

Color conversion from RGB to the human vision based space are performed following Eqs. 1, 13, and 5. Here a scale normalization is needed as chromatic scales are different in each model (see Fig. 2). CIELAB and LUX models are rescaled in order to have the CoLIP model chromatic range: $(0, M_0)$ for achromatic channel and $(-M_0, M_0)$ for chromatic channels and so that the $(0,0)$ value corresponds to the achromatic axe in the chromatic plane:

$$\begin{aligned} L^{*'} &= M_0 - L^* \\ a^{*'} &= -a^* \\ b^{*'} &= -b^* \end{aligned} \tag{14}$$

$$\begin{aligned} L^{'} &= M_0 - L \\ U^{'} &= M_0 - 2U \\ X^{'} &= 2X - M_0 \end{aligned} \tag{15}$$

SEGMENTATION

Regions and Marker extractions

Multi-thresholding segments each color space channel into N classes by means of the Otsu's multi-thresholding method, that uses intra-class variance optimization (Ostu, 1979). Achromatic and yellow-blue channels are divided into three areas corresponding to interest areas, in order to segment nuclei areas. Red-green channel is divided into 4 to 6 areas (depending on the model) to be more precise and segment dead nuclei areas. Morphological operations are computed to fill holes, remove small particles, smooth cells edges, in order to produce binary images that allow a cell quantification.

Morphology processing and watershed

The Euclidean distance to the object boundaries is first computed, and then the watershed is applied to the inverse of the distance map. The watershed algorithm is applied on both nuclei and dead nuclei markers images to disconnect close particles and quantify the number of particles. The sample viability rate is directly deduscted from the number of viable cells and dead cells.

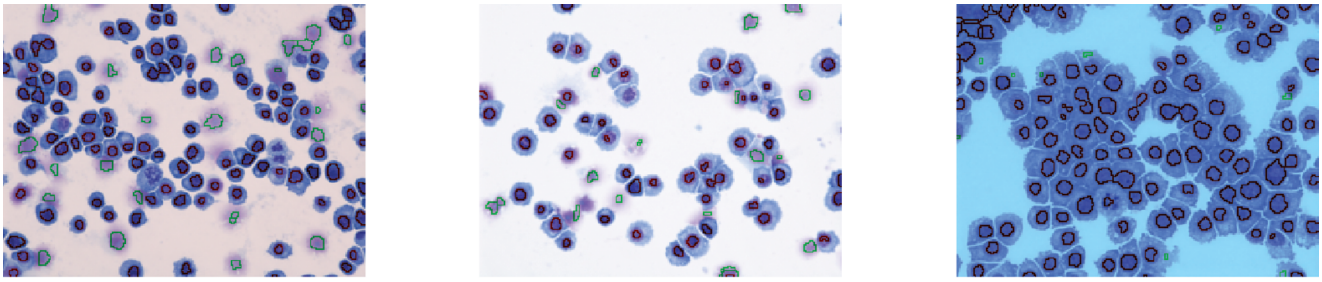

(a) (b) (c)

Fig. 4. *(a), (b), and (c): results of the color image segmentation with CoLIP model on corresponding images Fig.1. Living cells nuclei are in red and dead cells are in green.*

DISCUSSION

Result of the color segmentation algorithm on images from Fig. 1 with CoLIP model are displayed in Fig. 4. Color segmentation and numeration of living and dead cells has been tested on a data base of 32 MGG images. Exact numeration of living and dead cells has been performed by a biologist. Then, the table 1 compares absolute error average (Av) for living and dead cells (*i.e.*, the average error in number of cells) quantification and viability rate absolute error average (Av) and standard deviation (SD) in percentages on each color opponent space. The number of viable cells on the data base samples go from 47 to 195, depending on the sample. The number of dead cell is completely different from one sample to another, some have a viability rate of 100% (see Fig. 1c) and some have a viability rate of 60% with more than 50 dead cells.

Table 1. *Average (Av) absolute error of living cells and dead cells quantification and average (Av) and standard deviation (SD) of sample viability in percentage on CIELAB, LUX and CoLIP model.*

Model	Living cells	Dead cells	Viability	
	Av	Av	Av	SD
CIELAB	24.6	19.9	15.1	7.85
LUX	16.0	5.38	4.68	4.2
CoLIP	10.8	4.78	3.78	2.81

Results obtained in this study indicate that human vision based models allow to enhance simple luminosity segmentation, in adding color information. The CoLIP and LUX model give much better results than CIELAB model. CoLIP results are better on living cells and much better on dead cells. This can be explained by the fact that CoLIP red-green channel discriminate dead cells much more than CIELAB and LUX red-green channels. Viability rate error is clearly better with CoLIP and LUX model, and better within CoLIP model than LUX model considering that the standard deviation is lower and thus the viability rate error really low and really stable. Images with a blue halo (see Fig. 1c) induce trouble in the algoithm (see Fig. 4c) since the white balance remove the sample background color but also the contrast between relevant areas: special care is required during the image acquisition on the microscope, especially for the contrast balance. These results validate our method. The aim of cytological coloration such as MGG is to improve the human eye contrast. As color opponent models, and even more LIP-based color opponent models, follow each step of the human vision, any segmentation method on cytological images could probably be improved by using these models. Indeed, due to the color antagonism and the logarithmic image dynamic range, colors are much more discriminated before any segmentation method is performed.

As our segmentation method demonstrates the utility of human vision based color opponent models, it would be interesting in a near future to enhance this methodology with other morphological parameters. Indeed, macrophages are immune cells able to internalize foreign bodies during the phagocytic process leading to the formation of vesicles. Coupling cell death detection with a precise quantification of the amount of vesicles generated will be a powerful tool to assess biological important effects in toxicological studies (Nan *et al.*, 2008; Leclerc *et al.*, 2010; Song *et al.*, 2010).

REFERENCES

De Brauwer E, Jacobs J, Nieman F, Bruggeman C, Wagenaar S, Drent M (2000). Cytocentrifugation conditions affecting the differential cell count in bronchoalveolar lavage fluid. Anal Quant Cytol Histol 22:416–22.

Fairchild MD (2005). Color appearance models, 2nd Ed. Chichester: Wiley.

Gouinaud H, Gavet Y, Debayle J, Pinoli J (2011). Color correction in the framework of color logarithmic image processing. In: Lončarić S, Ramponi G, Seršić D, eds. Proc 7th Int Symp Image Signal Proc Anal (ISPA). Dubrovnik, Sept 4–6. pp. 129–33.

Jourlin M, Pinoli JC (1988). A model for logarithmic image processing. J Microsc 149:21–35.

Jourlin M, Pinoli JC (2001). Logarithmic image processing-the mathematical and physical framework for the representation and processing of transmitted images. Adv Imag Elect Phys 115:129–96.

Leclerc L, Boudard D, Pourchez J, Forest V, Sabido O, Bin V, *et al.* (2010). Quantification of microsized fluorescent particles phagocytosis to a better knowledge of toxicity mechanisms. Inhal Toxicol 22:1091–100.

Lezoray O (2003). Supervised automatic histogram clustering and watershed segmentation. application to microscopic medical images. Image Anal Stereol 22:113–20.

Lezoray O, Elmoataz A, Cardot H (2003). A color object recognition scheme: application to cellular sorting. Mach Vision Appl 14:166–71.

Lezoray O, Elmoataz A, Cardot H, Gougeon G, Lecluse M, Elie H, *et al.* (1999). Segmentation of cytological images using color and mathematical morphology. Acta Stereol 18:1–14.

Lezoray O, Lecluse M (2007). Automatic segmentation and classification of cells from broncho alveolar lavage. Image Anal Stereol 26:111–9.

Lievin M, Luthon F (2004). Nonlinear color space and spatiotemporal MRF for hierarchical segmentation of face features in video. IEEE Trans Image Process 13:63–71.

Luthon F, Beaumesnil B, Dubois N (2010). LUX color transform for mosaic image rendering. In: Miclea L, Stoian I, eds. Proc IEEE Int Conf Autom Quality Test Robot (AQTR), Cluj-Napoca. 3:1–6.

Meurie C, Lebrun G, Lezoray O, Elmoataz A (2003). A comparison of supervised pixels-based color image segmentation methods. application in cancerology. Proc WSEAS Trans Comput 2:739–44.

Nan A, Bai X, Son S, Lee S, Ghandehari H (2008). Cellular uptake and cytotoxicity of silica nanotubes. Nano Lett 8:2150–4.

Ostu N (1979). A threshold selection method from gray-level histograms. IEEE Trans Syst Man Cyb 9:62–6.

Song M, Song W, Bi H, Wang J, Wu W, Sun J, Yu M (2010). Cytotoxicity and cellular uptake of iron nanowires. Biomaterials 31:1509–17.

Image Anal Stereol 2013;32:175-181 doi:10.5566/ias.v32.p175-181
Original Research Paper

THE EULER NUMBER FROM THE DISTANCE FUNCTION

XIMO GUAL-ARNAU

Institute of New Imaging Technologies, Campus Riu Sec, Universitat Jaume I, 12071 Castelló, Spain
e-mail: gual@uji.es
(Received April 11, 2013; revised November 11, 2013; accepted November 12, 2013)

ABSTRACT

We present a new method to obtain the Euler number of a domain based on the tangent counts of concentric spheres in $\mathbb{R}^3$ (or circles in $\mathbb{R}^2$), with respect to the center O, that sweeps the domain. This method is derived from the Poincaré-Hopf Theorem, when the index of critical points of the square of the distance function with respect to the origin O is considered.

Keywords: critical points, distance function, Euler number, stereology, tangent counts.

INTRODUCTION

The Euler number describes the topology of the surfaces of a structure of interest and its practical value of obtaining, for example, the number of trabeculae in bone, the number of glomerular capillaries in kidney, or the alveolar number in lung-architecture, has been demonstrated.

Hadwiger (1957) gave an inductive definition of the Euler characteristic which has suggested several methods for deriving the Euler number from close parallel flat sections; see for instance De Hoff (1987), Gundersen *et al.* (1993), Ohser *et al.* (1996) or Rataj (2004). In this case, the principle used to obtain the Euler number of an n-dimensional domain in $\mathbb{R}^n$ ($n = 2$ or 3) is based on what happens in an $(n-1)$-dimensional plane that sweeps through the domain. Some of the methods obtained from this principle and derived from the Hadwiger definition, can also be proved from the classical Poincaré-Hopf Theorem, when the index of critical points of a family of height functions are considered (Gual-Arnau *et al.*, 2001).

It follows that, for any vector u in $\mathbb{R}^n$ ($n = 2$ or 3), the Euler number of a domain is obtained from the tangent counts of the domain and a perpendicular plane to u (or line in $\mathbb{R}^2$), that sweeps the domain. This method is isotropic in the sense that, although the tangent events depend on the direction u, the final result (Euler number) does not depend on u.

In this paper we present an alternative method to obtain the Euler number of a domain based on the tangent counts of concentric spheres in $\mathbb{R}^3$ (or circles in $\mathbb{R}^2$) that sweep the domain. The tangent counts will depend on the position of the center O of the spheres (or circles) but the final result will be the Euler number for a general position of the center O. This method is then based on what happens in a sphere in $\mathbb{R}^3$ (or circle in $\mathbb{R}^2$) that sweeps through the domain and it is obtained from the Poincaré-Hopf Theorem, when the index of critical points of the square of the distance function with respect to an origin O is considered. In fact, Chapter 6 of Milnor (1969) is deserved to show that the square distance from a chosen point, restricted to a smooth submanifold in $\mathbb{R}^n$, is indeed a function with no degenerate critical points (Morse function), for almost all chosen points for the origin O. For instance, if the domain is bounded by a sphere, the square distance restricted to the sphere is a Morse function for all reference points, except when the reference point O is the center of the sphere.

This method may be of interest in images with a prominent reference point: *e.g.*, the nucleolus of a cell or the planet earth when counting celestial objects like stars; and in images which include anisotropic particles that have approximately parallel sides (plant fibers, fibrous minerals,...).

In the first part of the paper we give the stereological versions of the principle for 3-dimensional domains in $\mathbb{R}^3$, 2-dimensional domains in $\mathbb{R}^2$ and domains with boundary in a surface $S \subset \mathbb{R}^3$. In the second part we give the detailed mathematical justifications and we relate the Euler-Poincaré characteristic with curvatures of the domain and the concentric spheres in $\mathbb{R}^3$ (or circles in $\mathbb{R}^2$).

STEREOLOGICAL FORMULAE

In this section we give an elementary version of the Euler-Poincaré characteristic of closed orientable smooth surfaces $S = \partial D$ in $\mathbb{R}^3$, of bounded domains $D \in \mathbb{R}^2$, and of domains with boundary in an orientable smooth surface S in $\mathbb{R}^3$.

The Euler-Poincaré characteristic for domains in $\mathbb{R}^2$ and $\mathbb{R}^3$ has been studied in several stereological applications (see, for instance, Gundersen *et al.*, 1993). The principle used to obtain the Euler number of an n-dimensional domain in $\mathbb{R}^n$ ($n = 2$ or 3), is based on what happens in an $(n-1)$-dimensional plane that sweeps through the domain. Here we consider a new principle based on what happens in a sphere $\mathbb{S}^2(\lambda)$ (or circle $\mathbb{S}^1(\lambda)$ in $\mathbb{R}^2$) that sweeps through the domain when the radius λ varies.

Both principles can be derived from a result of Morse (1929) that we simplify for surfaces in $\mathbb{R}^3$ and domains in $\mathbb{R}^2$. In the next section we give a more detailed mathematical justification.

CLOSED SURFACES IN $\mathbb{R}^3$

Let $f : S \longrightarrow \mathbb{R}$ be a smooth function defined on a closed orientable smooth surface. We say that $x \in S$ is a critical point if $\nabla f_x : T_xS \longrightarrow \mathbb{R}$ vanishes for every $v \in T_xS$. A critical point $x \in S$ is non degenerated if the Hessian of f at x, $(\nabla^2 f)_x : T_xS \times T_xS \longrightarrow \mathbb{R}$, is a non degenerated bilinear form, *i.e.*, for every non zero vector $v \in T_xS$, there exists a vector $w \in T_xS$ such that $(\nabla^2 f)_x(v,w) \neq 0$. A function f is called a Morse function if all its critical points are non-degenerated (Bruce *et al.*, 1984).

Theorem 1. (Morse) Let $f : S \to \mathbb{R}$ be a differentiable Morse function on a closed orientable two-dimensional surface, then

$$\chi(S) = \sum_{x \in \Sigma(f)} \mathrm{Ind}_x(f)\,, \tag{1}$$

where $\Sigma(f)$ denotes the set of singular points of f and the index, $\mathrm{Ind}_x(f)$, is given by $+1$ when x is a local extreme of f, or -1 when x is a saddle point (Morse, 1929).

That is,

$$\chi(S) = M - s + m\,, \tag{2}$$

where M, m and s denote the number of maximum, minimum and saddle, respectively, of f.

Now, we apply the above results to a particular function: the square of the distance function.

We define the square of the distance function to a generic coordinate origin $O \in \mathbb{R}^3$ as

$$\begin{aligned} d &: \mathbb{R}^3 \longrightarrow \mathbb{R} \\ x &\longrightarrow d(x) = \langle x, x \rangle = ||x||^2\,. \end{aligned} \tag{3}$$

For almost all $O \in \mathbb{R}^3$ (all but a set of measure 0), the restriction of d to S, $d|_S$, is a Morse function (Milnor, 1969). Now we will apply Theorem 1 to the square of the distance function.

The level sets are $\pi_{\lambda^2} = d^{-1}(\lambda^2) = \{x \in \mathbb{R}^3 \,/\, ||x||^2 = \lambda^2\} = \mathbb{S}^2(\lambda)$.

When we restrict d to S, the critical points $x \in \Sigma(d|_S)$ are those where the tangent plane to S at x coincides with the tangent plane to π_{λ^2} at x; *i.e.*, $T_xS = T_x\mathbb{S}^2(\lambda)$; then we give a 'stereological' interpretation of the local extreme (maximum and minimum) and saddle points of d.

Let D be a domain in $\mathbb{R}^3$ such that $\partial D = S$; then, the critical points of $d|_S$, $(x \in \Sigma(d|_S))$, can be classified as follows: $x \in \Sigma(d|_S))$ is a point of type "Island" if $d^{-1}(d(x)) = \mathbb{S}^2(\lambda)$ is locally contained in $\mathbb{R}^3 \setminus D$, (x is a local extreme (maximum) of $d|_S$); $x \in \Sigma(d|_S))$ is a point of type "Hole" if $d^{-1}(d(x))$ is locally contained in D (x is a local extreme (minimum) of $d|_S$); and $x \in \Sigma(d|_S))$ is a point of type "Bridge" if there exist points of S in the interior and in the exterior of $\mathbb{S}^2(\lambda)$ where $\mathbb{S}^2(\lambda) = d^{-1}(d(x))$, ($x$ is a saddle point of $d|_S$), (see Fig. 1).

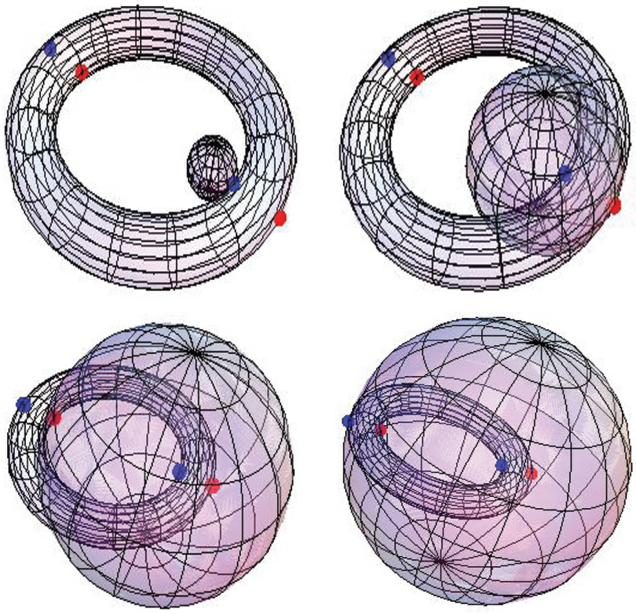

Fig. 1. *Images that we see in the sweeping spheres $\mathbb{S}^2(\lambda) \cap S$, where S is a fixed torus and the growing spheres $\mathbb{S}^2(\lambda)$ have a fixed center O. Depending on the type of critical point we have Islands or Holes (blue points) and Bridges (red points). The Euler number of the torus is 0. Note that, although S is fixed, as the radius of $\mathbb{S}^2(\lambda)$ increases, a change of scale and orientation of S (torus) appears in the images to get a better view of the critical (tangent) point.*

Let $S = \partial D \subset \mathbb{R}^3$ be an orientable smooth surface in $\mathbb{R}^3$ and let $O \in \mathbb{R}^3$ such that $d|_S$ is a Morse function. When λ varies on $\mathbb{R}$, the different spheres π_{λ^2} can be considered as a "sweeping" sphere $\mathbb{S}^2(\lambda)$ (centered at O) in $\mathbb{R}^3$. Then, Theorem 1, with the interpretation of local extrema and saddle points of $d|_S$ as Islands, Holes and Bridges, can be expressed as:

$$\chi(S) = 2\chi(D) = I_2 + H_2 - B_2 \,, \tag{4}$$

where I_2, H_2, B_2 denote the number of islands, holes and bridges observed in the "sweeping" sphere $\mathbb{S}^2(\lambda)$, which contribute to the sum $\sum_{x\in\Sigma(d|_S)} \mathrm{Ind}_x(d|_S)$.

Moreover, when $O \in S$, O is a minimum of d, and

$$\chi(S) = 2\chi(D) = 1 + I_2 + H_2 - B_2 \,. \tag{5}$$

Note that the tangent counts I_2, H_2, B_2 may depend on the position of the center O; however the final result of $(I_2 + H_2 - B_2)$ is always $2\chi(D)$ (see Fig. 2). In fact, when O is far from the domain D the tangent counts I_2, H_2, B_2 are similar to that obtained when sweeping planes are considered.

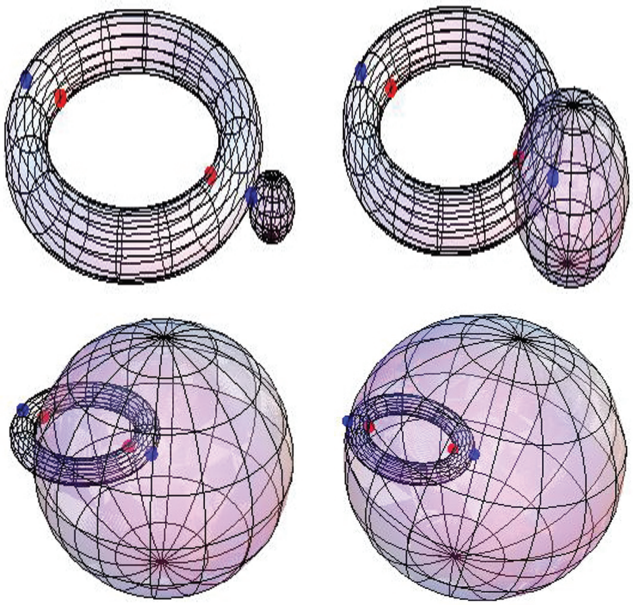

Fig. 2. *The surface S is the same as in Fig. 1 and the growing spheres $\mathbb{S}^2(\lambda)$ have a fixed origin O different to that considered in Fig. 1. Therefore, we obtain different values of the critical points, because they depend on the position of the center of the spheres, O. Blue points are Islands and red points are Bridges. The Euler number of the torus is 0.*

DOMAINS IN $\mathbb{R}^2$

Let $D \subset \mathbb{R}^2$ be a domain in $\mathbb{R}^2$ whose boundary is a curve ∂D. In this case, we can not apply Theorem 1 because D is a surface with a boundary. As explained in the Mathematical foundations section, the generalized result of Theorem 1 for domains in $\mathbb{R}^2$ is as follows:

Theorem 2. Let $D \subset \mathbb{R}^2$ be a domain with boundary and let $f : D \to \mathbb{R}$ be a Morse function such that f has no critical points on ∂D and the restriction $f|_{\partial D} : \partial D \to \mathbb{R}$ is also a Morse function. Then,

$$\chi(D) = \sum_{x\in\Sigma(f)} \mathrm{Ind}_x(f) + \frac{1}{2} \sum_{y\in\Sigma(f|_{\partial D})} \mathrm{Ind}_y(f) \,, \tag{6}$$

where the index $\mathrm{Ind}_x(f)$ is defined as in Eq. 1 and the index $\mathrm{Ind}_x(f|_{\partial D})$ is defined as follows: if the level set $f^{-1}(f(y))$ is locally contained in $\mathbb{R}^2 \setminus D$ then $\mathrm{Ind}_y(f|_{\partial D}) = +1$ and if the level set $f^{-1}(f(y))$ is locally contained in D then $\mathrm{Ind}_y(f|_{\partial D}) = -1$.

The square of the distance function to a generic coordinate origin $O \in \mathbb{R}^2$ is

$$\begin{aligned} d : \mathbb{R}^2 &\longrightarrow \mathbb{R} \\ x &\longrightarrow d(x) = \langle x, x \rangle = ||x||^2 \,. \end{aligned} \tag{7}$$

The level curves π_{λ^2} are in this case circles $\mathbb{S}^1(\lambda)$ centered at $O \in \mathbb{R}^2$.

To satisfy Theorem 2 we suppose that $O \in \mathbb{R}^2 \setminus \partial D$; then, the square of the distance function $d|_D$ has only a critical point $O \in D$; and we also suppose that the restriction of the square of the distance function $d|_{\partial D}$ is a Morse function; then, from Eq. 6,

$$\chi(D) = \delta_0(D) + \frac{1}{2} \sum_{y\in\Sigma(d|_{\partial D})} \mathrm{Ind}_y(d|_{\partial D}) \,, \tag{8}$$

where

$$\delta_0(D) = \begin{cases} 1, \text{ if } O \in D \,, \\ 0, \text{ if } O \notin D \,, \end{cases} \tag{9}$$

and a critical point $y \in \Sigma(d|_{\partial D})$ is a point of type "Island" if $d^{-1}(d(y)) = \mathbb{S}^1(\lambda)$ is locally contained in $\mathbb{R}^2 \setminus D$; and $y \in \Sigma(d|_{\partial D})$) is a point of type "Bridge" if $d^{-1}(d(y))$ is locally contained in D (see Fig. 3).

Therefore, when λ varies on $\mathbb{R}$, the different circles $\mathbb{S}^1(\lambda)$ can be considered as "sweeping" circles in $\mathbb{R}^2$, and Eq. 6 can be expressed as:

$$\chi(D) = \delta_0(D) + \frac{1}{2}(I_1 - B_1) \,, \tag{10}$$

where I_1 and B_1 denote the number of islands and bridges observed in the "sweeping" circle $\mathbb{S}^1(\lambda)$.

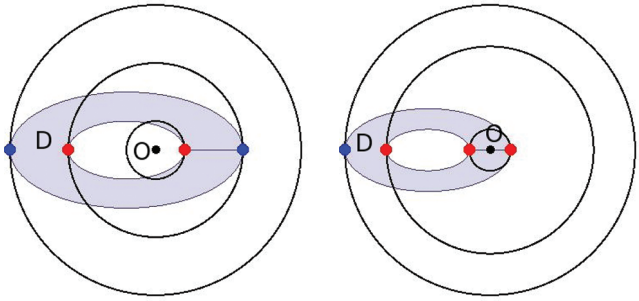

a) $O \notin D$. b) $O \in D$.

Fig. 3. *Different values of the critical points, depending on the position of the center of the growing circles, O. Blue points are Islands and red points are Bridges. The Euler number of the domain D is 0.*

Note that when the point $O \notin D$, Eq. 10 can be expressed as:

$$\chi(D) = \frac{1}{2}(I_1 - B_1)\,, \tag{11}$$

which, when O is far from D, is similar to that obtained in Gundersen *et al.* (1993), where I_1 and B_1 denote the number of islands and bridges observed in a "sweeping" line.

SURFACES WITH BOUNDARY IN $\mathbb{R}^3$

Let $D \subset S \subset \mathbb{R}^3$ be a domain with boundary in an orientable smooth surface S in $\mathbb{R}^3$ and let $O \in \mathbb{R}^3$ such that Eq. 14 is satisfied in this case. When λ varies on $\mathbb{R}^+$, the different spheres $\mathbb{S}^2(\lambda)$ can be considered as a sweeping sphere in $\mathbb{R}^3$, and

$$\chi(D) = (I_2 - B_2) + \frac{1}{2}(I_1 - B_1)\,, \tag{12}$$

where I_2, B_2 are defined as in Eq. 4 and I_1, B_1 denote the number of islands and bridges, respectively, observed in the level curves $\mathbb{S}^2(\lambda) \cap S$. In Fig. 4 we consider a domain D in a cylinder, whose boundary is given by two circles (black curves), and we show two critical points: an Island where the level curve $S \cap \mathbb{S}^2(\lambda)$ (red curve) is locally contained in $S \setminus D$, and a Bridge point, where the level curve is locally contained in D.

MATHEMATICAL FOUNDATIONS

The classical Poincaré-Hopf Theorem states that if S is a closed orientable smooth surface and v is a smooth vector field on S with isolated zeros, then

$$\chi(S) = \sum_{v(x)=0} \mathrm{Ind}_x(v)\,,$$

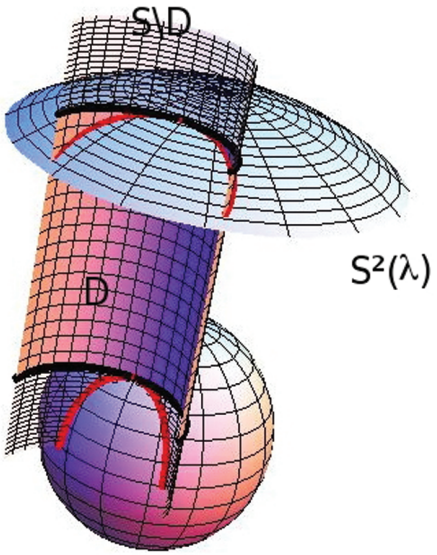

Fig. 4. *Partial view of the domain D. The boundary ∂D is given by the black curves (circles). The red curves correspond to $S \cap \mathbb{S}^2(\lambda)$.*

where $\chi(S)$ is the Euler-Poincaré characteristic of S and the index, $\mathrm{Ind}_x(v)$, is just the local degree of v at x; that is, the degree of the map $u : S \longrightarrow \mathbb{S}^2$ given by $u(z) = v(z)/|v(z)|$. As an immediate consequence, we see that if $f : S \to \mathbb{R}$ is a Morse function (that is, a function with non-degenerate critical points), then

$$\chi(S) = \sum_{x \in \Sigma(f)} \mathrm{Ind}_x(f)\,, \tag{13}$$

where $\Sigma(f)$ denotes the set of singular points of f and the index, $\mathrm{Ind}_x(f)$, is given by $+1$ when x is a local extreme of f, or -1 when x is a saddle point (Morse, 1929).

Now, we consider a generalization of the classical Poincaré-Hopf Theorem which can be applied domains with boundary in an orientable smooth surface in $\mathbb{R}^3$ and, in particular, to closed domains in $\mathbb{R}^2$ (Gual-Arnau *et al.*, 2001).

Let $D \subset \mathbb{R}^3$ be a compact orientable smooth surface with boundary and let $f : D \to \mathbb{R}$ be a Morse function such that f has no critical points on ∂D and the restriction $f|_{\partial D} : \partial D \to \mathbb{R}$ is also a Morse function. Then, the Poincaré-Hopf Theorem (Morse, 1929), states

$$\chi(D) = \sum_{x \in \Sigma(f)} \mathrm{Ind}_x(f) + \frac{1}{2} \sum_{y \in \Sigma(f|_{\partial D})} \mathrm{Ind}_y(f)\,, \tag{14}$$

where the index $\mathrm{Ind}_x(f)$ is defined as in Eq. 1 and the index $\mathrm{Ind}_x(f|_{\partial D})$ is defined as follows: if the level set $f^{-1}(f(y))$ is not locally contained in D then

$\mathrm{Ind}_y(f|_{\partial D}) = +1$ and if the level set $f^{-1}(f(y))$ is locally contained in D then $\mathrm{Ind}_y(f|_{\partial D}) = -1$.

In the next section we will consider a particular function f, the square of the distance function, and we will interpret Eq. 1 in terms of critical points of this function.

CLOSED SURFACES IN $\mathbb{R}^3$

Let S be a closed orientable smooth surface in $\mathbb{R}^3$. Given $x \in S$, we denote by $N(x)$ and $K(x)$ the normal vector and the Gauss curvature of S, respectively.

Theorem 3. Let $S \subset \mathbb{R}^3$ be a closed orientable smooth surface in $\mathbb{R}^3$.

1. Let $x \in S$. It is a critical point of $d|_S$ if and only if $x = \pm\lambda N(x)$ if and only if $T_xS = T_x\mathbb{S}^2(\lambda)$ (where $d(x) = \lambda^2$).
2. Let $x \in S$ be a critical point of $d|_S$.
   (a) Suppose that $x = -\lambda N(x)$; then x is non-degenerate if and only if $\kappa_1 \neq \frac{1}{\lambda}$ and $\kappa_2 \neq \frac{1}{\lambda}$ ($\frac{1}{\lambda^2}$ is the Gauss curvature of $\mathbb{S}^2(\lambda)$). Moreover, it is a local extreme or a saddle point of $d|_S$ depending on weather $(\frac{1}{\lambda} - \kappa_1)(\frac{1}{\lambda} - \kappa_2)$ is positive or negative, respectively.
   (b) Suppose that $x = \lambda N(x)$; then x is non-degenerate if and only if $\kappa_1 \neq -\frac{1}{\lambda}$ and $\kappa_2 \neq -\frac{1}{\lambda}$. Moreover, it is a local extreme or a saddle point of $d|_S$ depending on weather $(\frac{1}{\lambda} + \kappa_1)(\frac{1}{\lambda} + \kappa_2)$ is positive or negative, respectively.

Proof. To prove part 1 we consider

$$\begin{aligned}(\nabla d)_x(v) &= \frac{d}{dt}|_{t=0}||\alpha(t)||^2 \\ &= 2\langle\alpha'(0),\alpha(0)\rangle = 2\langle v,x\rangle\ ,\end{aligned} \tag{15}$$

where $\alpha : (-\varepsilon,\varepsilon) \longrightarrow S$ is a differentiable curve with $\alpha(0) = x$ and $\alpha'(0) = v$. Then, $(\nabla d)_x(v) = 0$ if and only if $v \perp x$ if and only if $x = \pm\lambda N(x)$ if and only if $N(x) \perp T_x\mathbb{S}^2(\lambda)$ ($||x|| = \lambda$) if and only if $T_xS = T_x\mathbb{S}^2(\lambda)$. An alternative proof using local coordinates can be found in Milnor (1969).

To prove part 2a we consider the Hessian of d at x,

$$\begin{aligned}(\nabla^2 d)_x(v) &= \frac{d^2}{dt^2}|_{t=0}||\alpha(t)||^2 = 2\frac{d}{dt}|_{t=0}\langle\alpha'(t),\alpha(t)\rangle \\ &= 2(\langle\alpha''(0),\alpha(0)\rangle + \langle\alpha'(0),\alpha'(0)\rangle) \\ &= 2(\langle\alpha''(0),-\lambda N(x)\rangle + \langle v,v\rangle)\ .\end{aligned} \tag{16}$$

Now, if we take derivatives at $t = 0$ of the identity $\langle\alpha'(t),-\lambda N(\alpha(t))\rangle = 0$ we obtain

$$\langle\alpha''(0),-\lambda N(x)\rangle = -\langle v,-\lambda dN(x)(v)\rangle\ .$$

Since the second fundamental form of S at x is defined as $II_x(v,v) = -\langle dN(x)(v),v\rangle$ and it is symmetric, we obtain

$$(\nabla^2 d)_x(v) = 2(||v||^2 - \lambda II_x(v,v))\ . \tag{17}$$

Let $\{e_1,e_2\}$ be a principal orthonormal frame at x; then, in matrix form we have

$$(\nabla^2 d)_x(v) = v\begin{pmatrix} 1-\lambda\kappa_1 & 0 \\ 0 & 1-\lambda\kappa_2 \end{pmatrix}v^T. \tag{18}$$

So, x is non-degenerate if $(1-\lambda\kappa_1)(1-\lambda\kappa_2) \neq 0$; that is, $\kappa_1 \neq \frac{1}{\lambda}$ and $\kappa_2 \neq \frac{1}{\lambda}$. The rest of part 2a is derived from the classification of local extrema and the proof of part 2b is similar. □

Corollary 1. Let $S \subset \mathbb{R}^3$ be a closed orientable smooth surface in $\mathbb{R}^3$. Then

$$\begin{aligned}\chi(S) = &\sum_{x\in S/x=-\lambda N(x)} \mathrm{sign}(1-\lambda\kappa_1)(1-\lambda\kappa_2) \\ &+ \sum_{x\in S/x=\lambda N(x)} \mathrm{sign}(1+\lambda\kappa_1)(1+\lambda\kappa_2) \\ = &\sum_{x\in S/x=-\lambda N(x)} \mathrm{sign}(1-2\lambda H(x)+\lambda^2 K(x)) \\ &+ \sum_{x\in S/x=\lambda N(x)} \mathrm{sign}(1+2\lambda H(x)+\lambda^2 K(x))\ .\end{aligned} \tag{19}$$

where $H(x)$ denotes the mean curvature of S at x.

Proof. This formula is a direct consequence of Eq. 1 and Theorem 3. □

Remark. In Milnor (1969) it is proved that for almost all $O \in \mathbb{R}^3$ the function $d|_S$ is a Morse function; *i.e.*, in general, all the critical points of $d|_S$ are non-degenerate (these points are characterized in Theorem 3). When $O \in S$, from Eqs. 15 and 16, we have that $d|_S$ has a non-degenerate critical point (minimum) at $x = O$. In this case $\mathrm{Ind}_O(d|_S) = +1$.

DOMAINS IN $\mathbb{R}^2$

Let $D \subset \mathbb{R}^2$ be a domain with boundary. As in the preceding section, we consider now the square of the distance function $d : \mathbb{R}^2 \to \mathbb{R}$, instead of the square of the distance function of $\mathbb{R}^3$. The level curves π_{λ^2} are in this case circles $\mathbb{S}^1(\lambda)$.

We suppose that the origin $O \in \mathbb{R}^2 \setminus \partial D$, then, the square of the distance function $d|_D$ only has the point O as critical point (minimum) if $O \in D$ (the distance function d defined in D is given now by $d(x,y) = x^2 + y^2$; and this function has a minimum at the point

$O = (0,0) \in D$). Moreover, in general, the restriction of the square of the distance function $d|_{\partial D}$ is a Morse function; then, from Eq. 14,

$$\chi(D) = \delta_0(D) + \frac{1}{2} \sum_{y \in \Sigma(d|_{\partial D})} \mathrm{Ind}_y(d|_{\partial D}) \,, \qquad (20)$$

where

$$\delta_0(D) = \begin{cases} 1, \text{ if } O \in D \,, \\ 0, \text{ if } O \notin D \,. \end{cases} \qquad (21)$$

Lemma 1. Let $D \subset \mathbb{R}^2$ be a domain with boundary; then,

$$\chi(D) = \delta_0(D) + \frac{1}{2} \left(\sum_{y \in \partial D \,/\, y = -\lambda n(y)} \mathrm{sign} \left(\kappa - \frac{1}{\lambda} \right) + \sum_{y \in \partial D \,/\, y = \lambda n(y)} \mathrm{sign} \left(\kappa + \frac{1}{\lambda} \right) \right) , \qquad (22)$$

where $n(y)$ and $\kappa(y)$ are the normal vector and the curvature of the plane curve ∂D, respectively.

Proof. Suppose that α is a parameterization by arc length of ∂D. Given a point $y \in \Sigma(d|_{\partial D})$, with $\alpha(s_0) = y$, we have $Dd(s_0) = \langle \alpha'(s_0), \alpha(s_0) \rangle = 0$, then $\alpha'(s_0)$ is tangent to $S^1(\lambda)$ at y. Moreover, $D^2 h_u(s_0) = \langle \alpha''(s_0), \alpha(s_0) \rangle + \langle \alpha'(s_0), \alpha'(s_0) \rangle = \langle \kappa(y) n(y), \pm \lambda n(y) \rangle + 1 = 1 \pm \lambda \kappa(y)$ so y is a local extreme. Finally, from the way we have chosen the orientation on ∂D and the definition of $\mathrm{Ind}_y(h_u|_{\partial D})$ given in Eq. 14, we have the result. □

SURFACES WITH BOUNDARY IN $\mathbb{R}^3$

Let $D \subset S \subset \mathbb{R}^3$ be a domain with boundary in an orientable smooth surface S in $\mathbb{R}^3$ (Gual-Arnau *et al.*, 2001). Parts 1 and 2 of Theorem 3 are valid here when we restrict $d|_D$ and $x \in D$.

We will give a geometrical interpretation of the critical points of $d|_{\partial D}$. The level sets $S \cap \mathbb{S}^2(\lambda)$ and $D \cap \mathbb{S}^2(\lambda)$ are now curves in S. Given $y \in \partial D$, let $n(y)$ and $\kappa_g(y)$ denote the normal vector and the geodesic curvature of ∂D in D at y, respectively. We consider the orientation in ∂D such that $n(y)$ points to the interior of D. Let $\kappa_g^0(y)$ denote the geodesic curvature of the level curve $D \cap \mathbb{S}^2(\lambda)$ at a regular point y of $d|_D$. If the curves $S \cap \mathbb{S}^2(\lambda)$ and ∂D are tangent at y we choose in $S \cap \mathbb{S}^2(\lambda)$ the same orientation.

Theorem 4. Let D be a domain with boundary in an orientable smooth surface S in $\mathbb{R}^3$.

1. Let $y \in \partial D$ be a regular point of $d|_D$. y is a critical point of $d|_{\partial D}$ if and only if the curves $D \cap \mathbb{S}^2(\lambda)$ and ∂D are tangent at y.
2. Let $y \in \partial D$ be a regular point of $d|_D$ and a critical point of $d|_{\partial D}$. y is non-degenerate if and only if $\kappa_g(y) \neq \kappa_g^0(y)$. Moreover, it is an island when $\kappa_g(y) \rangle \kappa_g^0(y)$ and it is a bridge when $\kappa_g(y) \langle \kappa_g^0(y)$.

Proof. Suppose that $\beta(s)$ is a parameterization of $S \cap \mathbb{S}^2(\lambda)$ by arc length with $\alpha(s_0) = y$. The vector y can be expressed as

$$\begin{aligned} y = & \langle y, N(y) \rangle N(y) + \langle y, \beta'(s_0) \rangle \beta'(s_0) \\ & + \langle y, N(y) \wedge \beta'(s_0) \rangle N(y) \wedge \beta'(s_0) \,. \end{aligned} \qquad (23)$$

Since $\langle \beta(s), \beta(s) \rangle = \lambda^2$ we have that $\langle \beta'(s_0), y \rangle = 0$.

Suppose now that $\alpha(s)$ is a parameterization of ∂D by arc length with $\beta(s_0) = y$. Then,

$$\begin{aligned} y = & \langle y, N(y) \rangle N(y) + \langle y, \alpha'(s_0) \rangle \alpha'(s_0) \\ & + \langle y, N(y) \wedge \alpha'(s_0) \rangle N(y) \wedge \alpha'(s_0) \,, \end{aligned} \qquad (24)$$

where $N(y) \wedge \alpha'(s_0) = n(y)$.

y is a critical point of $d|_{\partial D}$ if $\langle y, \alpha'(s_0) \rangle = 0$. Since y is a regular point of $d|_D$, from Theorem 3 we have that $y \neq \lambda N(y)$; then, from Eqs. 23 and 24, y is a critical point of $d|_{\partial D}$ if and only if the normal vectors to α and β in $T_y \partial D$ coincide, and therefore the curves $D \cap \mathbb{S}^2(\lambda)$ and ∂D are tangent at y.

To prove the second part of the theorem we suppose that $y = \alpha(s_0)$ is a critical point of $d|_{\partial D}$, *i.e.*, $\langle \alpha'(s_0), \alpha(s_0) \rangle = 0$.

y will be a degenerate critical point of $d|_{\partial D}$ if

$$\langle \alpha''(s_0), \alpha(s_0) \rangle + \langle \alpha'(s_0), \alpha'(s_0) \rangle = 0 \,,$$

that is, $\langle \alpha''(s_0), \alpha(s_0) \rangle = -1$.

Since $\langle \beta(s), \beta(s) \rangle = \lambda^2$ we have that $\langle \beta''(s_0), \beta(s_0) \rangle = -1$.

On the other hand,

$$\langle \alpha''(s_0), y \rangle = \kappa_n(y) \langle y, N(y) \rangle + \kappa_g(y) \langle y, n(y) \rangle \,, \qquad (25)$$

$$\langle \beta''(s_0), y \rangle = \kappa_n(y) \langle y, N(y) \rangle + \kappa_g^0(y) \langle y, n(y) \rangle \,, \qquad (26)$$

where the normal curvature $\kappa_n(y)$ of α at y coincides, from the Meusnier's theorem, with the normal curvature of β at y. Then, subtracting Eq. 26 to Eq. 25, we obtain

$$\langle \alpha''(s_0), y \rangle + 1 = (\kappa_g(y) - \kappa_g^0(y)) \langle y, n(y) \rangle \,. \qquad (27)$$

Finally, since $\langle y, n(y) \rangle \neq 0$, we conclude that y is non-degenerate if and only if $\kappa_g(y) \neq \kappa_g^0(y)$. The fact that the cases $\kappa_g(y) \rangle \kappa_g^0(y)$ and $\kappa_g(y) \langle \kappa_g^0(y)$ correspond to an island or bridge, respectively, can be deduced from the orientation we have chosen on ∂D. □

ACKNOWLEDGEMENTS

This research was supported by the Spanish Ministry of Education and Science I+D Project MTM2009-14500-C02-02, the UJI project P11B2012-24 and the PROMETEO/2010/028 project.

REFERENCES

Bruce JW, Giblin PJ (1984). Curves and singularities. Cambridge: Cambridge University Press.

De Hoff RT (1987). Use of the disector to estimate the Euler characteristics of three-dimensional micro structures. Acta Stereol 6:133–40.

Gual-Arnau X, Nuño-Ballesteros JJ (2001). A stereological version of the Gauss-Bonnet formula. Geometriae Dedicata 84:253–60.

Gundersen HJG, Boyce RW, Nyengaard JR, Odgaard A (1993). The conneulor: unbiased estimation of connectivity using physical disectors under projection. Bone 14:217–22.

Hadwiger H (1957). Vorlesungen über Inhalt, Oberfläche und Isoperimetrie. Berlin: Springer Verlag.

Milnor JW (1969). Morse theory. Princeton University Press.

Morse M (1929). Singular points of vector fields under general boundary conditions. Amer J Math 51:165-78.

Ohser J, Nagel W (1996). The estimation of the Euler-Poincaré characteristic from observations on parallel sections. J Microsc 184:117–26.

Rataj J (2004). On estimation of the Euler number by projections on thin slabs. Adv Appl Prob (SGSA) 36:715–24.

Santaló LA (1976). Integral geometry and geometric probability. London: Addison-Wesley.

Teufel E (1982). Differential topology and the computation of total absolute curvature. Math Ann 258:471–80.

Image Anal Stereol 2013;32:183-188 doi:10.5566/ias.v32.p183-188
Short Research Communication

COLLAGE-BASED INVERSE PROBLEMS FOR IFSM WITH ENTROPY MAXIMIZATION AND SPARSITY CONSTRAINTS

HERB KUNZE✉,[1], DAVIDE LA TORRE[2] AND EDWARD VRSCAY[3]

[1]Department of Mathematics and Statistics, University of Guelph, Guelph, Ontario, Canada; [2]Department of Applied Mathematics and Sciences, Khalifa University, Abu Dhabi, UAE and Department of Economics, Management and Quantitative Methods, University of Milan, Italy; [3]Department of Applied Mathematics, University of Waterloo, Ontario, Canada
e-mail: hkunze@uoguelph.ca, davide.latorre@unimi.it, ervrscay@uwaterloo.ca
(Received July 8, 2013; revised November 1, 2013; accepted November 1, 2013)

ABSTRACT

We consider the inverse problem associated with IFSM: Given a target function f, find an IFSM, such that its invariant fixed point $\bar{f}$ is sufficiently close to f in the L^p distance. In this paper, we extend the collage-based method developed by Forte and Vrscay (1995) along two different directions. We first search for a set of mappings that not only minimizes the collage error but also maximizes the entropy of the dynamical system. We then include an extra term in the minimization process which takes into account the sparsity of the set of mappings. In this new formulation, the minimization of collage error is treated as multi-criteria problem: we consider three different and conflicting criteria *i.e.*, collage error, entropy and sparsity. To solve this multi-criteria program we proceed by scalarization and we reduce the model to a single-criterion program by combining all objective functions with different trade-off weights. The results of some numerical computations are presented. Numerical studies indicate that a maximum entropy principle exists for this approximation problem, *i.e.*, that the suboptimal solutions produced by collage coding can be improved at least slightly by adding a maximum entropy criterion.

Keywords: collage theorem, entropy, fractal transforms, iterated function systems with mappings, sparsity.

INTRODUCTION

In fractal image coding based on Generalized Fractal Transforms (GFT), one seeks to approximate a target image or signal v by the fixed point $\bar{u}$ of a contractive fractal transform operator T. The usual formulation involves a fixed set of geometric contraction maps along with a corresponding set of greyscale maps. The inverse problem, which involves the determination of the best greyscale map parameters for a given target image, is based on the so-called "Collage Theorem", a simple consequence of Banach's fixed point theorem. Another consequence of Banach's fixed point result is that the approximation of the target image or signal can be generated by iteration of the fractal transform (see Hutchinson, 1981; Barnsley et al., 1985; Barnsley and Demko, 1985; Barnsley, 1989; Barnsley and Hurd, 1993; Forte and Vrscay, 1995; 1999; Iacus and La Torre, 2005a; 2005b; Kunze et al., 2008; 2009; 2012a; 2012b; La Torre et al., 2009; La Torre and Vrscay, 2009; 2011). In Forte and Vrscay (1995), the authors showed that one can find an iterated function system with greyscale maps (IFSM) to approximate any target signal or image with arbitrary precision, and they provided a suboptimal but systematic "collage-based" approach for doing so.

In this paper we extend the approach developed in Forte and Vrscay (1995) along two different – in fact, competing – directions, namely, entropy and sparsity. First, we search for a set of mappings and greyscale map parameters that not only minimizes the so-called *collage error* but also maximizes the entropy of the parameter set. A motivation for this procedure is as follows. As stated earlier, given a target image v, one would ideally like to find a contractive fractal transform T with fixed point $\bar{u}$ that is as close as possible to v, *i.e.*, which minimizes the approximation error given by the distance $E(u) = d(v,u)$. This problem, however, is enormously difficult and impractical. The Collage Theorem provides a significant simplification in that one searches for a fractal transform T – as defined by its fractal parameters – which minimizes the "collage distance" $d(v,Tv)$. Such a procedure is often easy to formulate and solve algorithmically. As may be expected, however, the fractal transform T_c yielded by this collage-based method is suboptimal, *i.e.*, its fixed point $\bar{u}_c$ does not minimize the true approximation error $E(u)$. As such, we may consider the parameters defining the suboptimal fractal transform T_c as representing "incomplete" or "partial information." We now apply the maximum entropy principle of Jaynes (1957), *i.e.*, "making inferences on the basis of partial information we must use that probability distribution

which has maximum entropy subject to whatever is known." Here, a suitable probability distribution over the relevant fractal parameters is defined and employed.

Second, we examine the effects of maximizing the *sparsity* of the set of greyscale parameters, *i.e.*, forcing as many of these parameters as possible to be zero. The motivation of this approach is as follows. The parameters defining the suboptimal transform T_c are once again viewed as representing an approximation to the true solution. We now borrow from sparsity studies in signal and image processing, where it is often found that a signal/image is well approximated by a vector of coefficients with a small number of nonzeros (see Elad, 2010) – in other words, a vector with *high sparsity*.

In the new formulation presented in this paper, the minimization of collage error is studied as a multi-criteria problem. Three different and conflicting criteria are considered, namely collage error, entropy and sparsity. In order to reduce the complexity of this model, we employ a scalarization technique which allows the multi-criteria program to be reduced to a single-criterion program by combining all objective functions with different trade-off weights. This new approach is illustrated through some numerical examples which indicate that a maximum entropy principle does exist for this approximation problem, *i.e.*, that the suboptimal solutions produced by collage coding can be improved at least slightly by adding a maximum entropy criterion. Similar results were obtained in the context of measure approximation using Iterated Function System with Probabilities (IFSP) by La Torre and Vrscay (2012) and in the analysis of inverse problems for differential equations by collage methods in Kunze et al. (2012).

ITERATED FUNCTION SYSTEMS ON FUNCTIONS: SOME BASICS

The action of a GFT $T : X \to X$ on an element u of the complete metric space (X,d) can be summarized in the following steps. It produces a set of N spatially-contracted copies of u and then it modifies the values of these copies by means of a suitable range-mapping. Finally, it recombines them using an appropriate operator in order to get the element $v \in X$, $v = Tu$. In all these cases, under appropriate conditions, the fractal transform T is a contraction and thus Banach's fixed point theorem guarantees the existence of a unique fixed point $\bar{u} = T\bar{u}$. The inverse problem is a key factor for applications: given $T : X \to X$ a point-to-point contraction mapping and a "target" element $v \in X$, we look for a contraction mapping T with fixed point $\bar{u}$ such that $d(v,\bar{u})$ is as small as possible. In practical applications, however, it is difficult to construct solutions to this problem and one relies on the following simple consequence of Banach's fixed point theorem, known in the fractal coding literature as the *collage theorem*, which states that

$$d(v,\bar{u}) \leq \frac{1}{1-c} d(v,Tv) \tag{1}$$

(c is the contractivity factor of T). Instead of trying to minimize the error $d(v,\bar{u})$, one looks for a contraction mapping T that minimizes the *collage error* $d(v,Tv)$. In this section we focus on the method of iterated function systems with greyscale maps (IFSM), as formulated by Forte and Vrscay (1995), a GFT which can be used to approximate a given element u of $L^2([0,1])$.

We consider the case in which $u : [0,1] \to [0,1]$ and the space

$$X = \left\{ u : [0,1] \to [0,1], u \in L^2[0,1] \right\} . \tag{2}$$

The ingredients of an N-map IFSM on X are

1. a set of N contractive mappings $w = \{w_1, w_2, \ldots, w_N\}$, $w_i(x) : [0,1] \to [0,1]$, most often affine in form:

$$w_i(x) = s_i x + a_i , \quad 0 \leq s_i < 1, \quad i = 1,2,\ldots,N; \tag{3}$$

2. a set of associated functions—the greyscale maps—$\phi = \{\phi_1, \phi_2, \ldots, \phi_N\}$, $\phi_i : \mathbb{R} \to \mathbb{R}$. Affine maps are usually employed:

$$\phi_i(t) = \alpha_i t + \beta_i , \tag{4}$$

with the conditions

$$\alpha_i, \beta_i \in [0,1] \tag{5}$$

and

$$0 \leq \sum_{i=1}^{N} \alpha_i + \beta_i < 1 . \tag{6}$$

Associated with the N-map IFSM (w,ϕ) is the *fractal transform* operator T, the action of which on a function $u \in X$ is given by

$$(Tu)(x) = \sum_{i=1}^{N}{}' \phi_i(u(w_i^{-1}(x))) , \tag{7}$$

where the prime means that the sum operates on all those terms for which w_i^{-1} is defined.

Theorem 1. *(Forte and Vrscay, 1995) $T : X \to X$ and for any $u, v \in X$ we have*

$$d_2(Tu, Tv) \leq C d_2(u, v) \,, \tag{8}$$

where

$$C = \sum_{i=1}^{N} s_i^{\frac{1}{2}} \alpha_i \,. \tag{9}$$

When $C < 1$, then T is contractive on X, implying the existence of a unique fixed point $\bar{u} \in X$ such that $\bar{u} = T\bar{u}$.

The inverse problem associated with IFSM can, in principle, be solved to arbitrary accuracy, using a procedure defined in Forte and Vrscay (1995). The squared collage distance function associated with an N-map IFSM may be written as a quadratic form,

$$\Delta^2 = z^T A z + b^T z + c \,, \tag{10}$$

where $z = (\alpha_1, \ldots \alpha_N, \beta_1, \ldots, \beta_N)$. The maps w_k are chosen from an infinite set W of fixed affine contraction maps on $[0,1]$ which satisfy the following properties.

Definition 2.1. *We say that W generates an m-dense and nonoverlapping family A of subsets of I if for every $\varepsilon > 0$ and every $B \subset I$ there exists a finite set of integers i_k, $i_k \geq 1$, $1 \leq k \leq N$, such that*

- $A = \cup_{k=1}^{N} w_{i_k}(I) \subset B$,
- $m(B \backslash A) < \varepsilon$, *and*
- $m(w_{i_k}(I) \cap w_{i_l}(I)) = 0$ *if* $k \neq l$,

where m denotes Lebesgue measure.

Let

$$W^N = \{w_1, \ldots w_N\} \tag{11}$$

be the N truncations of w. Let $\Phi^N = \{\phi_1, \ldots, \phi_N\}$ be the N-vector of affine grey level maps. Let Ω be a compact subset of set $\mathbb{R}^{2N}$ which describes the set of all possible constraints and let z_N be the solution of the previous quadratic optimization problem over Ω. Let $\Delta^2_{N,min} = \Delta^2_N(z_N)$. In Forte and Vrscay (1995), the following result was proved.

Theorem 2.

$$\Delta^2_{N,min} \to 0 \; as \; N \to \infty \,.$$

Using the Collage Theorem, the inverse problem may be solved to arbitrary accuracy. A practical choice for the contraction maps w on $X = [0,1]$ is

$$w_{ij}(x) = 2^{-i}(x + j - 1), \; i = 1, 2, \ldots, \; j = 1, 2, \ldots, 2^i.$$

COLLAGE ERROR MINIMIZATION, ENTROPY AND SPARSITY MAXIMIZATION

Solutions to the optimization problem,

$$\min_{z \in \Omega} \Delta_2(z) \tag{12}$$

using a quadratic programming algorithm were presented in Forte and Vrscay (1995). Here we consider an extension of the above optimization problem which includes two additional objective functions, namely, maximum entropy and sparsity. The reasons for adding these two criteria were discussed in the Introduction but we recall them briefly here.

On the one hand, it is desired to improve the results obtained from the collage-based method, acknowledged as being suboptimal, thereby obtaining a better approximation of the target image. In fact, from Eq. (1), we see that the collage error $d(v, Tv)$ provides an upper bound to the error, $d(v, \bar{u})$, in approximating the target v with the fixed point $\bar{u}$ of T. We consider the maximum entropy principle as a way of improving the collage-based approximation.

On the other hand, collage error minimization often provides a solution with several nonzero coefficients, many of them being very close to zero. Once again borrowing the idea of sparsity from signal/image processing, it seems to be quite natural to ask – especially in the context of data compression – if there exists an alternative solution which possesses a lesser number of nonzero coefficients – hence greater sparsity – but which still produces a small approximation error. This is the role played by the function F_2 below which counts the number of nonzero coefficients z_i – essentially the l_0 norm of the vector z – which is a measure of the *lack of sparsity* of z. Bearing these motivations in mind, the collage-based inverse problem for images can be viewed as a multi-objective optimization problem which involves the following three criteria:

- $F_1(z) = z^T A z + b^T z + c$,
- $F_2(z) = \sum_{i=1}^{N} H(z_i)$, where $H(z_i) = 1$ if $z_i > 0$ and 0 otherwise,
- $F_3(z) = \sum_{i=1}^{N} \frac{z_i}{Z} \ln\left(\frac{z_i}{Z}\right)$ where $Z = \max\{z_i\}$.

The function F_1 is the squared collage distance and it has to be minimized. . As mentioned above, the function F_2 measures the lack of sparsity of z and therefore has to be minimized. Finally the function F_3 is the negative Shannon entropy, which will have to be minimized. (Here we mention that other definitions of entropy could, in principle, be used.)

We are now interested in the solution to the following multi-objective problem,

$$\min_{z\in\Omega}(F_1(z),F_2(z),F_3(z))\,, \tag{13}$$

where Ω is a compact subset of set $\mathbb{R}^{2N}$ which describes the set of all possible constraints. Because of presence of F_2 this optimization problem is nonsmooth and NP hard. We then proceed by replacing the function F_2 with a differentiable approximation. For this purpose, we propose the following approximation of $H_i(z)$,

$$H_\alpha(z_i) := 1-\exp(-\alpha z_i^2), \quad \alpha>0\,, \tag{14}$$

and the accuracy of this approximation increases as $\alpha\to+\infty$.

There are different techniques to deal with a multi-objective optimization problem and the notion of optimal solution has to be understood in the Pareto sense. In fact it is unlikely to be able to determine an optimal vector z_{min} which minimizes all criteria simultaneously. However in practical situations, the simplest and most common approach which is used in this context is the one based on a scalarization technique. The idea behind this approach consists of combining all different criteria in a unique objective function by introducing a vector of non-negative weights, $L=(l_1,l_2,l_3)$, $\sum_{i=1}^3 l_i=1$. The scalarization of the above multi-objective model leads to the following single-criterion optimization problem

$$\min_{z\in\Omega}\; l_1F_1(z)+l_2F_2(z)+l_3F_3(z)\,. \tag{15}$$

NUMERICAL SIMULATIONS

The following examples illustrate that adding small-weighted entropy and sparsity constraints can lead to a better fixed point approximation.

Example 1. For $j=1,\dots,N$, we introduce the family of IFS maps

$$\begin{cases} w_i^j(x) &= \frac{1}{2^j}x+(j-1)\frac{1}{2^j}, \\ \phi_i^j(t) &= \alpha_i^j t+\beta_i^j\,, \end{cases} \qquad i=1,\dots,2^j,$$

which for each j defines an associated IFSM map

$$(T_ju)(x)=\sum_{i=1}^{2^j}{}'\phi_i^j(u((w_i^j)^{-1}(x)))\,.$$

The map T_j assembles 2^j shrunken and adjusted copies of $u(x)$, each supported on an interval of width $\frac{1}{2^j}$, of the function u. For fixed j, the domains of the maps w_i^j only overlap at the endpoints of their domains. On the other hand, any point $x\in[0,1]$ that is not a multiple of $\frac{1}{2^m}$ for some m appears in the domain of exactly N of the maps in the family, once per member of the family, offering a sort of map redundancy. We define the combined (contractive) map

$$(Tu)(x)=\sum_{j=1}^{N}(T_ju)(x)\,,$$

and consider the associated squared collage distance $F_1(z)$, where z is the vector of parameters α_i^j and β_i^j. In this example, we explore the scalarized optimization problem (15).

We choose the target function $v(x)=0.8x^2+0.1$, $x\in[0,1]$. We set $N=4$, which means we have a total of 60 parameters in the optimization problem. We use the nonlinear program solver in Maplesoft's Maple to solve (15). The first row of Table 1 shows the results without any entropy or sparsity constraints; we use 38 nonzero parameters. In the Table, values are presented with numbers of decimal places that illustrate the effect of changing the weights l_1, l_2, and l_3, and $\|v-\bar u\|_2$ is the L^2 distance between the target $v(x)$ and the resulting fixed point approximation $\bar u=T\bar u$.

Table 1. *Results of Example 1.*

l_2	l_3 ($\times10^{-5}$)	$\sqrt{F_1(z)}$	$F_2(z)$	$F_3(z)$	$\|v-\bar u\|_2$
0	0	0.014300	38	-7.808589	0.0000741868
0	1.3	0.014409	60	-12.648761	0.0000739184
0	1.4	0.014420	60	-12.560957	0.0000731701
0	1.5	0.014435	60	-12.701199	0.0000730789
0.3	0	0.756211	6	-2.348598	0.0029801527
0.01	0	0.066448	8	-2.545824	0.0003091702
0.0001	0	0.016935	10	-2.984062	0.0000789527
0.0001	1.5	0.016358	23	-7.929161	0.0000754027

In the absence of a sparsity constraint, *i.e.*, when $l_2=0$, we see that adding an entropy constraint with relatively small weighting l_3 leads to parameter values corresponding to a larger collage distance but to a better fixed point approximation. The numerical

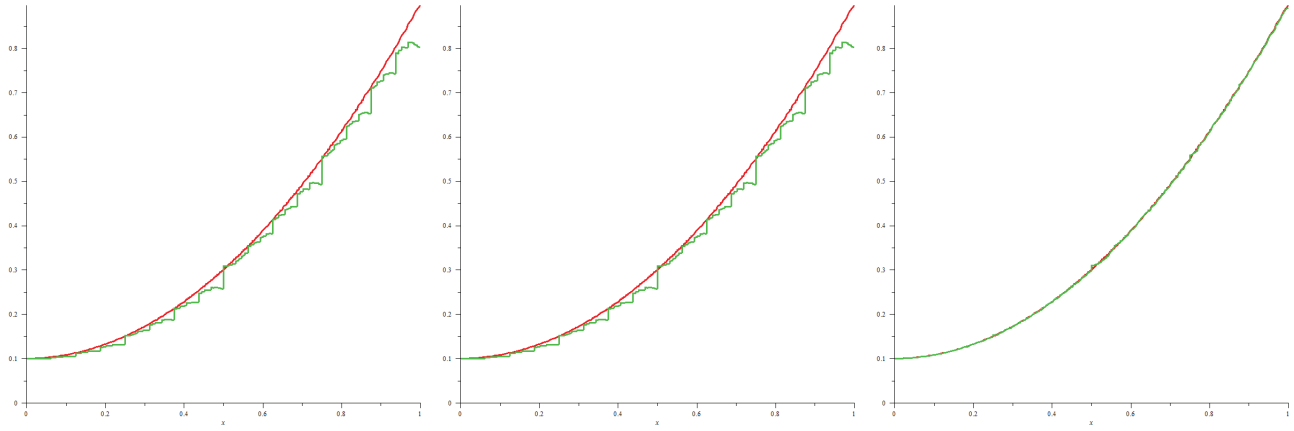

Fig. 1. *(left-to-right) Iterations 2, 4, and 8 of 23-map IFSM operator corresponding to the final row of Table 1.*

results are presented in rows two through four of the table; note that all 60 parameters are nonzero in these cases. Including only sparsity constraints, as in rows five to seven of the table, we see that the number of nonzero parameters is reduced dramatically from the collage distance case. Row five presents results for a case where only six parameters are nonzero, but the approximation error suffers. In row seven, we demonstrate that we can come close to the approximation error in row one while only using 10 nonzero parameters. Finally, in row eight, we include both entropy and sparsity constraints and come very close to the approximation error in row one by using less than two thirds of the number of parameters. Fig. 1 displays some iterates of the IFSM operator T corresponding to the final row of the table.

Example 2. We repeat the process of Example 1, this time using a nonmonotone target function $v(x) = \sin \pi x$ and setting $N = 6$ (corresponding to 124 parameters). Table 2 presents the results.

Table 2. *Results of Example 2.*

l_2	l_3 ($\times 10^{-7}$)	$\sqrt{F_1(z)}$
0	0	0.286458
0	5	0.286458
0	1	0.286458
0.0001	1	0.286500

l_2	$F_2(z)$	$F_3(z)$	$\|v-\bar{u}\|_2$
0	62	-19.707141	0.001142806379840
0	65	-23.653037	0.001142806381003
0	65	-23.651937	0.001142806379732
0.0001	35	-9.814576	0.001142959788729

In Fig. 2, we show some iterates of the IFSM operator T corresponding to the final row of the table.

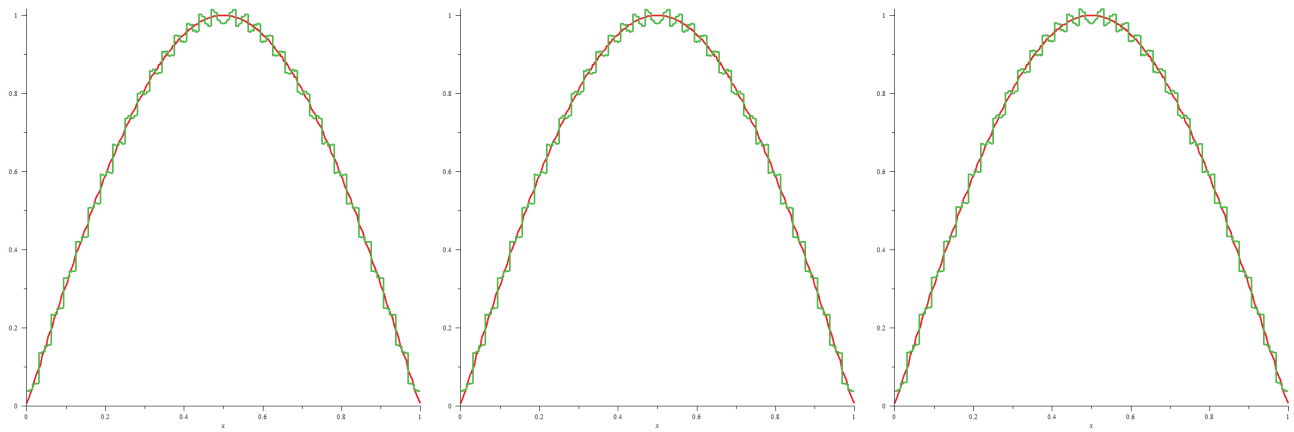

Fig. 2. *(left-to-right) Iterations 2, 4, and 8 of 23-map IFSM operator corresponding to the final row of Table 2.*

REFERENCES

Barnsley MF, Ervin V, Hardin D, Lancaster J (1985). Solution of an inverse problem for fractals and other sets. Proc Nat Acad Sci USA 83:1975–77.

Barnsley MF (1989). Fractals everywhere. New York: Academic Press.

Barnsley MF, Demko S (1985). Iterated function systems and the global construction of fractals. Proc Roy Soc London Ser A 399:243–75.

Barnsley MF, Hurd L (1993). Fractal image compression. Natick, Mass: AK Peters.

Centore P, Vrscay ER (1994). Continuity of attractors and invariant measures for Iterated Function Systems. Canad Math Bull 37(3):315–29.

Demers M, Kunze H, La Torre D (2012). On random iterated function systems with greyscale maps. Image Anal Stereol 31(2):109–20.

Elad M. (2010) Sparse and redundant representations: From theory to applications in signal and image processing. New York: Springer.

Fisher Y (1995). Fractal image compression, theory and application. New York: Springer.

Forte B, Vrscay ER (1995). Solving the inverse problem for function and image approximation using iterated function systems. Dyn Contin Discret Impuls Syst 1(2):177-232.

Forte B, Vrscay ER (1998). Theory of generalized fractal transforms. In: Fisher Y, ed. Fractal Image Encoding and Analysis. NATO ASI Series F 159:145–68. New York: Springer Verlag.

Ghazel M, Freeman GH and Vrscay ER (2003). Fractal image denoising. IEEE Trans Image Proc 12(12):1560–78.

Hutchinson J (1981). Fractals and self-similarity. Indiana Univ J Math 30:713–47.

Iacus S, La Torre D (2005). A comparative simulation study on the IFS distribution function estimator. Nonlinear Anal Real World Appl 6(5):858–73.

Iacus S, La Torre D (2005). Approximating distribution functions by iterated function systems. J Appl Math Dec Sci 1:33–46.

Jaynes ET (1957). Information theory and statistical mechanics. Phys Rev 106(4):620–30.

Kunze H, La Torre D, Vrscay ER (2008). From iterated function systems to iterated multifunction systems. Commun Appl Nonlinear Anal 15(4):1–15.

Kunze H, La Torre D, Vrscay ER (2009). A generalized collage method based upon the Lax-Milgram functional for solving boundary value inverse problems. Nonlinear Anal 71(12):e1337–43.

Kunze H, La Torre D, Vrscay ER (2012). Solving inverse problems for DEs using the collage theorem and entropy maximization. Appl Math Letters 25(12):2306–11.

Kunze H, La Torre D, Mendivil F, Vrscay ER (2012). Generalized fractal transforms and self-similar objects in cone metric spaces. Comput Math Appl 64:1761–9.

La Torre D, Vrscay ER, Ebrahimi M, Barnsley M (2009). Measure-valued images, associated fractal transforms and the affine self-similarity of images. SIAM J Imaging Sci 2(2):470–507.

La Torre D, Vrscay ER (2009). A generalized fractal transform for measure-valued images. Nonlinear Anal 71(12):e1598–607.

La Torre D, Vrscay ER (2011). Generalized fractal transforms and self-similarity: recent results and applications. Image Anal Stereol 30(2):63–76.

La Torre D, Vrscay ER (2012). Fractal-based measure approximation with entropy maximization and sparsity constraints. AIP Conf Proc 1443:63–71.

Lu N (2003). Fractal imaging. New York: Academic Press.

Vrscay ER, Saupe D (1999). Can one break the 'collage barrier' in fractal image coding? In: Dekking M, LevyVehel J, Lutton E, Tricot C eds. Fractals: Theory and Applications in Engineering, London: Springer-Verlag. 307–23.

FORTHCOMING MEETINGS

2014

23rd Australian Conference on Microscopy and Microanalysis & 2014 International Conference on Nanoscience and Nanotechnology
Adelaide, Australia
February 2–6
http://www.aomevents.com/ACMMICONN

SSIAI 2014 - IEEE Southwest Symposium on Image Analysis and Interpretation
San Diego, California, USA
April 6–8
http://www.ssiai.org/

Lehigh Microscopy School 2014
Bethlehem, PA, USA
June 8–13
http://www.lehigh.edu/microscopy

Inter/Micro 2014, 65th Annual Applied Microscopy Conference
Chicago, IL, USA
July 14–18
http://www.mcri.org/home/section/101/inter-micro

Microscopy & Microanalysis 2014 - Annual Meeting of the Microscopy Society of America and the Microbeam Analysis Society
Hartford, CT, USA
August 3–7
http://www.microscopy.org/MandM/2014/index.cfm

IMC 2014, 18th International Microscopy Congress
Prague, Czech Republic
September 7–12
http://www.imc2014.com/

ICIP 2014, IEEE International Conference on Image Processing
Paris, France
October 27–30
http://www.icip2014.com/

The host: CSMS Supported by: IFSM

MAIN DEADLINES

1 September 2013 On-line abstract submission open
On-line registration available at the website

15 February 2014 Abstract submission deadline
Early registration deadline

1 July 2014 Standard registration deadline

SCIENTIFIC TOPICS

Instrumentation and Techniques

Electron optics and optical elements
High resolution TEM and STEM
Super-resolution light microscopy and nanoscopy imaging
Scanning electron microscopy
Analytical electron microscopy
Environmental electron microscopy
In-situ microscopic techniques and cryo-microscopies
Ultrafast and high-throughput microscopies
Electron and X-ray diffraction techniques
Electron tomography
Electron holography and lens-less imaging
Surface microscopy, spectromicroscopy and microspectroscopy
Focused ion beam microscopy and techniques
Scanning probe microscopy and near-field microscopies
X-ray, atom probe, neutron and other microscopies
Electron microscopy theory and simulations

Material Sciences

Nanoobjects and engineered nanostructures, catalytic materials
Carbon-based nanomaterials, nanotubes, fullerenes, graphenes
Thin films, coatings and surfaces
Metals, alloys and metal matrix composites
Ceramics and inorganic materials
Polymers and organic materials
Composite materials and hybrids
Semiconductors and materials for information technologies
Defects in materials and phase transformations
Porous and architectured materials
Amorphous and disordered materials, liquid crystals, quasicrystals
Magnetic, superconducting, ferroelectric and multiferroic materials
Materials in geology, mineralogy and archeology
Energy-related materials

Life Sciences

Live imaging of cells, tissues and organs
Structure and function of cells and organelles
High-resolution localization of molecular targets
and macromolecular complexes
Structure of macromolecules and macromolecular complexes
Cellular transport and dynamics
Microbiology and virology
Invertebrates and parasitology
Plant science and mycology
Gene-modified organisms and animal science
Human health and disease
Physiology and pathology
Advances in immunohistochemistry and cytochemistry
Embryology and development biology
Neuroscience

Interdisciplinary

Correlative microscopy in life and material sciences
Imaging mass spectrometry
Microscopy of single molecule dynamics
High-throughput microscopy and its applications in life and material sciences
Nanoparticles: Biomedical applications and bio-safety issues
Microscopy in forensic science
Microscopy in arts, restoration and archeology
Three-dimensional reconstructions in microscopy
Microscopic image analysis and stereology
Advances in sample preparation techniques
Multidisciplinary applications of progressive light microscopy imaging techniques
In-situ and environmental microscopy of processes in materials
and material reactions
Materials for medicine and biomaterials

CONGRESS SECRETARIAT

IMC 2014 Congress Secretariat, GUARANT International, Opletalova 22, 110 00 Praha 1, Czech Republic
Tel: +420 284 001 444 Fax: +420 284 001 448 E-mail: info@imc2014.com

Get more information and subscribe for updates at www.imc2014.com

FROM ISS

TAKING A NEW DIMENSION

Dear Stereologist,

2013 is already coming to an end and our Society is looking forward to take up new challenges.

Our recent European congress held in Kaiserslautern was a nice opportunity to meet a good number of you and discover recent advances in stereology and image analysis.

Thanks to the energy deployed by Katja, Claudia and the whole Fraunhofer team we also had stimulating discussions.

Let me once again thank them wholeheartedly for this success.

It is now time for our Society to take a new dimension and increase its visibility.

Be it through discussion groups, through cosponsored sessions in larger congresses or through short courses on "digital image analysis and stereology", every member is invited to promote ISS in in his community.

With fifty years of contributions to the advancement of science, our society has a lot to offer.

Please share with your friends and colleagues the following resources:

- LinkedIn discussion group on Stereology and Image analysis
- Portal towards digitized issues of Acta Stereologica (http://popups.ulg.ac.be)
- Open access to Image Analysis and Stereology (http://www.ias-iss.org/)
- Our website with announcements of future congresses and short courses

And don't miss our next rendez-vous :

"Microscopic image analysis and stereology" (Session ID-9)
at the 18th Int Microscopy Congress
Prague, 7–12 Sep 2014.

Last but not least, the next International Congress for Stereology will be announced very soon... please book July 6-10, 2015 in your agenda.

I wish you all plenty of energy and enthusiasm for 2014 ... and if you have some left, please feel free to share it with ISS.

We need you!
Eric Pirard

ANNOUNCEMENT

ISS MEMBERSHIP APPLICATION/RENEWAL FOR 2014

The International Society for Stereology is a non-profit organization, whose purpose is to promote the exchange and dissemination of information about stereology among persons of various scientific disciplines and countries. The members' fees constitute the sole source of revenues of the ISS. In order to help us promote stereology, we would be pleased to welcome you as a member.

The ISS membership fee (regular members 50 €, students 25 €) includes a subscription to the journal 'Image Analysis and Stereology'

(http://www.ias-iss.org)

To renew your membership for 2014, please pay by bank transfer to the following account

IBAN: BE69 7320 1659 9478 BICCode: CREGBEBB

account owner International Society for Stereology

To pay via PayPal or to apply for a NEW membership, please send a message to

gemme@ulg.ac.be

You can also contact the ISS President and secretary/treasurer at:

gemme@ulg.ac.be

Eric Pirard
ISS President

Claudia Redenbach
ISS Secretary/treasurer

INSTRUCTIONS TO AUTHORS

Manuscript Submission. Manuscripts should be submitted electronically in PDF or Word format (first submission) and in Word or LaTex format (final submission) at Online Submission

www.ias-iss.org.

What To Submit:

- PDF or Word file of the Manuscript prepared by the author (obligatory at first submission)
- Cover Letter (obligatory)
- Supplementary Material (optional)
- Manuscript and Figures (obligatory at final submission of the accepted manuscript)
- Copyright Transfer Agreement (obligatory at final submission of the accepted manuscript)

E-mail correspondence. Should you require any information regarding article submission, please feel free to contact the Editorial Office at

ias@mf.uni-lj.si or editor.ias@mf.uni-lj.si

Guidelines for Manuscript Preparation. For rapid and accurate publication it is essential that manuscripts follow exactly the guidelines described below. Manuscript should be written in MS Word or LaTeX.

LaTeX. LaTeX style guide PDF file presents the instructions for preparing manuscripts for the Image Analysis & Stereology journal in LaTeX, and serves itself as an example of a LaTeX file conforming to the described form.

Language is English. Please be consistent. Use the same form of English (UK or American) throughout the text.

Length. Full-length research papers or full-length review articles including tables and figures with legends and references should not exceed 30 pages (30 lines per page, font size 11 pt, single column) or 15 typeset pages if prepared in LaTeX. Short research communications, reviews, communications or notes should not exceed 15 pages (7 typeset pages if prepared in LaTex) including tables and figures with legends.

Title. Short and to the point, not longer than 120 characters (including spaces); it should be written entirely in capital letters. Title should indicate the methodological aspects of the paper, which are of interest also for several fields of application. Include the running title with the surname of the first author with no more than 100 characters including spaces (*e.g.*, MACKAY CE *ET AL*: Comparison of MRI and physical sections).

Authors. Whole name(s) and family name of each author; no academic degrees or titles. Indicate who will be responsible for correspondence. Complete address of each author including an e-mail address.

Abstract. Not more than 250 words, summarizing the work presented in the manuscript, in 3rd person. Abstract should be underrstandable to a nonspecialist. It should be followed by a list of keywords (not more than 6) in alphabetical order.

Keywords should allow an appropriate classification of the paper in regard to the methodology and field of application.

Text. Sufficient details must be given to enable an interdisciplinary audience of the journal to understand the considered problem and methods. This includes a brief explanation of basic concepts, abbreviations and symbols, and, if available, a review paper as a reference. The manuscript should be structured with the following headings: Introduction, Materials and Methods, Results, Discussion,

Acknowledgements, and References. The headings should be placed on separate lines and written in capitals with no underlining. Avoid unnecessary subheadings. In the text do not underline words, do not use letters in bold type.

Methods which are of some general character should be emphasized. New methods or theoretical results should be given with an appropriate reasoning or derivation. Applications of methods are welcome. Appropriate real data, simulation or numerical results should be given to illustrate the main results.

Figures and Tables should be in a form and condition suitable for publication across a single column (8 cm) or a whole page (16 cm). The minimum font size of characters is 11. Figures and tables should be numbered consecutively in Arabic numerals (*e.g.*, Fig. 1; Table 1) and headed with a short title. Please mark in the manuscript (i.e., insert Fig. 1 or Table 1) where Tables or Figures should be placed in the text. Each figure and table should be accompanied by a self-explanatory legend. Please note that Figures and Tables should be included in manuscript file at first submission. At final submission (after the acceptance of the paper), all figures and tables should be uploaded as separate files, using the Supplementary files form. Ideally, all original files (manuscript, figures and tables) should be collected in a ZIP archive and uploaded as a Supplementary file. Maximum file size for upload is 50 MB.

Figures should be sent as TIFF or JPG files for raster images (bitmaps) or PS format for vector images. Files should have 600 dpi resolution for colour, greyscale images or black and white images.

Color Prints. A limited number of colour images is free of charge.

Equations should be on separate lines, with an extra spacing above and below. They should always be numbered, placing the number in brackets against the right hand margin. If a mathematical expression is to be included as a part of a sentence try to maintain the single line spacing by use of brackets (*e.g.*, (1-x)/(3-h)). Please, use an abbreviation (*e.g.*, Eq. 1) when discussing an equation in a sentence.

Units. SI units should be used wherever these exist for the parameter concerned. Units should be separated from values (*e.g.*, 5 μm, 2 mg, 1 min); exceptions are °, °C and % (*e.g.*, 90°, 37°C, 50%).

References in the text should be given in parentheses: *e.g.*, (Fish, 1971) when there is only one author; (Fish, 1971a,b) when an author has two references in the same year; (Fish, 1971; 1972) when an author has two references in different years; (Flesh and Fowl, 1954) when there are two authors; (Good *et al*., 1962) when there are more than two authors; (Flesh and Fowl, 1954; Good *et al*., 1962) when there is more than one reference; "as shown by Miller (1967), the ..." when author's name is part of a sentence. If the same authors have more than one publication in one year, then distinguish them, thus: 1985a, 1985b, etc. The reference list should be in alphabetical order and prepared according to the examples below:

Macpherson IA (1973). Soft agar technique. In: Kruse PF, Patterson IMK, eds. Tissue culture methods and application. Ch. 7. New York: Academic Press, 276-81.

Osler AG (1976). Complement: Mechanisms and functions. Englewood Cliffs: Prentice Hall, 51-5.

Solter NA, Wasserman SI, Austen KF (1976). Cold urticaria: release into circulation of histamine and eosinophilic chemotactic factor of anaphylaxis during cold challenge. N Engl J Med 294: 687-90.

Bengtsson S, Solheim BG (1992). Enforcement of data protection, privacy and security in medical information. In: Lun KC, Degoulet P, Piemme TE, Rienhoff O, eds. MEDINFO 92. Proceedings of the 7th World Congress on Medical Informatics, 1992 Sep 6-10; Geneva, Switzerland. Amsterdam: North-Holland, 1561-5.

"Personal communications", "unpublished observations" and "in preparation" should be given in the text and should not appear in the reference list.

Page Numbering. Pages in the manuscript should be numbered in Arabic numerals starting with the cover page.

Supplementary Materials are images, movies, data sets, and other files that support and augment the content of a manuscript. They are intended for publication only in the Online version of Image Analysis & Stereology. These materials should be referenced in the manuscript, and then accessed via the online Journal.

Supplementary Materials generally fall into the following categories

1. Extra Tables
2. Extra Figures
3. Datasets and Movies

Guidelines for submitting Supplementary Materials: Supplementary Materials must be submitted with the manuscript at the time of submission at Step 4 of the submission process. Supplementary Materials must be accompanied by a complete set of legends, one legend for each supplemental item. They must be referenced in the manuscript body at least once.

Cover letter This letter must be submitted in a text-box in the first step of the submission process. The letter must contain the following:

1. A brief statement of the significance of the paper.
2. Information about conflict of interest: Any conflict or no conflict of interest, should be declared and described clearly and explicitly.
3. A statement that all of the authors have directly participated in the planning, execution, or analysis of the study and resulting paper, and have read and approved the version submitted. **Please define the contribution of each author separately – without this statement the paper will not be processed for peer review!**
4. The authors confirm that the submitted manuscript has been either written or reviewed for quality of language by a native English speaker or alternatively professionally edited. Please note that manuscripts written in poor English will be rejected without possibility for further consideration.
5. (Optional) The contact information of any suggested reviewers (names, addresses, and e-mail).

Manuscripts submitted without a cover letter will not be processed for peer review.

Copyright Transfer Agreement After the manuscript has been accepted for publication in Image Analysis & Stereology the Copyright Transfer Agreement will be sent to the corresponding author. All authors engaged in the manuscript need to sign the form.

Submission Preparation Checklist As part of the submission process, authors are required to check off their submission's compliance with all of the following items, and submissions may be returned to authors that do not adhere to these guidelines.

1. The submission has not been previously published, nor is it before another journal for consideration (or an explanation has been provided in the Cover Letter).
2. The initial submission file is in PDF. The original manuscript files in Microsoft Word or LaTeX will be uploaded at final submission of the accepted manuscript.
3. The text adheres to the stylistic and bibliographic requirements outlined in the Author Guidelines, which is found in About the Journal.
4. References are in the correct format for this journal. All references listed in the reference list are cited in the text, and vice versa. Where available, DOI or URL for the references have been provided.
5. If the submission uses copyrighted material from other sources (including the Web), permission has been obtained for its use; the sources are appropriately noted in the text.
6. Submission is accompanied with a cover letter, written in accordance to the Author Guidelines, found in About the Journal.